

Doctor thesis

Quasielastic  $\pi^-$ -nucleus scattering at 950 MeV/ $c$

Department of Physics,  
Tohoku University

Yuu Fujii

February, 1998



# Contents

<b>1</b>	<b>Introduction</b>	<b>6</b>
1.1	The quasielastic scattering . . . . .	6
1.2	Previous studies on quasielastic scattering . . . . .	7
1.3	Present experiment . . . . .	8
<b>2</b>	<b>Experimental Setup</b>	<b>11</b>
2.1	Overview . . . . .	11
2.2	K6 beam line . . . . .	11
2.3	Beam spectrometer . . . . .	13
2.4	Scattered-particle spectrometer (SKS) . . . . .	16
2.5	Trigger and data-acquisition system . . . . .	17
2.6	Detector arrangement for the present experiment . . . . .	18
2.7	Run summary . . . . .	19
<b>3</b>	<b>Data Analysis</b>	<b>23</b>
3.1	Outline . . . . .	23
3.2	Momentum of beam particle . . . . .	23
3.3	Momentum of scattered particle . . . . .	26
3.4	Event vertex . . . . .	27
3.5	Doubly differential cross sections . . . . .	29
3.5.1	Effective solid angle . . . . .	30
3.5.2	Efficiencies . . . . .	30
3.5.3	Combination of the different setup spectra . . . . .	32
3.5.4	Extraction of D and $^6\text{Li}$ spectra . . . . .	36
<b>4</b>	<b>Results and Discussion</b>	<b>38</b>
4.1	Overview . . . . .	38
4.2	Doubly differential cross sections . . . . .	38
4.3	Fit to the quasielastic peak . . . . .	41
4.3.1	Fitting procedure . . . . .	41
4.3.2	Model uncertainty of the fitting . . . . .	42
4.4	Quasielastic cross sections . . . . .	43
4.5	Effective number of nucleons . . . . .	45
4.6	Fermi momenta . . . . .	46

4.7	Peak shifts . . . . .	49
4.8	Comparison with other data . . . . .	52
4.9	Comparison with theoretical calculation . . . . .	56
<b>5</b>	<b>Summary and Conclusions</b>	<b>59</b>
<b>A</b>	<b>Acceptance Study of the SKS</b>	<b>61</b>
A.1	Effective solid angle of the SKS . . . . .	61
A.1.1	Monte-Carlo simulation code . . . . .	62
A.2	$\pi^-$ -p cross sections . . . . .	69
<b>B</b>	<b>Data and Fitted Results</b>	<b>74</b>

# List of Tables

1.1	Couplings of reactions to $S, T$ . . . . .	7
2.1	Design specifications of the K6 beam-spectrometer system. . . . .	12
2.2	Specifications of the drift chambers. . . . .	14
2.3	Specifications of the trigger counters. . . . .	14
2.4	Design parameters of the SKS. . . . .	16
2.5	Parameters of the SKS magnet. . . . .	16
2.6	All the targets used in the present experiment. . . . .	20
2.7	Total number of irradiated $\pi^-$ for each target and SKS setup. . . .	20
2.8	Total number of $\pi^-$ for the acceptance study. . . . .	21
3.1	Efficiencies for the carbon runs with the 395A mode. . . . .	32
4.1	Comparison of $\alpha$ with other probes. . . . .	45
4.2	Measured and calculated values of $A_{\text{eff}}$ . . . . .	48
4.3	Dominant couplings of reactions and observed peak shifts . . . . .	49
A.1	Cuts for each detector applied in the Monte-Carlo simulation. . . .	64

# List of Figures

1.1	The spin/isospin content of the pion-nucleon scattering at $q = 400$ MeV/ $c$ for beam momenta of 624 and 950 MeV/ $c$ . . . . .	10
1.2	The $q$ dependence of the spin/isospin content of the pion-nucleon scattering at a beam momentum of 950 MeV/ $c$ . . . . .	10
2.1	Schematic view of the K6 beam line of KEK 12-GeV PS . . . . .	12
2.2	Schematic view of the beam spectrometer. . . . .	13
2.3	Schematic top view of the SKS. . . . .	15
2.4	Trigger logic diagram. . . . .	18
2.5	Diagram of the data-acquisition system. . . . .	19
2.6	Coverage of the present setup. . . . .	22
3.1	Flow chart of offline analysis program in this work. . . . .	24
3.2	Typical distribution of $\chi^2$ for the beam trajectory reconstruction. . . . .	25
3.3	Typical distribution of beam momentum. . . . .	26
3.4	Typical distribution of $\chi^2_{\text{SKS}}$ . . . . .	27
3.5	The event vertex. . . . .	28
3.6	Effective solid angle of the SKS for the 395A mode. . . . .	31
3.7	Differential cross sections for $\pi^-$ -p elastic scattering. . . . .	33
3.8	$^{12}\text{C}(\pi^-, \pi^-')$ , $q = 550$ MeV/ $c$ quasielastic spectra for each SKS mode. . . . .	34
3.9	Ratios of the doubly differential cross sections in the overlapped region. . . . .	35
3.10	Doubly differential cross sections for the $\text{CD}_2$ and $^6\text{LiD}$ targets at $q = 400$ MeV/ $c$ . . . . .	37
4.1	Doubly differential cross sections for D, $^6\text{Li}$ , C, Ca, Zr, and $^{208}\text{Pb}$ at $q = 500$ MeV/ $c$ . . . . .	39
4.2	Doubly differential cross sections for C at $q = 350, 450, 550$ , and 650 MeV/ $c$ . . . . .	40
4.3	Samples of the fitting. . . . .	42
4.4	Quasielastic cross sections for D, $^6\text{Li}$ , C, Ca, Zr, and $^{208}\text{Pb}$ as a function of momentum transfer. . . . .	44
4.5	Fit of the effective number of nucleons to a power law. . . . .	46

4.6	Extracted widths of quasielastic peak as a function of momentum transfer. . . . .	47
4.7	Fermi momenta extracted from measured widths of the quasielastic peaks. . . . .	48
4.8	Quasielastic peak shifts relative to scattering from hydrogen for D, ${}^6\text{Li}$ , C, Ca, Zr, and ${}^{208}\text{Pb}$ . . . . .	50
4.9	A comparison of the quasielastic peak shifts for different probes. . .	51
4.10	Response functions for ${}^{12}\text{C}$ at a momentum transfer of approximately 475 MeV/ $c$ for (a) the $(\pi^-, \pi^{-'})$ reaction at 950 MeV/ $c$ present work and (b) $(K, K')$ reaction at 705 MeV/ $c$ . . . . .	54
4.11	Ratio of response functions $R_\pi/R_K$ . . . . .	54
4.12	Response functions for ${}^{12}\text{C}$ at a momentum transfer of approximately 400 MeV/ $c$ for $(\pi^-, \pi^{-'})$ reaction at (a) 950 MeV/ $c$ present work and (b) 624 MeV/ $c$ previous work. . . . .	55
4.13	Ratio of response functions (a)/(b). . . . .	55
4.14	A comparison between a free and RPA response in the scalar-isoscalar channel for $\pi^-$ - ${}^{12}\text{C}$ quasielastic scattering. . . . .	57
4.15	$\pi^-$ - ${}^{12}\text{C}$ quasielastic cross sections compared with the RPA calculation. . .	58
A.1	Schematic top view of the SKS showing an additional acceptance cut. . .	63
A.2	Effective solid angle of SKS for the 395A mode. . . . .	65
A.3	Effective solid angle of SKS for the 320A mode. . . . .	66
A.4	Effective solid angle of SKS for the 272A mode. . . . .	67
A.5	Effective solid angle of SKS for the 210A mode. . . . .	68
A.6	Differential cross sections for $\pi^-$ -p elastic scattering measured with the 395A mode. . . . .	70
A.7	Differential cross sections for $\pi^-$ -p elastic scattering measured with the 320A mode. . . . .	71
A.8	Differential cross sections for $\pi^-$ -p elastic scattering measured with the 272A mode. . . . .	72
A.9	Differential cross sections for $\pi^-$ -p elastic scattering measured with the 210A mode. . . . .	73
B.1	Doubly differential cross sections for the $\pi^-$ -D scattering. . . . .	75
B.2	Doubly differential cross sections for the $\pi^-$ - ${}^6\text{Li}$ scattering. . . . .	77
B.3	Doubly differential cross sections for the $\pi^-$ -C scattering. . . . .	79
B.4	Doubly differential cross sections for the $\pi^-$ -Ca scattering. . . . .	81
B.5	Doubly differential cross sections for the $\pi^-$ -Zr scattering. . . . .	83
B.6	Doubly differential cross sections for the $\pi^-$ - ${}^{208}\text{Pb}$ scattering. . . . .	85

# Chapter 1

## Introduction

### 1.1 The quasielastic scattering

Quasielastic scattering is a process that an incident particle elastically interacts with only one nucleon inside a nucleus, with all the other nucleons being spectators. The inclusive doubly differential cross section of the quasielastic scattering, as a function of energy loss (the difference between initial and final laboratory kinetic energies of an incident particle), has two characteristic features: one is that the position of the peak corresponds to that of elastic scattering by a free nucleon, the other is that the width of the peak reflects internal motion of individual nucleons in a target nucleus.

On the basis of a plane wave impulse approximation (PWIA), the doubly differential cross section of quasielastic scattering can be factorized into three components,

$$\frac{d^2\sigma}{d\omega d\Omega} = A_{\text{eff}} \sum_{(S,T)} \left[ \left( \frac{d\sigma}{d\Omega} \right)_{\text{elem}} \right]_{(S,T)} R_{(S,T)}(q, \omega), \quad (1.1)$$

where  $A_{\text{eff}}$  is a normalization factor; it can be interpreted as an effective number of nucleons involved in the reaction,  $(d\sigma/d\Omega)_{\text{elem}}$  is the elementary projectile-nucleon elastic scattering cross section, and  $R(q, \omega)$  is a nuclear response; it gives a nuclear excitation probability for a given momentum transfer  $q$ . The suffix  $(S, T)$  denotes a channel with a given spin  $S$  and isospin  $T$ . Because a nucleon has spin and isospin of 1/2, there are six couplings of external fields to a free nucleon, isoscalar/isovector ( $T=0/T=1$ ), and spin 0/spin 1, with spin 1 having components of transverse and longitudinal with respect to the momentum transfer vector.

The nuclear response to an external probe, which couples to a nucleus through an excitation operator  $O_{(S,T)}$ , is defined as

$$R_{(S,T)}(q, \omega) = \sum_{n \neq 0} |\langle \psi_n | O_{(S,T)}(\vec{q}) | \psi_0 \rangle|^2 \delta(\omega - (E_n - E_0)), \quad (1.2)$$

where  $|\psi_n\rangle$  is a nuclear eigenstate of energy  $E_n$ .



Table 1.1: Couplings of reactions to  $S, T$ 

	$S$	$T$
$(e, e')$ coulomb	0	0+1
$(e, e')$ magnetic	$\boldsymbol{\sigma} \times \mathbf{q}$	$\approx 1$
$(\mathbf{p}, \mathbf{p}')$	$\boldsymbol{\sigma} \cdot \mathbf{q}, \boldsymbol{\sigma} \times \mathbf{q}$	0+1
$(\mathbf{p}, \mathbf{n})$	$\boldsymbol{\sigma} \cdot \mathbf{q}, \boldsymbol{\sigma} \times \mathbf{q}$	1
$(\pi, \pi^0)$	$\approx 0$	1
$(\pi, \pi')$	$\approx 0$	$\approx 0$
$(K, K')$	$\approx 0$	$\approx 0$

The effects of nuclear correlations for the corresponding probes can be observed as changes in cross section, and spectral shape changes due to attractive or repulsive interactions. Thus we can study the nuclear correlations for each spin/isospin channel using the quasielastic scattering.

## 1.2 Previous studies on quasielastic scattering

The quasielastic scattering has been studied by using various reactions:  $(e, e')$  [1][2][3][4],  $(p, p')$  [5][6][7],  $(p, n)$  [8][9][10],  $(^3\text{He}, t)$  [11],  $(\pi, \pi')$  [12],  $(\pi^\pm, \pi^0)$  [13][14], and  $(K, K')$  [15], because no single probe can provide complete information on nuclear responses. Each probe provides complementary information on nuclear responses to one another. Couplings of reactions to  $S, T$  are listed in Table 1.1.

The  $(e, e')$  reaction has been studied for a long time because of its advantage of the well-understood nature and the weakness of the fundamental lepton-nucleon interaction. The experimental Coulomb (longitudinal) response has been found significantly lower than theoretical prediction. This “Quenching” has motivated a large experimental and theoretical effort.

In addition, various reactions with hadronic probes have been studied to explore the responses not accessible in the  $(e, e')$  reaction. The  $(\mathbf{p}, \mathbf{p}')$  and  $(\mathbf{p}, \mathbf{n})$  reactions have been used to study isovector spin-longitudinal and spin-transverse response separately. These studies have been motivated by a theoretical prediction of Alberico *et al.* [16]. They predicted that the spin-longitudinal response ( $R_L$ ) is shifted toward lower energy loss and enhanced due to attractive character of the associated particle-hole interactions, while the spin-transverse one ( $R_T$ ) is shifted toward higher energy loss and quenched due to the repulsive character of the interactions. The measured ratio of the responses  $R_L/R_T$ , however, shows no evidence for nuclear collectivity [7][17]. A number of studies have been attempted to explain this problem.

Recently, mesonic probes have been used to investigate the scalar-isoscalar and scalar-isovector responses:  $(\pi, \pi')$  and  $(K, K')$  reactions measure mostly the

scalar-isoscalar ( $S=T=0$ ) response, and  $(\pi^\pm, \pi^0)$  reaction measures only the isovector ( $T=1$ ), mostly scalar ( $S=0$ ) response. The  $(\pi, \pi')$  [12] and  $(\pi^\pm, \pi^0)$  [13][14] reactions were measured using pions of 624 MeV/ $c$  at the Clinton P. Anderson Meson Facility (LAMPF). The quasielastic peak positions for the  $(\pi^\pm, \pi^0)$  reaction showed hardening and increasing softening above about  $q = 400$  MeV/ $c$ , while no shifts were observed for the  $(\pi, \pi')$  reaction. This difference was tentatively explained as the difference in effective particle-hole interactions for different channels. These studies demonstrated that the pion quasielastic scattering can be used to study nuclear responses in the scalar-isoscalar and scalar-isovector channels. The  $(K^+, K^+')$  reaction at 705 MeV/ $c$  [15] was measured at the Brookhaven National Laboratory (BNL). Theoretical calculation for the quasielastic  $K^+$ -nucleus scattering was performed in a finite-nucleus continuum RPA framework [18]; the calculation well described the experimental results and provided a constraint on the strength of the effective particle-hole interaction in the scalar-isoscalar channel.

### 1.3 Present experiment

The present experiment is a study of quasielastic  $\pi^-$ -nucleus scattering at 950 MeV/ $c$ . The aim of the work is to study the nuclear response through a scalar-isoscalar ( $S=0, T=0$ ) dominant probe. An advantage of the present experiment compared to the previous one at 624 MeV/ $c$  is a predominance of the scalar-isoscalar channel. Figure 1.1 shows the spin/isospin content of the pion-nucleon scattering at  $q = 400$  MeV/ $c$  for beam momenta of 624 and 950 MeV/ $c$ . The higher beam momentum of 950 MeV/ $c$  makes pions a better probe of the nuclear response in the scalar-isoscalar channel. Further, the previous data at 624 MeV/ $c$  may be affected by a large distortion at high  $q$ , because the outgoing pion energy is in the delta resonance region. A higher beam energy is preferable to be relatively free from final state interaction.

In this work, the doubly differential cross sections were measured for a wide range of  $q$ , from 350 to 650 MeV/ $c$ . In Figure 1.2, the  $q$  dependence of the spin/isospin content of the pion-nucleon scattering for a 950 MeV/ $c$  pion beam is shown. The scalar-isoscalar coupling dominates the scattering up to  $q$  of about 550 MeV/ $c$  and the other couplings become dominant at higher  $q$ . Thus, we can study the  $q$  dependence of the scalar-isoscalar response for a wide range of  $q$ . In addition, we expect to see a contribution from non-scalar-isoscalar channels at high  $q$ .

We used seven targets over a wide range of target masses to study mass-number dependence of the quasielastic scattering.

The doubly differential cross sections are discussed as follows. First, we extract quasielastic portions of the cross sections and interpret them based on a non-interacting Fermi gas model and an eikonal approximation. Secondly, we compare the results with the previous pion and kaon data in terms of experimental response function. Finally, we compare the results with a finite-nucleus continuum RPA

calculation.

The present thesis comprises five chapters and two appendices. The experimental apparatus is described in Chapter 2. The data analysis is described in Chapter 3. In Chapter 4, the experimental results are presented and their interpretations are discussed. A summary and conclusions are given in Chapter 5. The acceptance study of the SKS is described in Appendix A and full quasielastic spectra are shown in Appendix B.

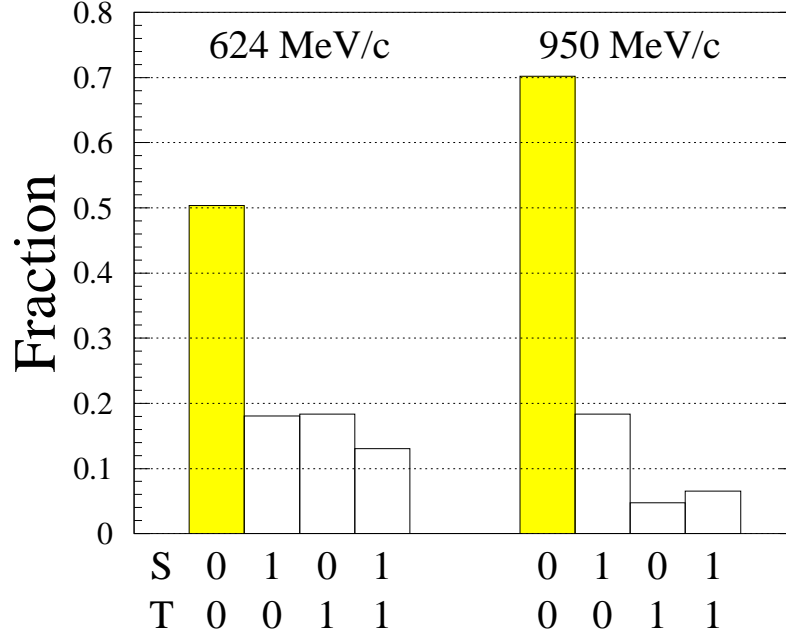


Figure 1.1: The spin/isospin content of the pion-nucleon scattering at  $q = 400$  MeV/ $c$  for beam momenta of 624 and 950 MeV/ $c$ .

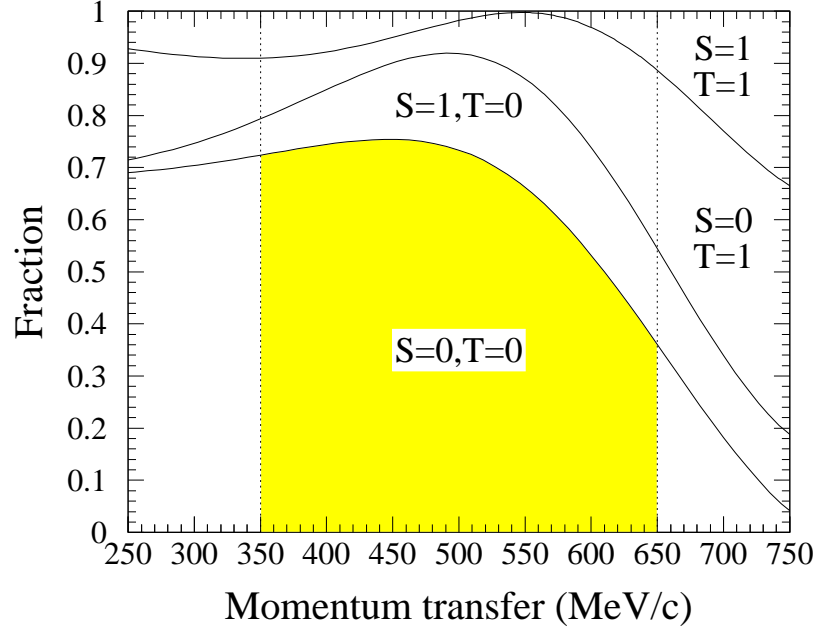


Figure 1.2: The  $q$  dependence of the spin/isospin content of the pion-nucleon scattering at a beam momentum of 950 MeV/ $c$ .

# Chapter 2

## Experimental Setup

### 2.1 Overview

The experiment was performed in the north experimental hall of the High Energy Accelerator Research Organization (KEK) 12-GeV proton synchrotron (PS) using the K6 beam line and the Superconducting Kaon Spectrometer (SKS)[19]. Since this experiment requires a 950 MeV/ $c$   $\pi^-$  beam and prefers a large solid angle spectrometer to cover entire quasielastic peak for the entire range of desired momentum transfer, the KEK-PS K6 beam line with the SKS spectrometer is a most suitable instrument for this experiment.

Intensive studies of pion-induced nuclear reactions have been carried out at meson factories, LAMPF, TRIUMF (Tri-Universities Meson Factory) and PSI (Paul Scherrer Institute). However, the maximum beam energy is limited to 500 MeV due to their proton beam energy. Meson beams in a momentum region of 1 GeV/ $c$  are available only at the KEK-PS and BNL-AGS.

The SKS was constructed at the K6 beam line of the KEK-PS to serve for nuclear physics experiments with meson beams in the 1 GeV/ $c$  region. The SKS was designed to achieve both a large solid angle (100 msr) and good momentum resolution (0.1% FWHM at 720 MeV/ $c$ ), particular emphasis being laid on study of  $\Lambda$ -hypernuclei via ( $\pi^+$ ,  $K^+$ ) reactions. Its large acceptance enables us to take quasielastic data over a wide range of momentum transfer.

### 2.2 K6 beam line

The K6 beam line was designed to provide pions and kaons in a momentum range between 0.5 and 2 GeV/ $c$  [19]. Secondary pions are produced on a production target hit by primary protons. In the present experiment, a platinum rod of diameter 6 mm and length 60 mm was used as the production target. The primary beam was extracted for 1.8 s in each 4.0 s, synchronized to the KEK 12-GeV PS operation cycle. Intensity of primary protons at the production target was typically  $2.2 \times 10^{12}$ /spill.

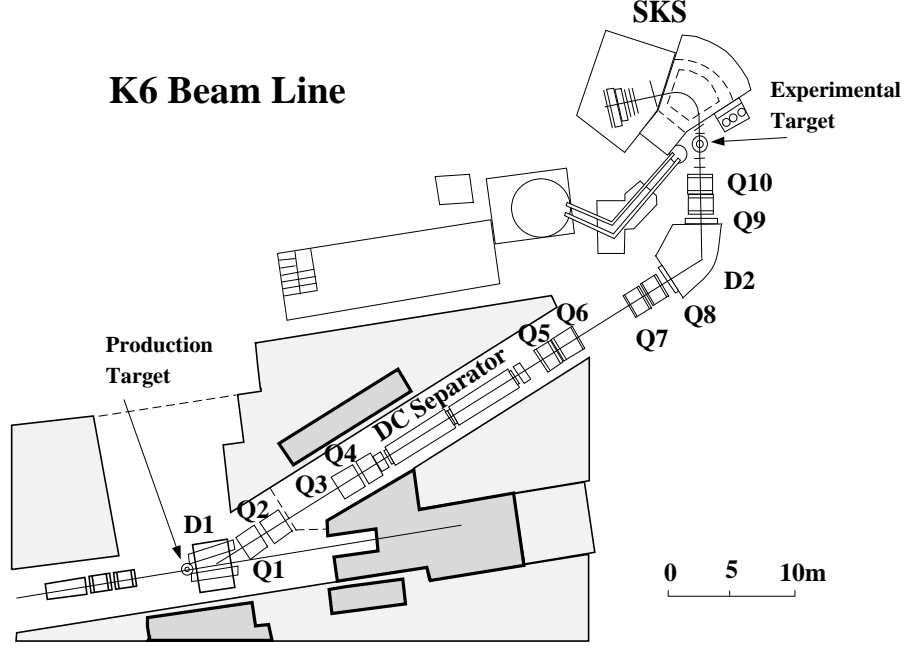


Figure 2.1: Schematic view of the K6 beam line of KEK 12-GeV PS

Table 2.1: Design specifications of the K6 beam-spectrometer system.

Momentum resolution	0.1% FWHM
Momentum bite	$\pm 3\%$
Maximum momentum	1.1 GeV/ $c$
Bending angle	60°

Figure 2.1 shows a schematic view of the K6 beam line. The beam line consists of two dipole magnets (D1, D2), ten quadrupole magnets (Q1-Q10), a sextupole magnet (SX), an electrostatic separator (DC separator) with two correction magnets (CM1, CM2), and four slits. The slits are installed between D1 and Q1 (acceptance slit), between Q2 and Q3 (intermediate focus slit), between SX and Q5 (momentum slit), and between Q6 and Q7 (mass slit).

At the experimental target, the intensity of  $\pi^-$  beam was typically  $1.1 \times 10^6$ /spill for primary protons of  $2.2 \times 10^{12}$ /spill, and the beam size was typically 6.3 mm in the horizontal direction and 13.0 mm in the vertical direction.

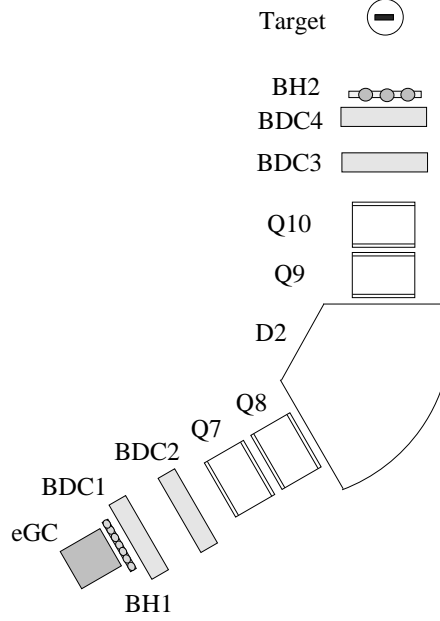


Figure 2.2: Schematic view of the beam spectrometer.

## 2.3 Beam spectrometer

The beam spectrometer comprises a QQDQQ magnet system, four sets of beam drift chambers (BDC1-4), two beam hodoscopes (BH1,2), and a Freon-gas Čerenkov counter (eGC) as shown in Figure 2.2. Design specifications of the spectrometer are listed in Table 2.1.

Beam momentum is measured particle by particle using a third-order transport matrix. In order to minimize multiple-scattering effects on the momentum resolution, the  $\langle x|\theta \rangle$  term of the transport matrix is tuned to be zero, the beam pipe in the QQDQQ system is evacuated, and the tracking drift chambers were made as thin as possible in substance.

### *Tracking chambers*

Specifications of the drift chambers are listed in Table 2.2. The beam drift chambers have a sense-wire spacing of 5 mm, so that they can handle a maximum counting rate of up to several M/spill. Each chamber has six layers of sense-wire planes ( $xx'uu'vv'$ ), where vertical and  $\pm 15^\circ$  tilted-wire planes are denoted by  $x$ ,  $u$ , and  $v$ . In each pair plane ( $xx'$ ,  $uu'$ , and  $vv'$ ), the sense-wire position is shifted by a half of a cell size 2.5 mm in order to solve left/right ambiguity. The sense wire is a gold-plated  $12.5 \mu\text{m}$  tungsten wire and the field wire is a gold-plated  $75 \mu\text{m}$  copper-beryllium wire. The cathode planes are made of  $7.5 \mu\text{m}$  Kapton, both sides of which are coated with  $0.1 \mu\text{m}$  aluminum and 2.5 nm chromium. A gas mixture of Ar:C<sub>4</sub>H<sub>10</sub>:Methylal = 76:20:4 is used at atmospheric pressure.

Table 2.2: Specifications of the drift chambers.

Name	Area (cm)	Drift space (mm)	Wires	Resolution ( $\mu\text{m}$ in r.m.s.)
BDC1–4	$24^{\text{W}} \times 15^{\text{H}}$	2.5	$xx'uu'vv'$	300
SDC1	$40^{\text{W}} \times 15^{\text{H}}$	2.5	$xx'uu'vv'$	300
SDC2	$56^{\text{W}} \times 15^{\text{H}}$	2.5	$xx'uu'$	300
SDC3X	$100^{\text{W}} \times 100^{\text{H}}$	21	$xx'$	300
SDC3Y	$100^{\text{W}} \times 100^{\text{H}}$	21	$yy'$	300
SDC4X	$100^{\text{W}} \times 100^{\text{H}}$	21	$x \times 6$	250
SDC4Y	$100^{\text{W}} \times 100^{\text{H}}$	21	$y \times 6$	250

Table 2.3: Specifications of the trigger counters.

Name	Sensitive area (cm)	PMT (Hamamatsu)	etc.
eGC	$\phi 20 \times 29^{\text{L}}$	R1584-02 $\times$ 1	Freon-12, n=1.00245
BH1	$19^{\text{W}} \times 9^{\text{H}} \times 0.5^{\text{T}}$	R1450 $\times$ 14	7-segments, 3-stage-booster
BH2	$9^{\text{W}} \times 10^{\text{H}} \times 0.3^{\text{T}}$	H5010 $\times$ 6	3-segments, 3-stage-booster
TOF	$105^{\text{W}} \times 100^{\text{H}} \times 3^{\text{T}}$	H1949 $\times$ 30	15-segments
AC1	$105^{\text{W}} \times 120^{\text{H}} \times 9^{\text{T}}$	R1584-02 $\times$ 18	n=1.06, not used
AC2	$140^{\text{W}} \times 140^{\text{H}} \times 12^{\text{T}}$	R1584-02 $\times$ 20	n=1.06, not used
LC	$140^{\text{W}} \times 140^{\text{H}} \times 4^{\text{T}}$	H1949 $\times$ 28	14-segments, n=1.49

### *Beam hodoscopes and the gas Čerenkov counter*

Specifications of the beam hodoscopes and the gas Čerenkov counter are listed in Table 2.3.

BH1 is located upstream of BDC1. It is segmented into seven vertical pieces of 5mm-thick plastic scintillator in order to reduce the single-counting rate. BH2 is located 57 cm upstream of the experimental target to define the beam hitting the target. It is segmented into three vertical pieces of 3mm-thick plastic scintillator. It is also used as the time-zero counter. Each segment is equipped with phototubes having three-stage booster on both ends. A coincidence of BH1 with BH2 rejects background particles which cannot pass through the QQDQQ system.

eGC is located upstream of BH1 to reject electrons (positrons) in the beam. The rejection efficiency is better than 99.9%.



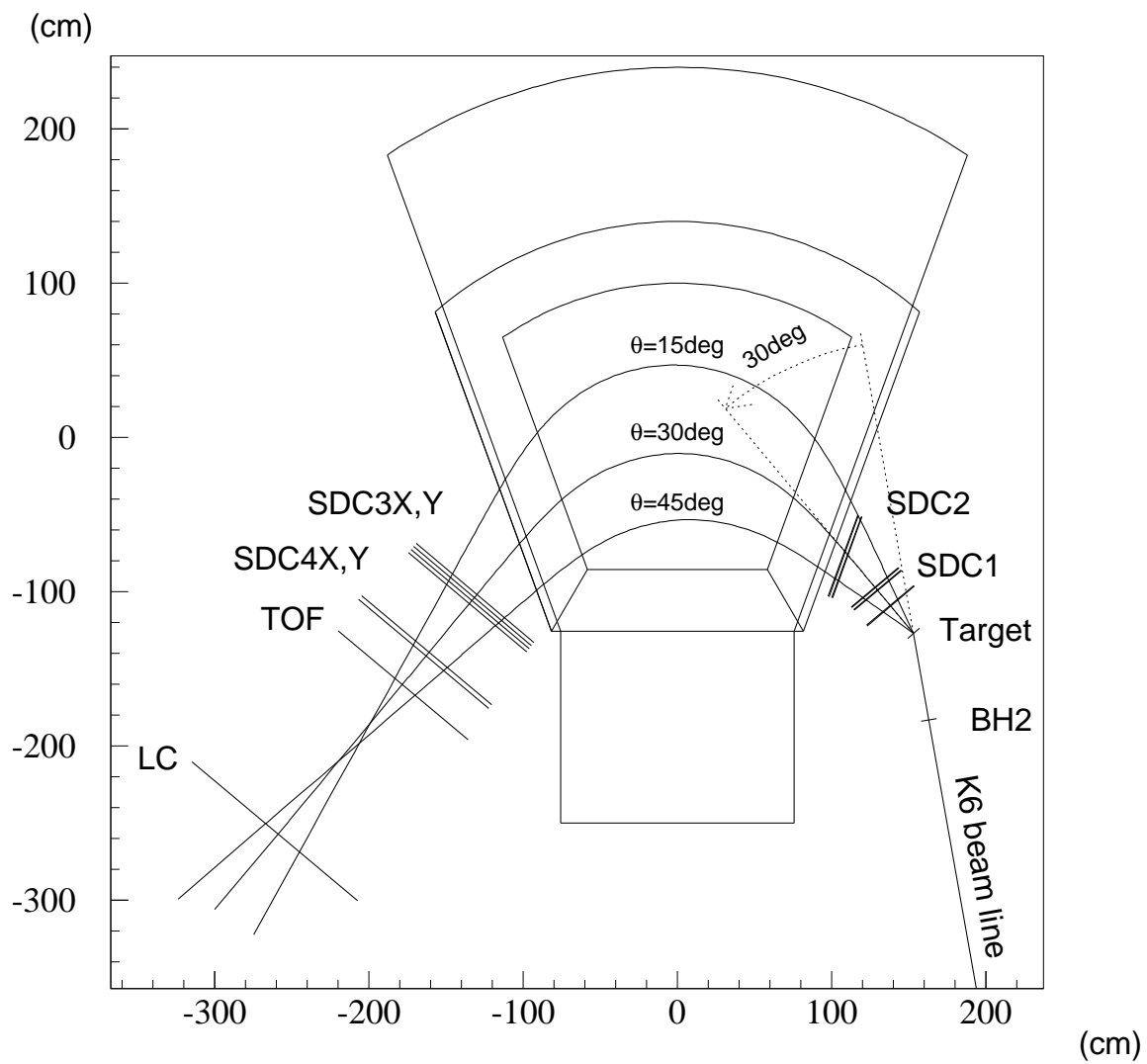


Figure 2.3: Schematic top view of the SKS.

Table 2.4: Design parameters of the SKS.

Momentum resolution	0.1% FWHM at 720 MeV/ $c$
Maximum central momentum	1.1 GeV/ $c$
Momentum bite	$\pm 10\%$
Bending angle	100° for the central trajectory
Solid angle	100 msr
Flight path	$\sim 5$ m for the central trajectory

Table 2.5: Parameters of the SKS magnet.

Maximum magnetic field	3 T
Stored energy	10.6 MJ
Pole gap	49.75 cm
Conductor	NbTi/Cu
Ampere turns	2.1 MA·T
Maximum current	500 A
Total Weight	280 t
Heat leak at 4 K	5 W
Content of Liquid He	156 $\ell$

## 2.4 Scattered-particle spectrometer (SKS)

Figure 2.3 shows schematic top view of the SKS. The SKS comprises a superconducting dipole magnet with six sets of drift chambers (SDC1, SDC2, SDC3X, SDC3Y, SDC4X, and SDC4Y) for momentum reconstruction and three kinds of trigger counters for particle identification: a scintillator wall (TOF), two sets of silica aerogel Čerenkov counters (AC1 and AC2), and a lucite Čerenkov counter wall (LC). To measure wide-angular distributions, the SKS can be rotated around the experimental target from  $-10^\circ$  to  $40^\circ$  with respect to the beam line.

In order to realize a large acceptance and a good momentum resolution, a sector-type superconducting magnet with a pole gap of 50 cm and a maximum magnetic field of 3 T was adopted. Unlike conventional high-resolution spectrometers used in nuclear physics, the SKS has no well-defined focal plane. The parameters of the SKS magnet are listed in Table 2.5.

Specifications of the drift chambers are listed in Table 2.2. SDC1 and SDC2 are located at the entrance of the magnet. They have the same drift-cell structure as the BDC's and the high-rate capability. SDC3X, SDC3Y, SDC4X, and SDC4Y are located at the exit of the magnet. They have a large drift space of 21 mm. SDC4X and SDC4Y have six anode planes. In each cell, the sense wires are staggered by

$\pm 200 \mu\text{m}$  in order to solve left/right ambiguity. The sense wire is a gold-plated  $20 \mu\text{m}$  tungsten wire and the field wire is a gold-plated  $80 \mu\text{m}$  aluminum wire. A gas mixture of  $\text{Ar}:\text{C}_2\text{H}_6 = 50:50$  at atmospheric pressure is used. In order to reduce the effects of multiple scattering, the space along the particle trajectories between SDC1 and SDC4Y are filled with He bags.

Table 2.3 shows the specifications of the trigger counters. In the trigger, a combination of three kinds of counters selects  $\pi$ ,  $K$ , and  $p$ ; TOF is sensitive to charged particles; AC1 and AC2 are sensitive only to  $\pi$ ; LC is insensitive to protons. These counters were prepared for the  $(\pi^+, K^+)$  measurements. Since we measured pions, AC's were not used in the present experiment.

TOF is placed behind SDC4Y. It comprises 15 vertical segments of plastic scintillator of  $7 \times 100 \times 3 \text{ cm}^3$ . 2" phototubes (Hamamatsu-H1949) are attached on the both ends of each segment.

LC is placed behind AC2. It comprises 14 vertical segments of lucite counters of  $10 \times 140 \times 4 \text{ cm}^3$ . A wave-length shifter of bis-MSB was mixed by 10 ppm in weight in the lucite radiator in order to enhance the detection efficiency ( $99.8 \pm 0.2\%$ ) for pions and kaons with various incident angles. Protons slower than  $850 \text{ MeV}/c$  are mostly rejected because of the Čerenkov light threshold.

## 2.5 Trigger and data-acquisition system

Figure 2.4 shows a trigger logic diagram. A beam trigger (**BEAM**) was defined as  $\text{BH1} \times \text{BH2} \times \overline{\text{eGC}}$ . A pion trigger ( $\pi$ ) was defined as  $\text{BEAM} \times \text{TOF} \times \text{LC} \times \overline{\text{VETO}}$ . Mean timer modules (MT) were used in the counters which have two PMT's at both ends so as to remove the incident-position dependence of the timing.

Timing of an event trigger (**Trigger**) was determined by **BH2**; after the trigger selection logic, a coincidence of **BH2** and the selected trigger was taken. **Trigger** gave the STOP timing for the drift chamber TDC of BDC's, SDC1, and SDC2. For SDC3X, SDC3Y, SDC4X, and SDC4Y, however, **TOF** gave the STOP timing. Because a flight time from BH2 to the exit of SKS varies according to the flight-path and momentum of the particle.

A diagram of the data-acquisition system is shown in Figure 2.5. Most of the signals from the detectors are digitized with TDC and ADC modules in the TKO boxes. The TKO is a standard developed at KEK.

In a VME box, six VME-MP's (Memory Partner) are installed. The VME-MP is an interface module between a TKO bus and a VME bus, and has a local memory which can be accessed by a CPU module. During a beam spill on, event triggers are fed into the ACCEPT input of the VME-MP's. Then the VME-MP's read out the data of the TDC and ADC modules and store them into its local memories. At the spill-end, the stored data are read out by the CPU module (MC-68020) on which OS-9 works. The CAMAC scalers in one crate are also read out via a VME-CAMAC interface (CES-8216) connected to a K3922 CAMAC crate



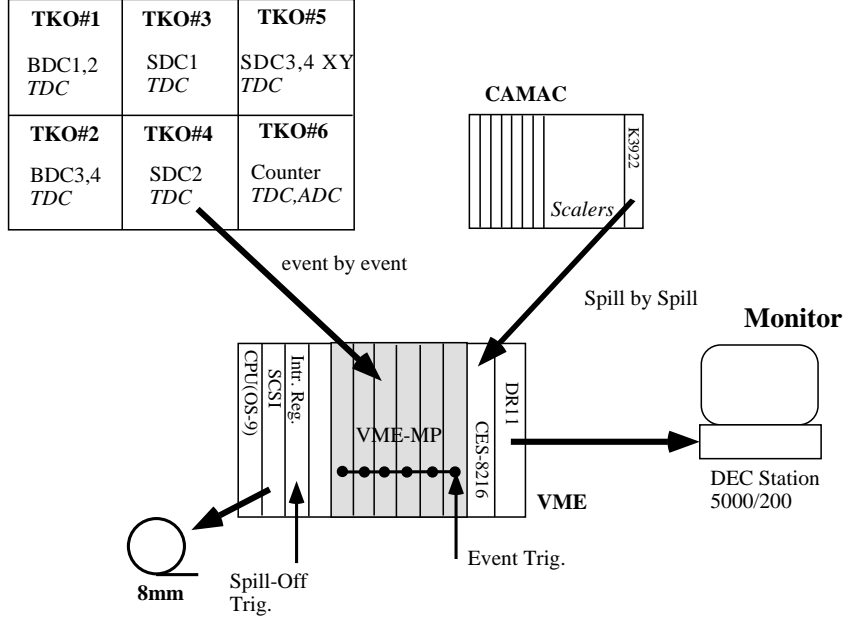


Figure 2.5: Diagram of the data-acquisition system.

of chambers. The VETO counter was positioned between SDC1 and SDC2. It rejected particles with scattering angle of smaller than about  $17^\circ$ .

Three or four spectrometer momentum settings were used to cover entire quasielastic peak with a sufficient overlap. We called these settings 210A, 272A, 320A, and 395A mode according to their current settings. The energy loss range up to 350 MeV was covered by these settings.

The quasielastic kinematics and the coverage of the present setup are shown in Figure 2.6. The thin solid line shows the region covered by the present setup. The  $q$ -fixed loci are shown in the dashed lines. The thick solid line shows kinematics of a quasielastic peak and the dotted lines show full width of a quasielastic peak calculated with a Fermi-gas model.

In addition, targets were positioned to be parallel to SDC1, namely, to make an angle of  $30^\circ$  with the beam line.

## 2.7 Run summary

The present experiment (KEK-PS E352) was performed for two periods of time, for 11 days in November 1995 (Nov95 runs) and for 7 days in February 1996 (Feb96 runs). The total number of pions is  $2.05 \times 10^{11}$ , the total number of triggers is  $7.43 \times 10^7$ , and the size of the raw data is about 35 Gbytes. The targets used for the experiment are listed in Table 2.6. Total number of irradiated pions for each target and SKS setup is listed in Table 2.7.

Table 2.6: All the targets used in the present experiment.

target	thickness	description
CH <sub>2</sub>	3.50 g/cm <sup>2</sup>	polyethylene
CD <sub>2</sub>	1.43 g/cm <sup>2</sup>	deuterated polyethylene
<sup>6</sup> LiD	2.02 g/cm <sup>2</sup>	contained in polyethylene bag
C	4.58 g/cm <sup>2</sup>	natural
Ca	3.09 g/cm <sup>2</sup>	natural, covered by thin Al foil
Zr	3.39 g/cm <sup>2</sup>	natural
<sup>208</sup> Pb	4.62 g/cm <sup>2</sup>	isotopically enriched to 99%

Table 2.7: Total number of irradiated  $\pi^-$  for each target and SKS setup.

target	395A mode (860 MeV/c)*	320A mode (780 MeV/c)*	272A mode (720 MeV/c)*	210A mode (630 MeV/c)*
CD <sub>2</sub>	$5.58 \times 10^9$	$4.44 \times 10^9$	$3.01 \times 10^9$	-
<sup>6</sup> LiD	$5.47 \times 10^9$	$4.27 \times 10^9$	$3.98 \times 10^9$	$0.81 \times 10^9$
C	$6.14 \times 10^9$	$4.73 \times 10^9$	$4.37 \times 10^9$	$2.62 \times 10^9$
Ca	$7.91 \times 10^9$	$5.92 \times 10^9$	$5.63 \times 10^9$	-
Zr	$3.82 \times 10^9$	$2.29 \times 10^9$	$2.60 \times 10^9$	-
<sup>208</sup> Pb	$7.73 \times 10^9$	$4.21 \times 10^9$	$5.30 \times 10^9$	$1.11 \times 10^9$

\* Central momentum

For an extensive study of the acceptance of the SKS,  $\pi^-$ -p elastic data as well as quasielastic data were taken. We devoted 30% of the total beam to this study, because the acceptance is most important for the present experiment. Total number of pions for each setup is listed in Table 2.8.

In addition to these data, we took beam trigger data, no-VETO data, and empty target data. The beam trigger data, 1/200K of all the beam triggers, were simultaneously taken with normal (pion trigger) data for every run to know the information of the beam line without pion trigger bias. The no-VETO data were taken without **VETO** in the pion trigger to check the VETO scintillator gave no distortion on a quasielastic peak shape. The empty target data were taken to check experimental backgrounds.

Table 2.8: Total number of  $\pi^-$  for the acceptance study.

target	$P_{beam}$ (MeV/c)	395A mode (860 MeV/c)*	320A mode (780 MeV/c)*	272A mode (720 MeV/c)*	210A mode (630 MeV/c)*
CH <sub>2</sub>	700	-	-	-	$1.18 \times 10^9$
	730	-	-	$0.32 \times 10^9$	-
	780	-	$3.34 \times 10^9$	$3.17 \times 10^9$	-
	850	$0.36 \times 10^9$	$2.95 \times 10^9$	$3.52 \times 10^9$	-
	900	$3.11 \times 10^9$	-	-	-
	950	$7.79 \times 10^9$	$5.53 \times 10^9$	$4.19 \times 10^9$	-
	1000	$5.70 \times 10^9$	$2.03 \times 10^9$	-	-
	1050	$3.86 \times 10^9$	-	-	-
	1100	$3.98 \times 10^9$	-	-	-
C	700	-	-	-	$1.19 \times 10^9$
	730	-	-	$0.17 \times 10^9$	-
	780	-	$1.78 \times 10^9$	$2.23 \times 10^9$	-
	850	$3.56 \times 10^9$	$5.62 \times 10^9$	$4.42 \times 10^9$	-
	900	$3.10 \times 10^9$	-	-	-
	1000	$5.87 \times 10^9$	$0.81 \times 10^9$	-	-
	1050	$3.81 \times 10^9$	-	-	-
	1100	$1.39 \times 10^9$	-	-	-

\* Central momentum

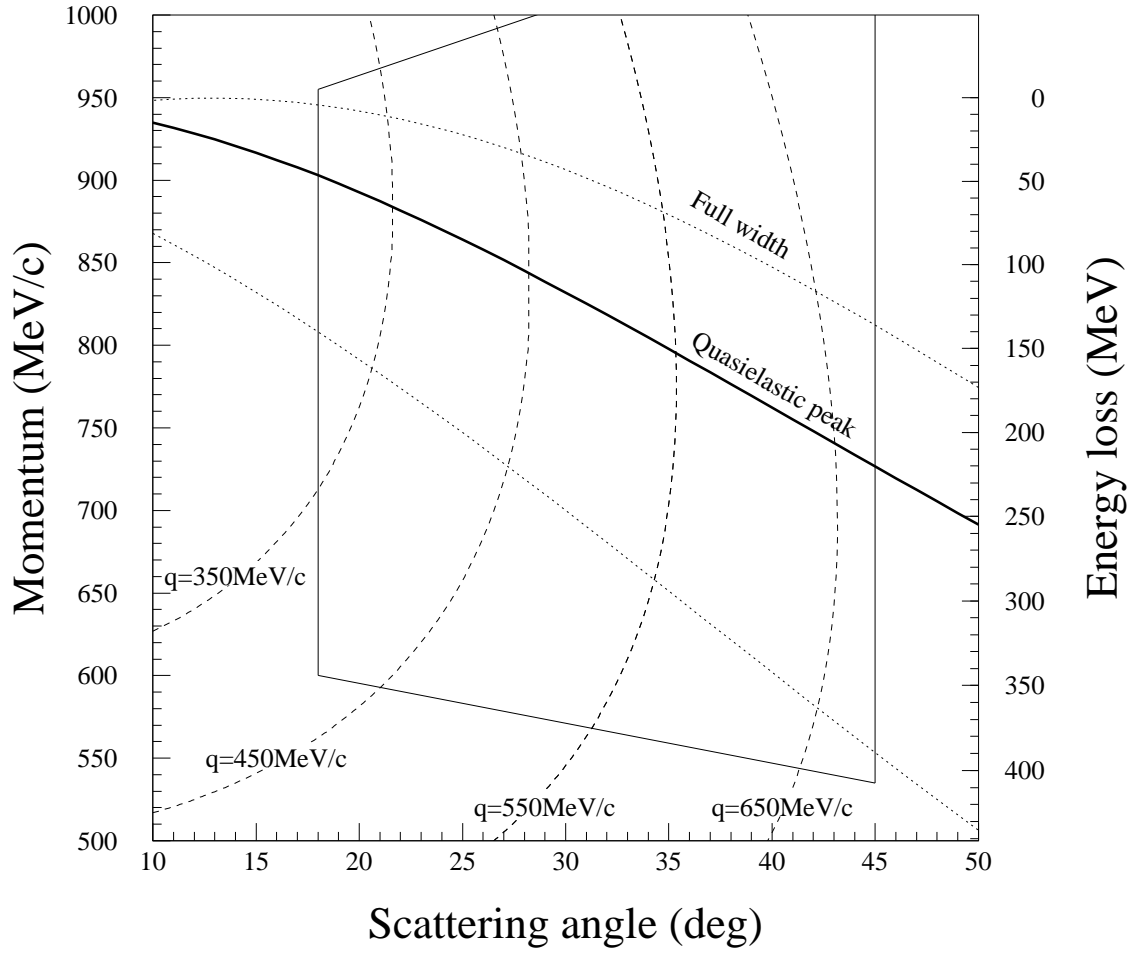


Figure 2.6: Coverage of the present setup. The thin solid line shows the region covered by the present setup. The  $q$ -fixed loci are shown in the dashed lines. The thick solid line shows kinematics of a quasielastic peak and the dotted lines show full width of a quasielastic peak calculated with a Fermi-gas model.



# Chapter 3

## Data Analysis

### 3.1 Outline

In this chapter, procedures to calculate the doubly differential cross sections from the raw data are described. The doubly differential cross sections are obtained as a function of momentum transfer  $q$  and energy loss  $\omega$ . The energy loss is defined here as the difference between initial and final laboratory kinetic energies of a pion.

Figure 3.1 shows a flow chart of off-line analysis program in this work. First, TDC and ADC data for the trigger hodoscopes (BH1, BH2, TOF, and LC) are checked. Next, tracks at the entrance and exit of the SKS are obtained from the SDC data. In section 3.2, beam momentum is calculated from BDC data as described. The momentum of a scattered particle is calculated by reconstructing a trajectory as described in section 3.3. Next, a vertex cut is applied as shown in section 3.4. Finally, the doubly differential cross sections are obtained as described in section 3.5. The procedures to derive the effective solid angle of the SKS and efficiencies are also discussed. These are most important points in the present analysis for extraction of reliable shape and absolute cross section of the quasielastic peak.

### 3.2 Momentum of beam particle

The beam momentum was calculated from the BDC data as follows. First, a straight track was defined locally at the entrance and exit of the QQDQQ magnet system by BDC1·2 and BDC3·4, respectively. Next, the tracks at the entrance and exit of the QQDQQ were connected using a 3rd-order transport matrix, and the momentum was calculated. For a multi-track event, only one combination which gave the least  $\chi^2$  was chosen. The transport matrix was calculated with the code ORBIT [20].

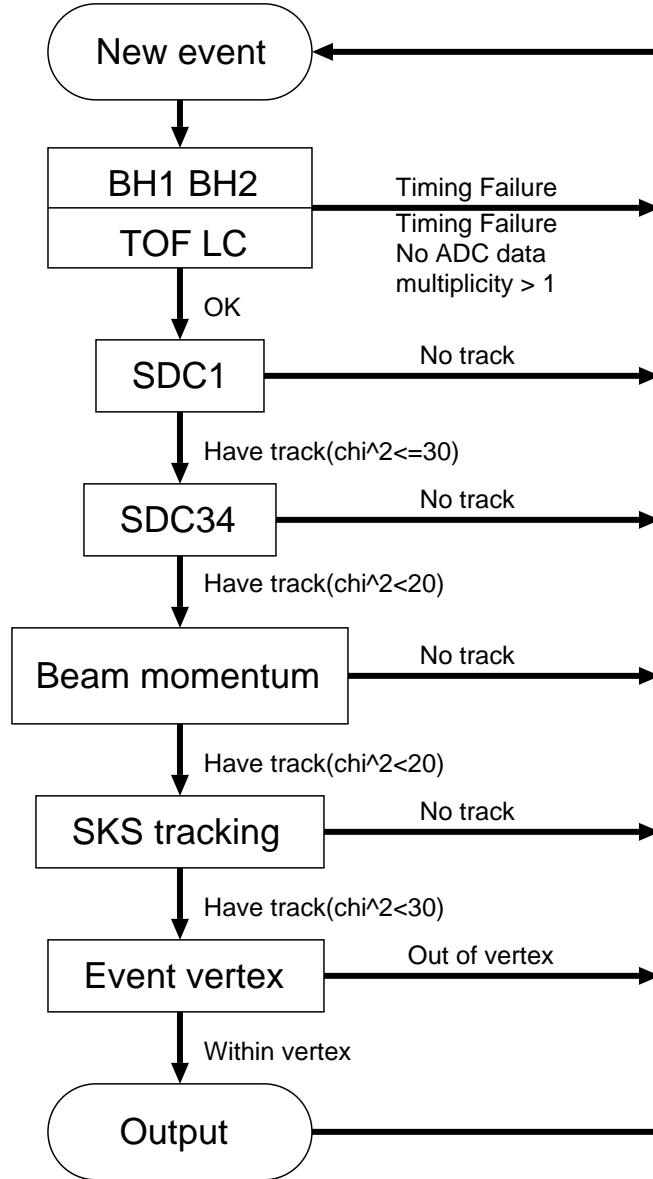


Figure 3.1: Flow chart of offline analysis program in this work.

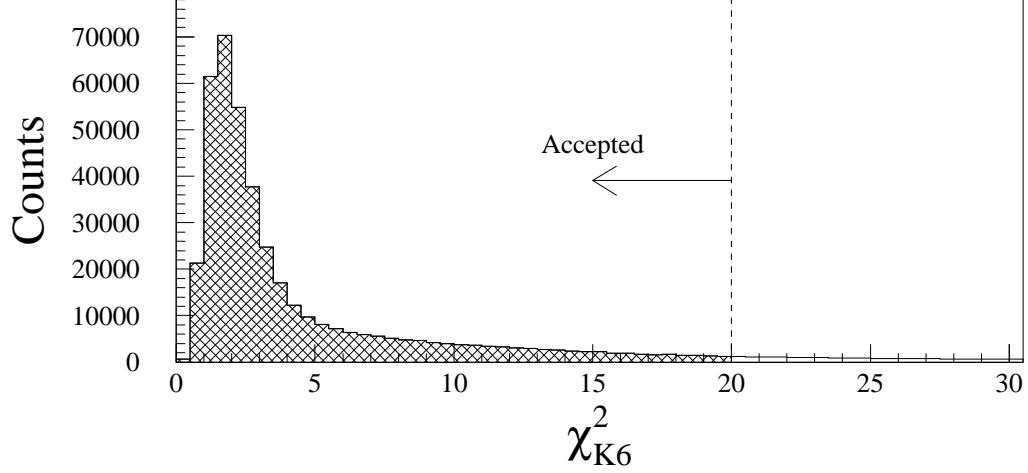


Figure 3.2: Typical distribution of  $\chi_{K6}^2$ . A cut of  $\chi_{K6}^2 < 20$  is applied.

The  $\chi^2$  of the tracking is defined as

$$\chi_{K6}^2 \equiv \frac{1}{n-5} \left( \sum_{i=1}^{12} H_i \left( \frac{P_i - f_i(\vec{X}_{in})}{w_i} \right)^2 + \sum_{i=13}^{24} H_i \left( \frac{P_i - g_i(\vec{X}_{out})}{w_i} \right)^2 \right), \quad (3.1)$$

$$n = \sum_{i=1}^{24} H_i, \quad (3.2)$$

$$H_i = \begin{cases} 1 & \text{if } i\text{th plane has a hit,} \\ 0 & \text{if } i\text{th plane has no hit,} \end{cases} \quad (3.3)$$

$$\vec{X}_{out} = \mathcal{M}(\vec{X}_{in}, \delta), \quad (3.4)$$

where  $P_i$  and  $w_i$  denote the hit position and resolution of the  $i$ th plane; for example, 13 – 18 represent the BDC3's planes. The calculated position for the trajectory at the  $i$ th plane is denoted by  $f_i(\vec{X}_{in})$  and  $g_i(\vec{X}_{out})$ ;  $\vec{X}_{in}$  and  $\vec{X}_{out}$  are the vectors at the entrance and exit of the QQDQQ, denoted by the horizontal and vertical positions and their derivatives  $(x, y, \frac{dx}{dz}, \frac{dy}{dz})$ . The particle momentum is denoted by  $p = p_0(1 + \delta)$ , where  $p_0$  is the central momentum. The operator  $\mathcal{M}$  denotes the 3rd-order transport matrix which combines the  $\vec{X}_{in}$  and  $\vec{X}_{out}$ . A typical  $\chi^2$ -distribution is shown in Figure 3.2. The events whose  $\chi^2$  were less than 20 were accepted.

Figure 3.3 shows a distribution of beam momentum. The momentum spread was about 30 MeV/ $c$ .

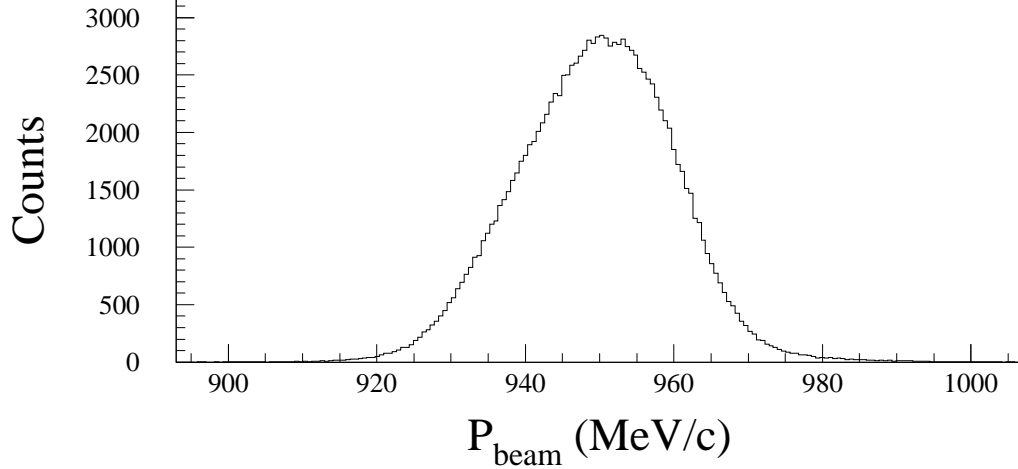


Figure 3.3: Typical distribution of beam momentum.

### 3.3 Momentum of scattered particle

The momentum of a scattered particle was calculated from the SDC data as follows. First, straight tracks at the entrance and exit of SKS were defined locally by SDC1 and SDC3-4, respectively. In finding the SDC1 track, all combinations of left/right ambiguity were examined, because the trajectory to the chamber planes had a large angle and we could not use pair-plane information. For a multi-hit event, all possible combinations were examined and tracks whose  $\chi^2$  were less than 30 were accepted.

Next, the momentum was determined from the hit positions by reconstructing a trajectory. It was reconstructed with a fast Runge-Kutta method [21] using a measured magnetic field map. The field maps were measured at various current settings with an accuracy of  $10^{-4}$  [19]. In this method, five track parameters, position and momentum vector on a starting plane, are optimized iteratively by minimizing the  $\chi^2$  defined as

$$\chi_{\text{SKS}}^2 = \frac{1}{n-5} \sum_{i=1}^n \left( \frac{x_i^{\text{tracking}} - x_i^{\text{data}}}{w_i} \right)^2, \quad (3.5)$$

where  $n$  is the number of the chamber planes with a hit;  $x_i^{\text{tracking}}$  and  $x_i^{\text{data}}$  are the hit positions on the  $i$ th plane in the tracking and the data, respectively;  $w_i$  is the position resolution of the  $i$ th plane. In this method, the derivatives, which are required to guess the trajectory in the next iteration, are computed together with the track coordinates themselves. The convergence criterion in the iteration is that the variation of  $\chi^2$  is less than 20% ( $\delta\chi^2 = (\chi_{k+1}^2 - \chi_k^2)/\chi_k^2 < 0.2$ ) and the divergence criterion is  $k > 40$ . For a multi-track event, all possible combinations were examined and only the track which gave the least  $\chi^2$ -value was chosen. Figure

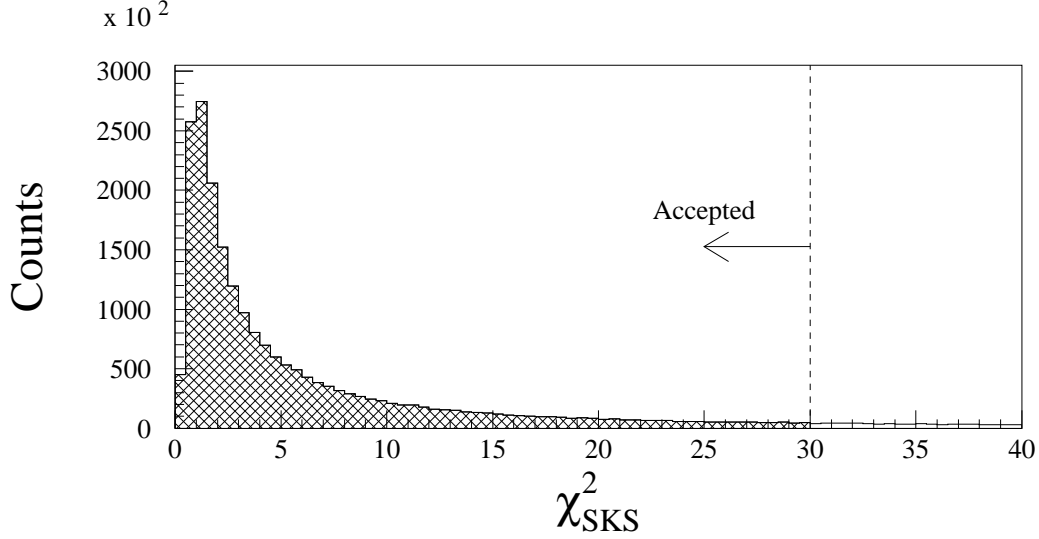


Figure 3.4: Typical distribution of  $\chi^2_{\text{SKS}}$ . A cut of  $\chi^2_{\text{SKS}} < 30$  was applied in the present analysis.

3.4 shows a typical  $\chi^2$ -distribution. A cut of  $\chi^2_{\text{SKS}} < 30$  was applied in the present analysis.

In addition, calculated flight time of a scattered particle was compared with the TDC data of TOF counter. No particles other than  $\pi^-$  were seen as expected.

### 3.4 Event vertex

The scattering angle and event vertex were determined by two trajectories: the local straight track by BDC3·4 and the track determined by the momentum reconstruction of the scattered particle. The scattering-angle resolution is about  $1^\circ$ , deduced from the energy resolution difference between  $\pi^-$ - $^{12}\text{C}$  and  $\pi^-$ -p elastic scattering peaks.

Figure 3.5 shows a Z-projection of the event vertex; Z-axis is defined to be perpendicular to the target plane. The events scattered at the target and BH2 are clearly distinguished. The shadowed histogram shows the background events measured with no target. The vertex-cut was applied in the analysis in order to reject them. The hatched area shows an accepted region.

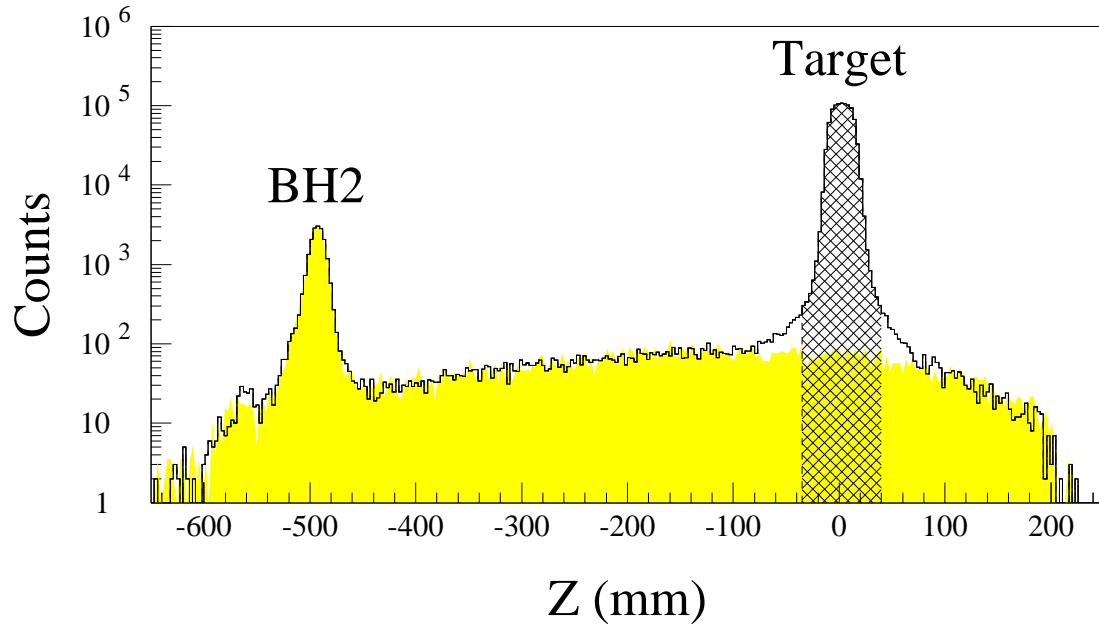


Figure 3.5: Z-projection of the event vertex for the carbon target. The events scattered at the target and BH2 are clearly distinguished. The hatched area shows an accepted region. The shadowed histogram shows the background events measured with no target.

### 3.5 Doubly differential cross sections

The doubly differential cross sections were calculated from the data according to the following expression.

$$\frac{d^2\sigma}{d\Omega d\omega}(q, \omega) = \sum_i b(q^i, \omega^i) \cdot \frac{1}{N_{tgt} \cdot N_{beam}} \cdot \frac{1}{\Delta\Omega_{\text{eff}}(q^i, p^i)} \cdot \frac{1}{\Delta\omega} \cdot \frac{1}{\varepsilon(\vec{X}_{in}^i)}, \quad (3.6)$$

$$b(q^i, \omega^i) = \begin{cases} 1 & \text{if } \omega - \frac{1}{2}\Delta\omega \leq \omega^i < \omega + \frac{1}{2}\Delta\omega \\ & \text{and } q - \frac{1}{2}\Delta q \leq q^i < q + \frac{1}{2}\Delta q, \\ 0 & \text{otherwise,} \end{cases} \quad (3.7)$$

$$\varepsilon(\vec{X}_{in}^i) = \varepsilon_{K6} \cdot \varepsilon_{DAQ} \cdot \varepsilon_{SDC1}(\vec{X}_{in}^i) \cdot \varepsilon_{tracking}(\vec{X}_{in}^i) \cdot \varepsilon_{norm}, \quad (3.8)$$

where  $i$  denotes each event and the summation runs over all the events. Meaning of the variables is the following:

- $b(q^i, \omega^i)$  : Factor to select a bin. 1, if the event is in the  $(q, \omega)$  bin; 0, otherwise;
- $\Delta\omega$  : Bin size for the  $\omega$  axis;
- $\Delta q$  : Bin size for the  $q$  axis;
- $N_{tgt}$  : Number of target nucleus per unit area;
- $N_{beam}$  : Scaler count of the beam trigger (**BEAM**);
- $\vec{X}_{in}^i$  : Reconstructed vector at the target;
- $\Delta\Omega_{\text{eff}}(q^i, p^i)$  : Effective solid angle of the SKS for a momentum transfer  $q^i$  and momentum of scattered pion  $p^i$ ;
- $\varepsilon(\vec{X}_{in}^i)$  : Overall normalization factor.

See the following subsection for the effective solid angle. The definition of the normalization factors is described in subsection 3.5.2.

Energy loss of incident and scattered pions on experimental target is calculated and corrected with the Bethe-Bloch formula. The energy loss correction ranges from 1.5 to 4 MeV, mostly depends on a target thickness.

### 3.5.1 Effective solid angle

The effective solid angle as a function of scattering angle  $\theta$  and momentum  $p$  was calculated with a Monte-Carlo simulation code. The effect of pion decay was included in the code. Beam events were generated so as to reproduce the experimental beam profile. Scattered particle events were generated uniformly from  $\theta - \frac{1}{2}\Delta\theta$  to  $\theta + \frac{1}{2}\Delta\theta$  with respect to the polar angle, from 0 to  $2\pi$  with respect to the azimuthal angle, and from  $p - \frac{1}{2}\Delta p$  to  $p + \frac{1}{2}\Delta p$  with respect to the momentum. The effective solid angle was calculated using

$$\Delta\Omega_{\text{eff}}(\theta, p) = \left( 2\pi \int_{\theta - \frac{1}{2}\Delta\theta}^{\theta + \frac{1}{2}\Delta\theta} \sin\theta d\theta \right) \times \frac{\text{number of events accepted}}{\text{number of events generated}}. \quad (3.9)$$

The result for the 395A mode is shown in Figure 3.6. Detailed discussion of the effective solid angle is given in Appendix A.

### 3.5.2 Efficiencies

Data were normalized to the free  $\pi^-$ -p scattering cross sections determined by the SM95 solution incorporated in the program SAID [22]. Efficiencies for beam line spectrometer, data acquisition, SDC1 analysis, and momentum reconstruction, however, were explicitly used in the analysis because they showed a position dependence, or changed run by run. Efficiencies and the normalization factor for carbon runs with the 395A mode are listed in Table 3.1. Each efficiency was estimated from the obtained data as follows:

$$\varepsilon = \frac{\text{Number of events accepted in the analysis}}{\text{Number of selected events to be analyzed}}. \quad (3.10)$$

Beam line efficiency ( $\varepsilon_{K6}$ ) was estimated using beam trigger data, which were free from trigger biases.

For estimation of SDC1 efficiency ( $\varepsilon_{SDC1}$ ), events passed through the effective area of SDC1 with scattered from the target were adopted as the denominator of Eq. (3.10). The events were selected using the reconstructed trajectory from the SDC2 and SDC3-4 data. The efficiency of SDC1 showed strong position dependence for the Nov95 runs. It was due to missing wires. A position-dependent efficiency for SDC1 was used in the analysis. For the Feb96 runs, no position dependence was seen, because the missing wires had been repaired.

Tracking efficiency ( $\varepsilon_{\text{tracking}}$ ) showed slight dependence on the incident angle ( $dx/dz$  in the SKS local coordinate).

Other efficiencies and factors, such as the SDC3-4 efficiency and a ratio of muon contamination in the beam, were included in a normalization factor  $\varepsilon_{\text{norm}}$ , because no dependence was observed for the other chambers and trigger counters.



## 395A mode

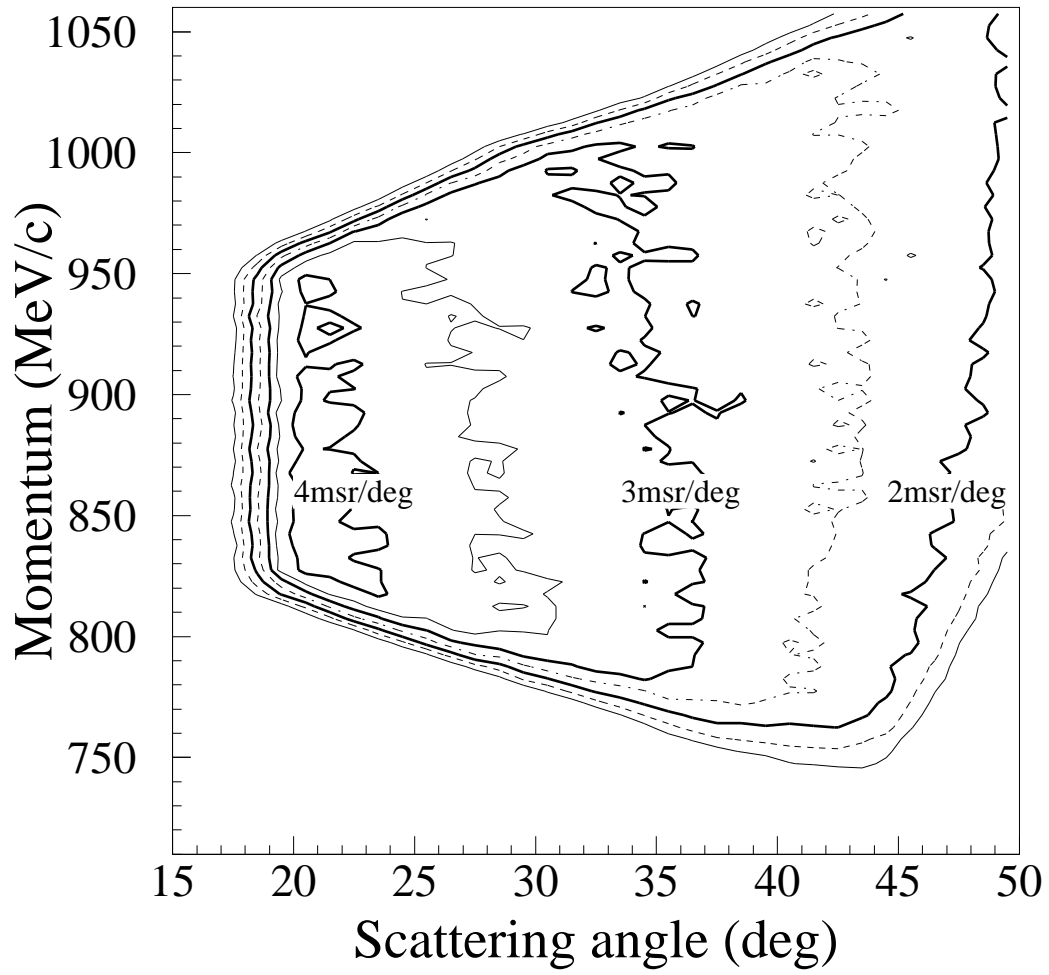


Figure 3.6: Effective solid angle of the SKS for the 395A mode.

Table 3.1: Efficiencies for the carbon runs with the 395A mode.

Factor	Meaning	Typical Value (%)
$\varepsilon_{K6}$	Beam line spectrometer's efficiency	$94.5 \pm 2.1$
$\varepsilon_{DAQ}$	Data acquisition efficiency	$83.5 \pm 0.2$
$\varepsilon_{SDC1}(\vec{X}_{in})$	SDC1 analysis efficiency	$96.0 \pm 3.0$
$\varepsilon_{tracking}(\vec{X}_{in})$	Analysis efficiency of the momentum reconstruction	$96.2 \pm 2.0$
$\varepsilon_{norm}$	Normalization factor	$62.0 \pm 2.9$

This factor was adjusted to reproduce the calculated  $\pi^-$ -p elastic scattering cross sections as mentioned before.

Figure 3.7 shows the differential cross sections for the  $\pi^-$ -p scattering measured with the 395A mode. The solid lines show the results of SAID. The present data agree very well with the calculation.

Systematic error of the effective solid angle was estimated to be  $\pm 7\%$  from ratios of the data from overlapped regions of the different momentum setups. Systematic error of SAID cross sections was assumed to be  $\pm 5\%$ . From these errors, overall normalization uncertainty was estimated to be  $\pm 11\%$ . The error on energy scale was estimated to be  $\pm 2$  MeV.

All experimental data for the  $\pi^-$ -p scattering are shown with the results of SAID in Appendix A.

### 3.5.3 Combination of the different setup spectra

Since three or four spectrometer momentum settings were used to cover an entire quasielastic region as described before, spectra should be combined smoothly into one spectrum. Following is a method to select and combine the data in overlapped regions.

First, ratios of the doubly differential cross sections in the overlapped kinematical region of two settings were taken. Next, a region where the ratios were stable was determined and the data in the region were accepted. Finally, the accepted data in the same  $\omega$  bin were weighted averaged, and a combined spectrum was obtained.

Figure 3.8 shows  $^{12}\text{C}(\pi^-, \pi^-')$ ,  $q = 500$  MeV/ $c$  quasielastic spectra for each SKS mode. The open circles, filled circles, triangles, and asterisks show the data for the 395A, 320A, 272A, and 210A mode, respectively. Figure 3.9 shows the ratios between the overlapped settings. The filled circles show the data in the accepted region, while the open circles show unused data. The error bars are statistical only. The ratios of the cross sections between the overlapped settings agree within  $\pm 7\%$ , which is assumed systematic error.

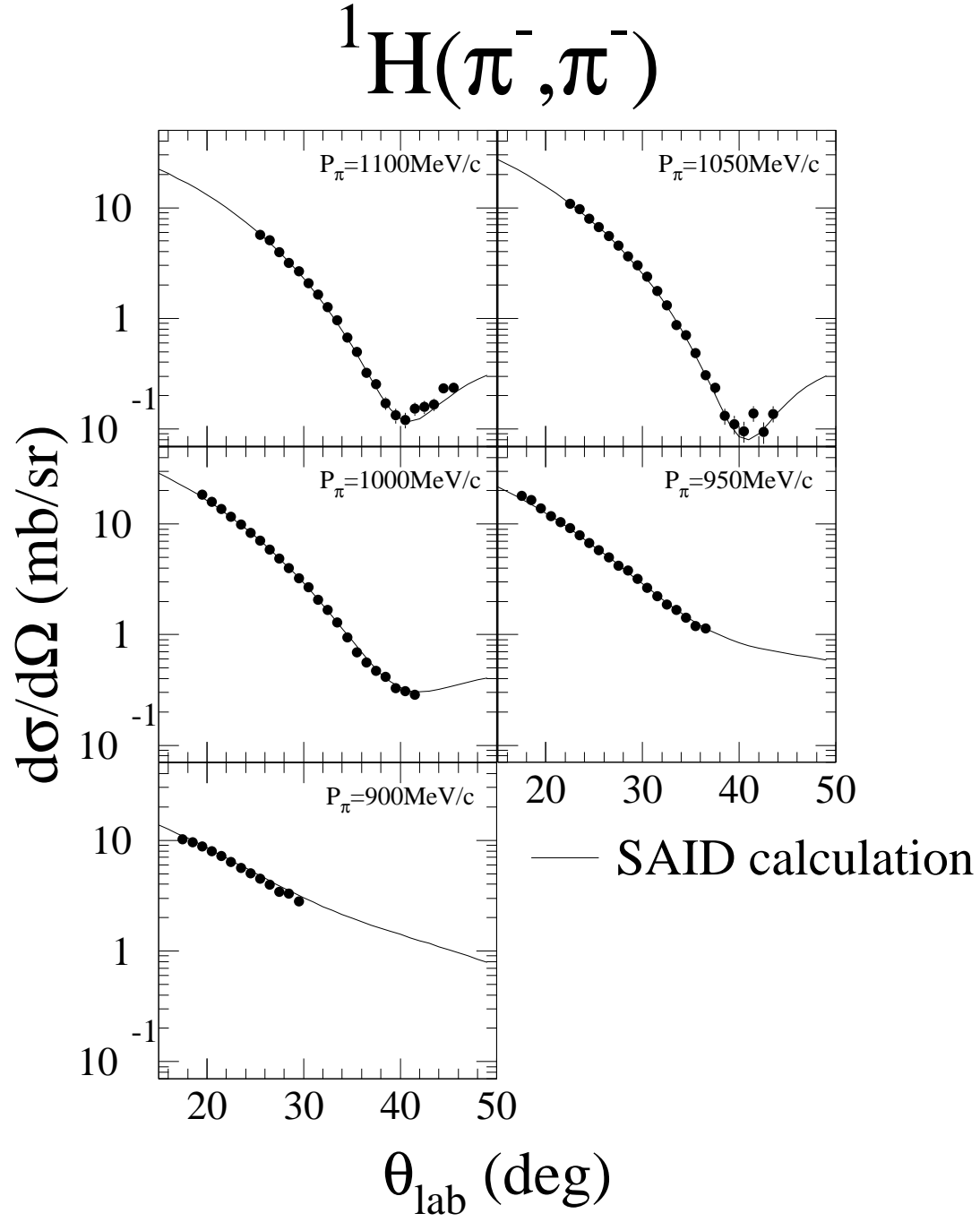


Figure 3.7: Differential cross sections for  $\pi^-$ -p elastic scattering measured with the 395A mode. The solid lines show the results of SAID.

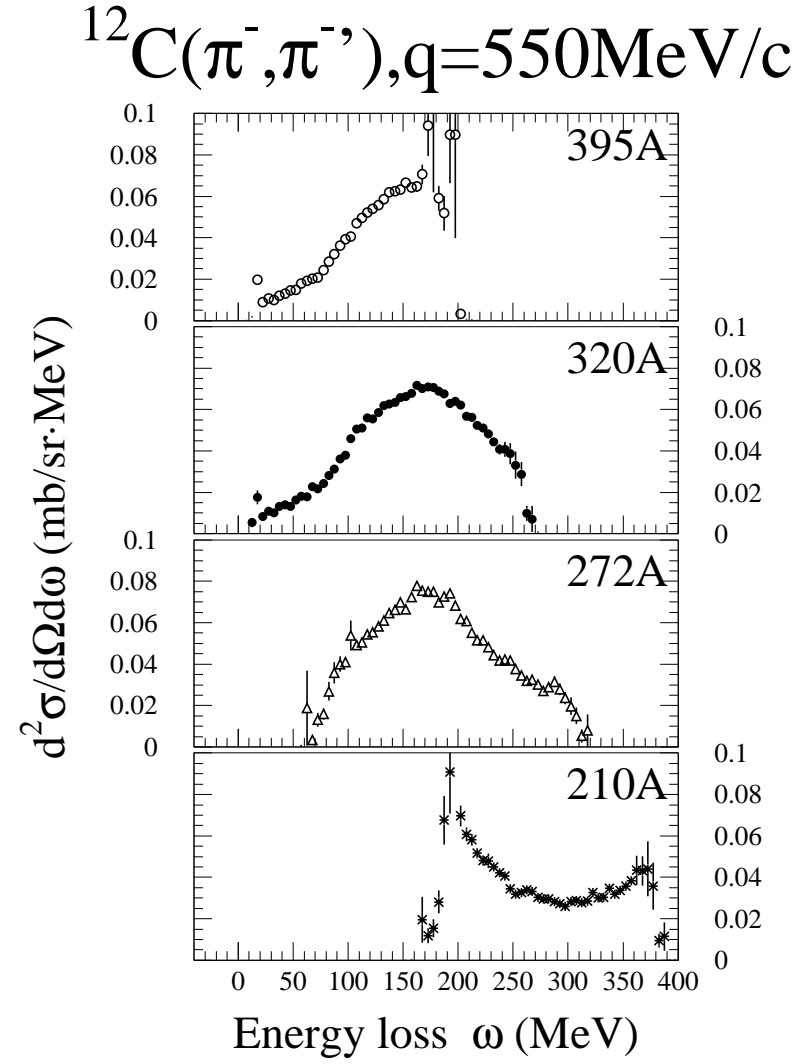


Figure 3.8:  $^{12}\text{C}(\pi^-, \pi^{-'}), q = 550 \text{ MeV}/c$  quasielastic spectra for each SKS mode. The open circles, filled circles, triangles, and asterisks show the data for the 395A, 320A, 272A, and 210A modes, respectively.

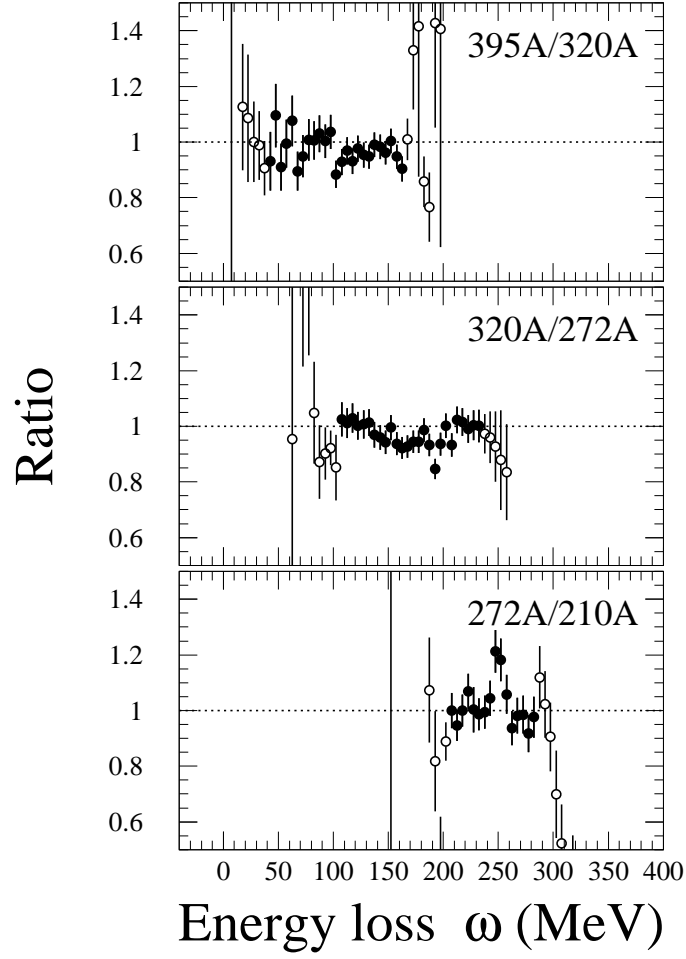


Figure 3.9: Ratios of the doubly differential cross sections in the overlapped region. The filled circles show the data in the accepted region, while the open circles show unused data. The error bars are statistical only.

### 3.5.4 Extraction of D and ${}^6\text{Li}$ spectra

The doubly differential cross sections for p, D, and  ${}^6\text{Li}$  were obtained from the spectra of the C,  $\text{CH}_2$ ,  $\text{CD}_2$ , and  ${}^6\text{LiD}$  target by using:

$$\frac{d^2\sigma^{(\text{p})}}{d\Omega d\omega} = \frac{1}{2} \left( \frac{d^2\sigma^{(\text{CH}_2)}}{d\Omega d\omega} - \frac{d^2\sigma^{(\text{C})}}{d\Omega d\omega} \right), \quad (3.11)$$

$$\frac{d^2\sigma^{(\text{D})}}{d\Omega d\omega} = \frac{1}{2} \left( \frac{d^2\sigma^{(\text{CD}_2)}}{d\Omega d\omega} - \frac{d^2\sigma^{(\text{C})}}{d\Omega d\omega} \right), \quad (3.12)$$

$$\frac{d^2\sigma^{({}^6\text{Li})}}{d\Omega d\omega} = \frac{d^2\sigma^{({}^6\text{LiD})}}{d\Omega d\omega} - \frac{d^2\sigma^{(\text{D})}}{d\Omega d\omega}. \quad (3.13)$$

Figure 3.10 shows the doubly differential cross sections for the  $\text{CD}_2$  and  ${}^6\text{LiD}$  targets at  $q = 400 \text{ MeV}/c$ . The shadowed histogram shows the C (D) spectrum to be subtracted from the  $\text{CD}_2$  ( ${}^6\text{LiD}$ ) spectrum.

Numbers of carbon atoms in the  $\text{CD}_2$  and  $\text{CH}_2$  targets relative to that of C target was deduced from yields of the  $\pi^-$ - ${}^{12}\text{C}$  elastic and inelastic ( $E_x = 4.4 \text{ MeV}$ ) scattering. Relative numbers of deuteron atoms in the  ${}^6\text{LiD}$  and  $\text{CD}_2$  targets was also deduced from yields of the  $\pi^-$ -D elastic scattering. These are consistent with the thicknesses listed in Table 2.6 within  $\pm 3\%$ .

The doubly differential cross sections for calcium show a considerable contribution of hydrogen. Accordingly, oxygen would be contained in the target too. The contributions from hydrogen and oxygen are, however, not subtracted from the calcium spectra here, but taken into account later.

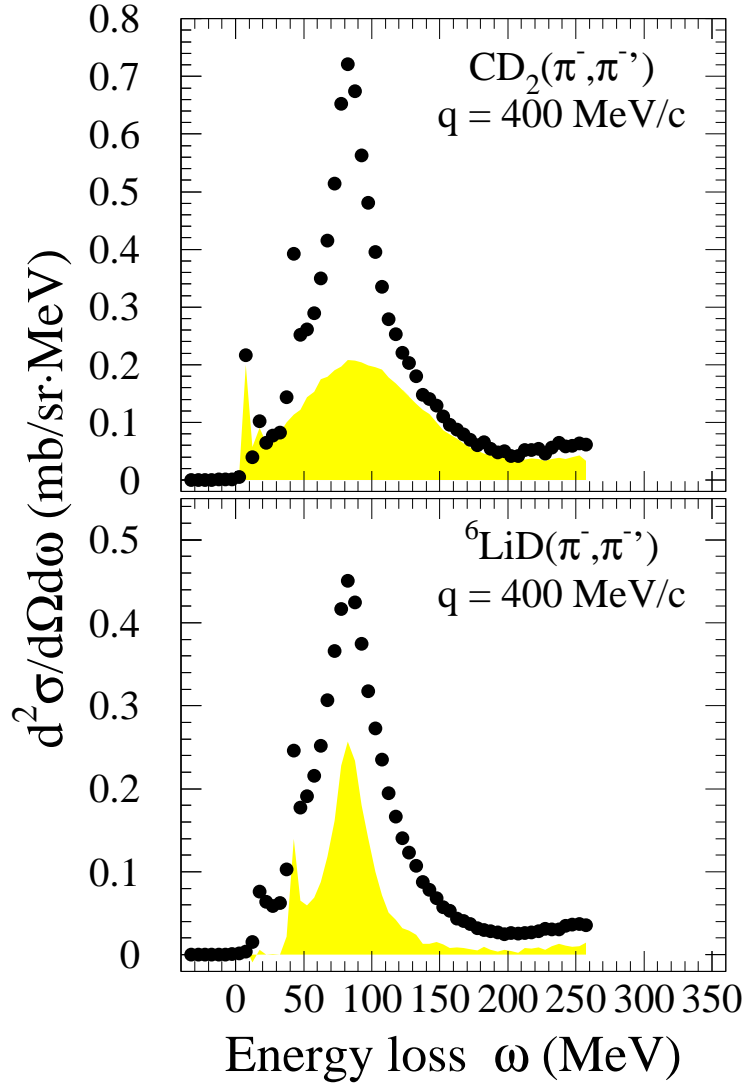


Figure 3.10: Doubly differential cross sections for the  $\text{CD}_2$  and  ${}^6\text{LiD}$  targets at  $q = 400 \text{ MeV}/c$ . Shaded histogram shows the C (D) spectrum to be subtracted from the  $\text{CD}_2$  ( ${}^6\text{LiD}$ ) spectrum.

# Chapter 4

## Results and Discussion

### 4.1 Overview

In this chapter, the experimental data are presented and discussed. First, in order to overview the results, cross section, width, and centroid of the quasielastic peaks are extracted and discussed based on a non-interacting Fermi gas model and an eikonal approximation. Secondly, the results are compared with the previous pion and kaon data in terms of experimental response function. Finally, the results are compared with a theoretical calculation.

### 4.2 Doubly differential cross sections

Figure 4.1 shows the doubly differential cross sections for D,  ${}^6\text{Li}$ , C, Ca, Zr, and  ${}^{208}\text{Pb}$  at  $q = 500 \text{ MeV}/c$ . Figure 4.2 shows the doubly differential cross sections for C at  $q = 350, 450, 550, \text{ and } 650 \text{ MeV}/c$ .

Bin width is  $25 \text{ MeV}/c$  for  $q$  and  $5 \text{ MeV}$  for  $\omega$ . Energy resolutions (as FWHM) for the  $\pi^-$ -p and  $\pi^-$ - ${}^{12}\text{C}$  elastic scattering are  $4.7 \text{ MeV}$  and  $2.3 \text{ MeV}$ , respectively. These are good enough for quasielastic scattering studies.

The spectra clearly show the characteristic shape of a quasielastic peak, centered at the energy loss corresponding to that of free  $\pi^-$ -nucleon elastic scattering and broadened due to the internal motion of individual nucleons inside a nucleus.



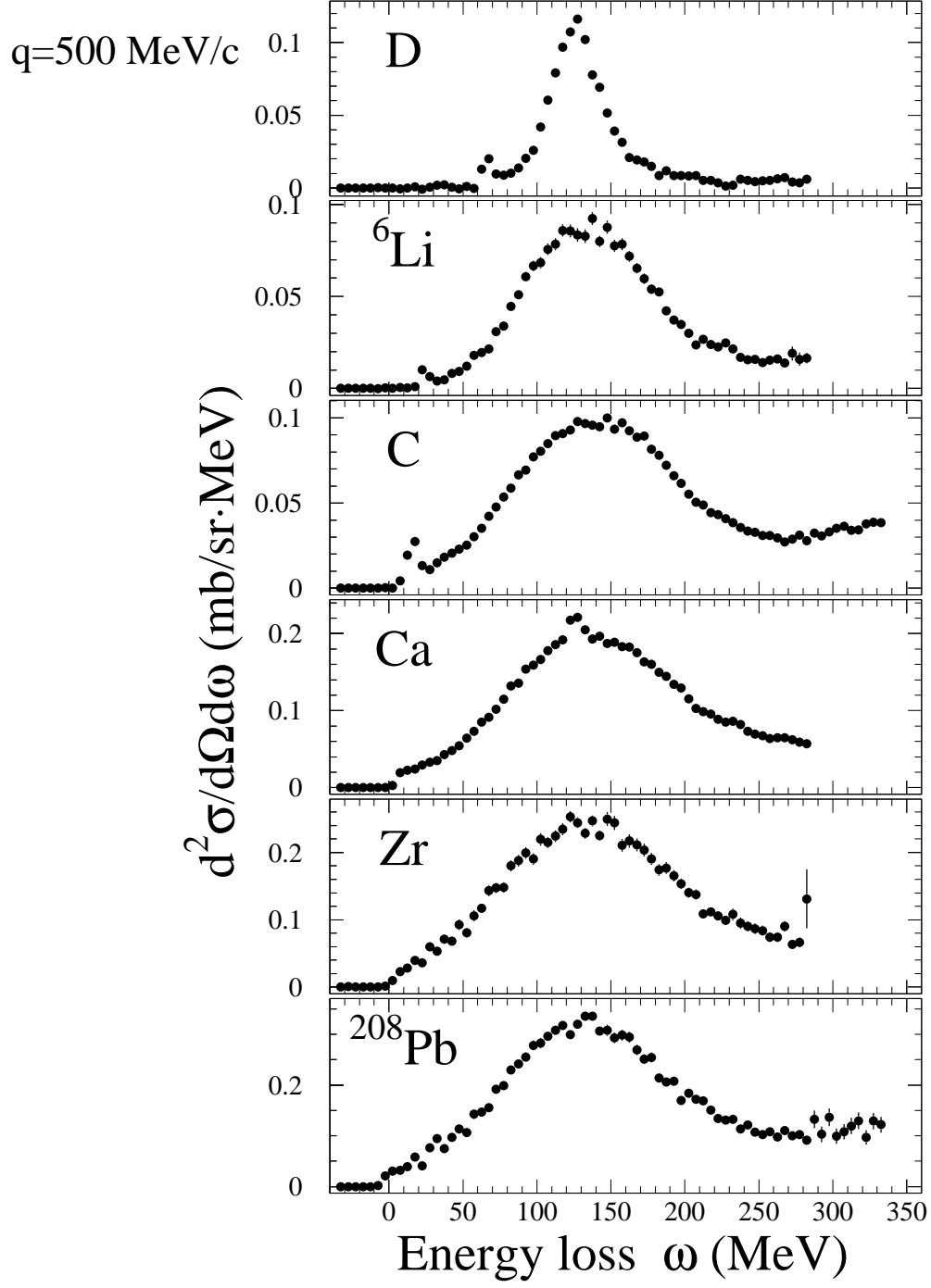


Figure 4.1: Doubly differential cross sections for D,  ${}^6\text{Li}$ , C, Ca, Zr, and  ${}^{208}\text{Pb}$  at  $q = 500 \text{ MeV}/c$ .

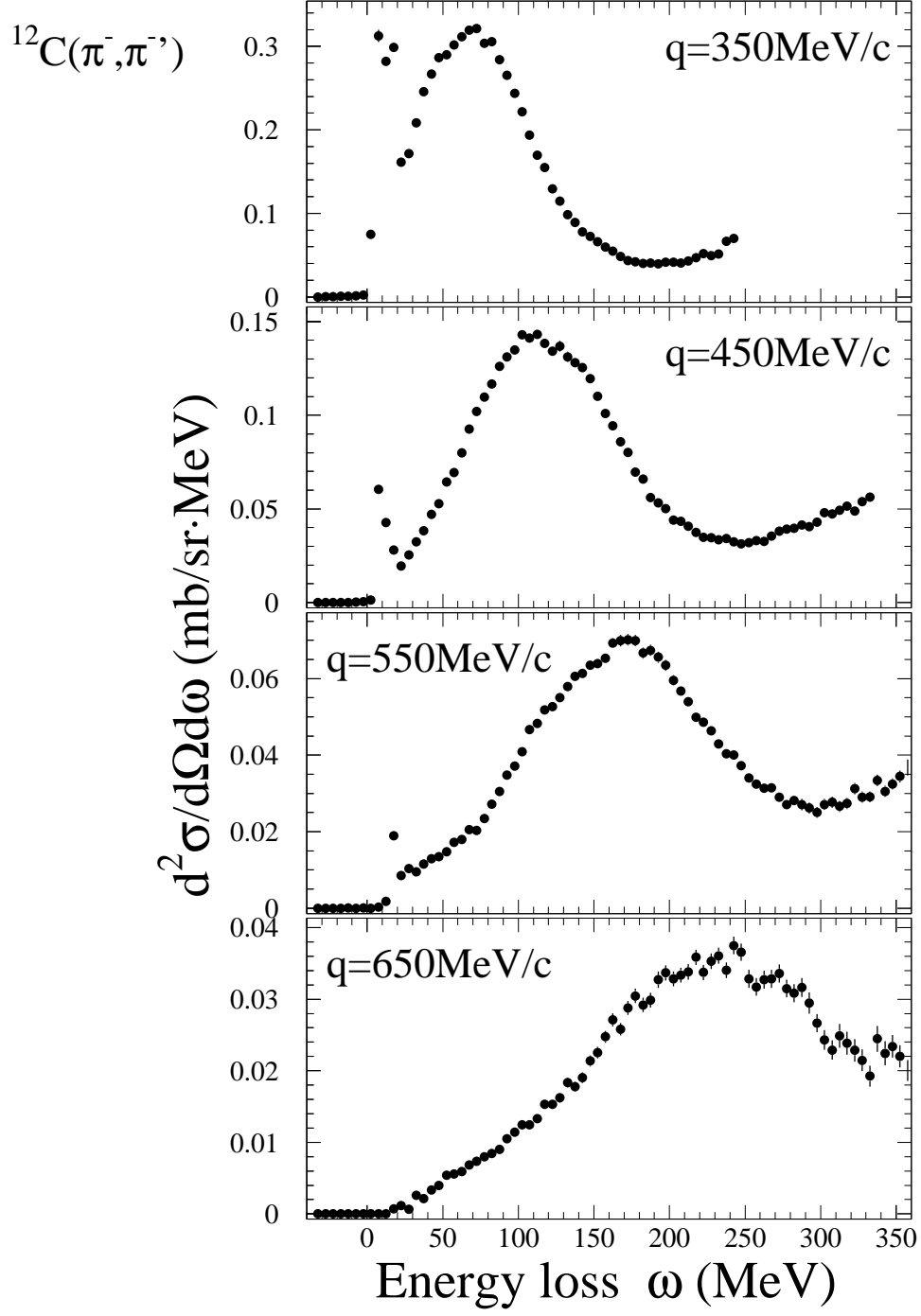


Figure 4.2: Doubly differential cross sections for C at  $q = 350, 450, 550$ , and  $650$   $\text{MeV}/c$ .

## 4.3 Fit to the quasielastic peak

### 4.3.1 Fitting procedure

Cross section, width, and centroid of the quasielastic peak were extracted by a fitting to the doubly differential cross sections. The spectra were fitted by a sum of three components: a quasielastic peak, a background, and additional Gaussian peak(s) for elastic and inelastic scattering. The following functions were used for the fitting, because they were simple and fairly well described the shape of the cross sections.

For the deuteron data, a shifted Lorentzian distribution was used to describe a quasielastic peak.

$$f_1(\omega) = \begin{cases} 0 & (\omega \leq \omega_{el}), \\ c_1 \left[ \frac{1}{(\omega - \omega_{el} - c_2)^2 + c_3} - \frac{1}{(\omega - \omega_{el} + c_2)^2 + c_3} \right] & (\omega > \omega_{el}), \end{cases} \quad (4.1)$$

$$\omega_{el} = \sqrt{q^2 + M_{tgt}^2} - M_{tgt} \quad (4.2)$$

where  $\omega_{el}$  is energy loss due to target recoil and  $M_{tgt}$  is a target mass. The original form (without  $\omega_{el}$ ) was introduced by Esbensen and Bertsch [23] to parametrize a free response of a semi-infinite slab model.

For the other targets, an asymmetric Gaussian with exponential cutoff factor  $C(\omega)$  was used to describe a quasielastic peak.

$$f_2(\omega) = \begin{cases} c_1 C(\omega) \exp\left(-\frac{1}{2} \left(\frac{\omega - c_2}{c_3}\right)^2\right) & (\omega \leq c_2), \\ c_1 C(\omega) \exp\left(-\frac{1}{2} \left(\frac{\omega - c_2}{c_4}\right)^2\right) & (\omega > c_2), \end{cases} \quad (4.3)$$

$$C(\omega) = \begin{cases} 0 & (\omega \leq \omega_{el}), \\ 1 - \exp\left(-\frac{\omega - \omega_{el}}{c_5}\right) & (\omega > \omega_{el}). \end{cases} \quad (4.4)$$

This formalism was introduced by Erell *et al.* [24]. In the original form, a Lorentzian was used to describe a quasielastic peak. The cutoff factor describes the suppression due to Pauli blocking.

For the calcium spectra, an additional Gaussian was included to describe a contribution from the hydrogen contamination. The width and centroid of the additional Gaussian were fixed to that of the  $\pi^-$ -p scattering data.

There supposed to be some contribution to the strength under the quasielastic peak from non-quasielastic processes, multiple scattering, two particle-two hole (2p-2h) excitations, and pion productions. In the present analysis, these contributions were subtracted as “background”, assuming the shape as a linear function of  $\omega$ ,

$$f_0(\omega) = \begin{cases} 0 & (\omega \leq \omega_{el}), \\ c_0(\omega - \omega_{el}) & (\omega > \omega_{el}). \end{cases} \quad (4.5)$$

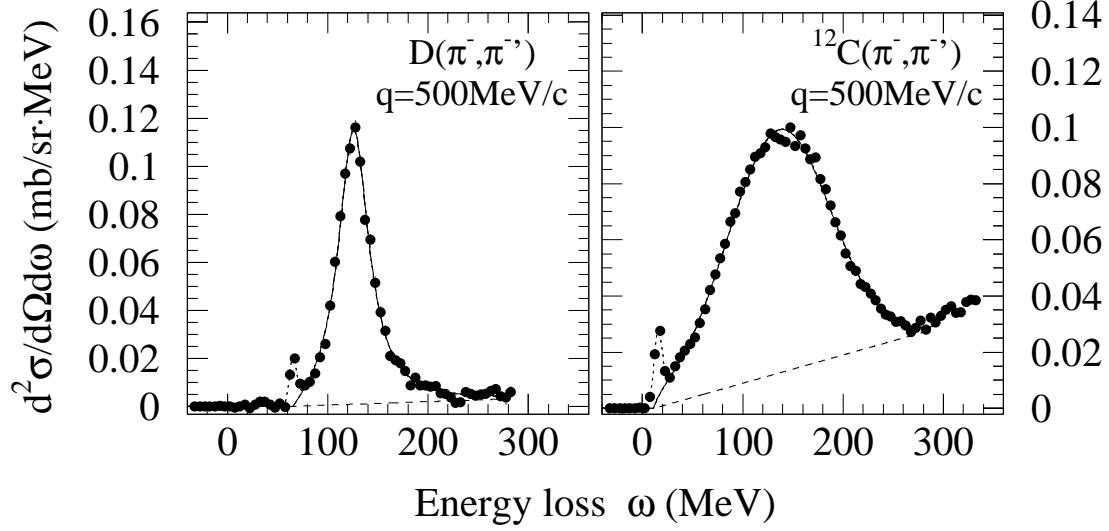


Figure 4.3: Samples of the fitting. The solid, dashed, and dotted lines show the fitted curve, background, and peak(s) for elastic and inelastic, respectively.

Using these functions, fitting to the doubly differential cross sections was performed. Figure 4.3 shows examples of the fitting. The solid, dashed, and dotted lines show the fitted curve, background, and peak(s) for elastic and inelastic, respectively. The spectra were well fitted by the present fitting functions. Then, cross section, width (in FWHM), and centroid of the quasielastic peaks were deduced.

The quasielastic cross sections for calcium were deduced from the extracted cross sections, which include contribution from the oxygen contaminant. The procedure is the following.

First, hydrogen impurity in the Ca target was determined to  $16 \pm 1\%$  of the number of calcium atoms from the fitting. Next, the ratio of the quasielastic cross sections between Ca and O was estimated by using Eq. (4.11). Finally, assuming the target composition of  $\text{Ca}(\text{OH})_{0.16}$ , the quasielastic cross sections for calcium were obtained as

$$\left(\frac{d\sigma}{d\Omega}\right)_{\text{QE}}^{(\text{Ca})} = \frac{A_{\text{eff}}^{\text{calc}}(\text{Ca})}{A_{\text{eff}}^{\text{calc}}(\text{Ca}) + 0.16 \cdot A_{\text{eff}}^{\text{calc}}(\text{O})} \cdot \left(\frac{d\sigma}{d\Omega}\right)_{\text{QE}}^{(\text{CaO}_{0.16})}. \quad (4.6)$$

### 4.3.2 Model uncertainty of the fitting

A model uncertainty of the fitting is mostly from evaluation of the background contribution. The present analysis assumed that the contribution is linear function of  $\omega$ , begins at energy loss of  $\omega_{el}$ . The reasons of this assumption are

the following. Pion production and 2p-2h excitation are two major processes to contribute to the background. Intranuclear cascade calculation [25] showed that the pion production contributed substantially to the inclusive  $(\pi, \pi')$  cross section. The contribution begins at about 175 MeV energy loss for 500 MeV pions. Alberico *et al.* showed that the 2p-2h excitation contributes significantly to the transverse  $(e, e')$  cross section [26]. The contribution begins close to zero energy loss. In addition,  $(\pi^-, \pi^0)$  data at large angle, where little quasielastic scattering is expected, were well described by a second-order polynomial [27]. Consequently, a linear background was assumed in the present analysis. Not quadratic but linear background was used because it was enough to fit the present spectra.

Model uncertainty was estimated from a fit to the spectra with another shape of background, a linear background begins at energy loss of 175 MeV. It modeled only delta production, while the background used in the analysis modeled both 2p-2h excitation and delta production. The difference in cross sections, widths, and centroids obtained from both fits were taken as model uncertainties, and referred as additional systematic errors in this thesis.

## 4.4 Quasielastic cross sections

Figure 4.4 shows the extracted quasielastic cross sections for the  $\pi^-$ -nucleus scattering as a function of momentum transfer. The solid lines show fitted results to a non-interacting Fermi-gas model with a parameter  $A_{\text{eff}}$ . The dotted lines show the same fits without a Pauli blocking factor. An expression for the fitting is obtained from Eq. (1.1), using a response function obtained from the non-interacting Fermi-gas model.

$$\frac{d\sigma}{d\Omega} = A_{\text{eff}} B(q, k_F) \left( \frac{d\sigma}{d\Omega} \right)_{\pi N}, \quad (4.7)$$

$$B(q, k_F) = \begin{cases} \frac{3q}{4k_F} - \frac{q^3}{16k_F^3} & (q < 2k_F), \\ 1 & (q \geq 2k_F), \end{cases} \quad (4.8)$$

where the factor  $A_{\text{eff}}$  is a parameter for the fitting and can be interpreted as the effective number of nucleons participating in the quasielastic scattering,  $B(q, k_F)$  is the Pauli blocking factor [28],  $k_F$  is the Fermi momentum of target nucleus, and  $\left( \frac{d\sigma}{d\Omega} \right)_{\pi N}$  is the elementary  $\pi$ - $N$  elastic scattering cross section, averaged over all nucleons in the nucleus as follows.

$$\left( \frac{d\sigma}{d\Omega} \right)_{\pi N} = \frac{Z(d\sigma/d\Omega)_{\pi^-p} + (A - Z)(d\sigma/d\Omega)_{\pi^+p}}{A}. \quad (4.9)$$

Since effects of Pauli blocking are small for the measured kinematical region,  $B = 0.85$  at the most for  $q = 350$  MeV/ $c$  on  $^{208}\text{Pb}$ ,  $k_F$  is fixed to the experimental value of the  $(e, e')$  data of Ref. [29]. Values of 169, 221, 249, 254, and 265 MeV/ $c$  were used for  $k_F$  in the fits to the  $^6\text{Li}$ , C, Ca, Zr, and  $^{208}\text{Pb}$  data, respectively. No

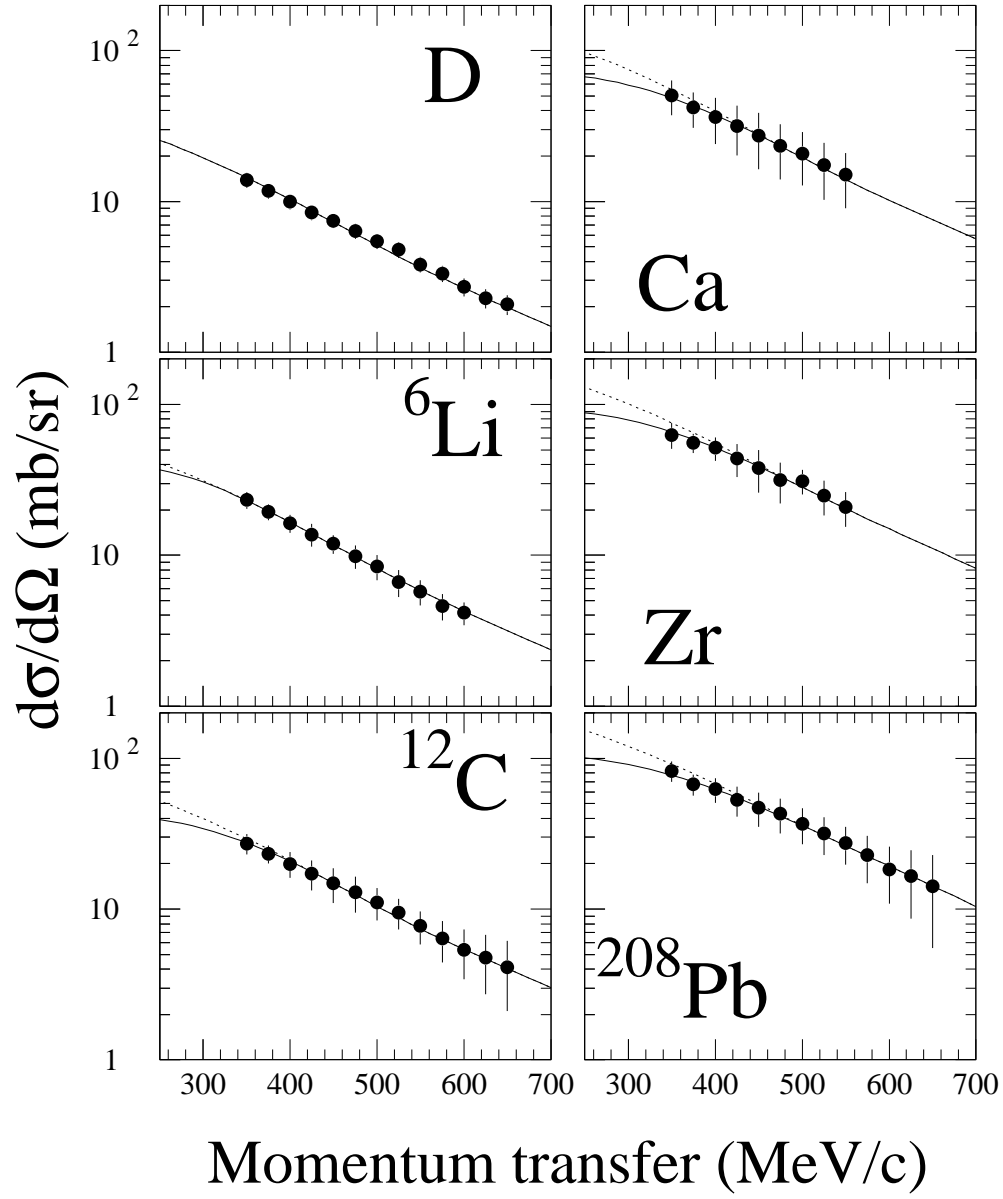


Figure 4.4: Quasielastic cross sections for D,  ${}^6\text{Li}$ , C, Ca, Zr, and  ${}^{208}\text{Pb}$  as a function of momentum transfer. The solid lines show fits to the cross sections. The dotted lines show the same fits without the Pauli blocking factor.

Table 4.1: Comparison of  $\alpha$  with other probes.  $\sigma_p$  ( $\sigma_n$ ) denotes the probe-proton (probe-neutron) total cross section.

	reaction	$\alpha$	$\sigma_p$ (mb)	$\sigma_n$ (mb)
$(\pi^-, \pi^{-'})$	950 MeV/ $c$ present	$0.42 \pm 0.01$	53.77	23.75
$(\pi^+, \pi^{+'})$	624 MeV/ $c$ [12]	$0.44 \pm 0.05$	19.2	33.0
$(\pi^-, \pi^{-'})$	624 MeV/ $c$ [12]	$0.56 \pm 0.03$	33.0	19.2
$(\pi^-, \pi^0)$	624 MeV/ $c$ [30]	$0.38 \pm 0.03$	33.0	19.2
$(K^+, K^{+'})$	705 MeV/ $c$ [15]	$0.61 \pm 0.05$	12.50	14.76
$(p, n)$	400 MeV [9]	0.50	26.82	33.31

blocking factor was used for the deuteron data. For the elementary  $\pi$ - $N$  elastic cross section the free  $\pi^-$ - $p$  and  $\pi^+$ - $p$  cross sections were used as obtained with SAID [22].

The present analysis well reproduces the experimental data with the single parameter  $A_{\text{eff}}$ . This agreement for the  $q$ -dependence of  $d\sigma/d\Omega$  confirms the cross section factorization of Eq.(1.1), that is, a factorization of distortion effect into  $A_{\text{eff}}$ .

Similar analyses were performed to the quasielastic  $(p, n)$  [8],  $(\pi, \pi')$  [12], and  $(\pi^\pm, \pi^0)$  [14] reactions. The effects of Pauli blocking were clearly seen in the forward-angle data of the  $(p, n)$  and  $(\pi^\pm, \pi^0)$  reactions, and the results were well reproduced with the Fermi-gas model.

## 4.5 Effective number of nucleons

The effective numbers of nucleons,  $A_{\text{eff}}$ , obtained from Eq. (4.7) are listed in Table 4.2. Atomic number,  $A$ , dependence of  $A_{\text{eff}}$  follows a power law,

$$A_{\text{eff}}^{\text{exp}} = N_0 A^\alpha. \quad (4.10)$$

The fit of  $A_{\text{eff}}$  to the power law as a function of  $A$  is shown in Figure 4.5. Best fit value for the exponent  $\alpha$  is  $0.42 \pm 0.01$ . The exponent  $\alpha$  less than one indicates a shadowing of nucleons in the nucleus by neighboring nucleons. For the electron scattering,  $\alpha$  is near unity because of the weakness of electron-nucleon interaction. Scattering from a black disk gives the lower limit of  $1/3$ . The present value of  $0.42$  indicates that pions are largely absorbed at the nuclear surface and thus scattered only from the surface region of a nucleus.

A comparison of  $\alpha$  with other probes is given in Table 4.1.  $\sigma_p$  ( $\sigma_n$ ) denotes the probe-proton (probe-neutron) total cross section. Among these hadronic probes, largest  $\alpha$  was obtained for the  $(K^+, K^{+'})$  reaction at 705 MeV/ $c$ , because  $K^+N$  total cross section for kaon laboratory momenta below 800 MeV/ $c$  is much weaker than that for  $NN$  and  $\pi N$ .

The value of  $A_{\text{eff}}$  can be estimated by using an eikonal approximation based on the Glauber theory [31].

$$A_{\text{eff}}^{\text{calc}} = \int d^2b T(b) e^{-\sigma_T T(b)}, \quad (4.11)$$

$$T(b) = \int_{-\infty}^{+\infty} dz \rho(\sqrt{b^2 + z^2}), \quad (4.12)$$

where  $\rho(r)$  is the proton density taken from the ground state charge distributions of Ref. [32] and references therein. The neutron density distribution is assumed to be same as that of proton.  $\sigma_T$  is the total  $\pi^-N$  cross section, averaged over all nucleons in the nucleus using the values for the  $\pi^-$ -p (53.77 mb) and  $\pi^-$ -n (23.75 mb) scattering. These values are obtained from SAID. The open circles in Figure 4.5 show the results of the calculation. The  $A$  dependence is well reproduced by the present calculation, though these are somewhat lower than the experimental ones. The lower values may be due to a change of the  $\pi^-N$  total cross section in the nuclear medium, which is somewhat reduced than the free values used in the calculation due to a Pauli-blocking effect. The lower total cross section increases the  $A_{\text{eff}}^{\text{calc}}$ .

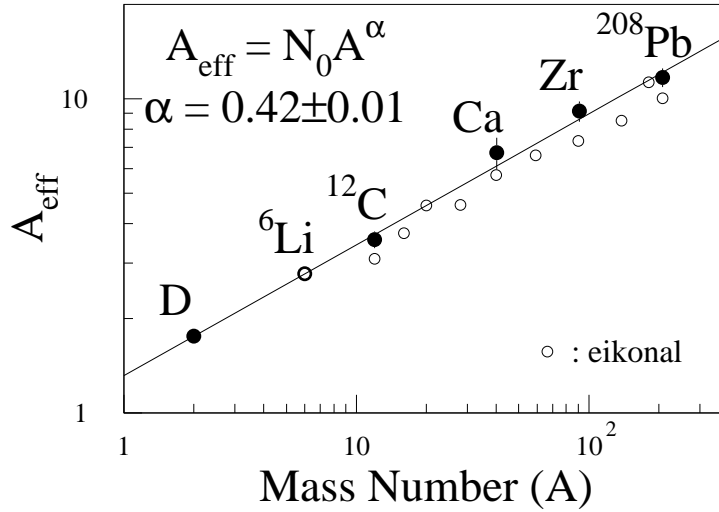


Figure 4.5: Fit of the effective number of nucleons to a power law. The open circles are the results of an eikonal calculation.

## 4.6 Fermi momenta

The response function for the non-interacting Fermi-gas model is parabolic in shape, and the width (in FWHM) of quasielastic peak  $\Gamma_{\text{FG}}$  can be related to the



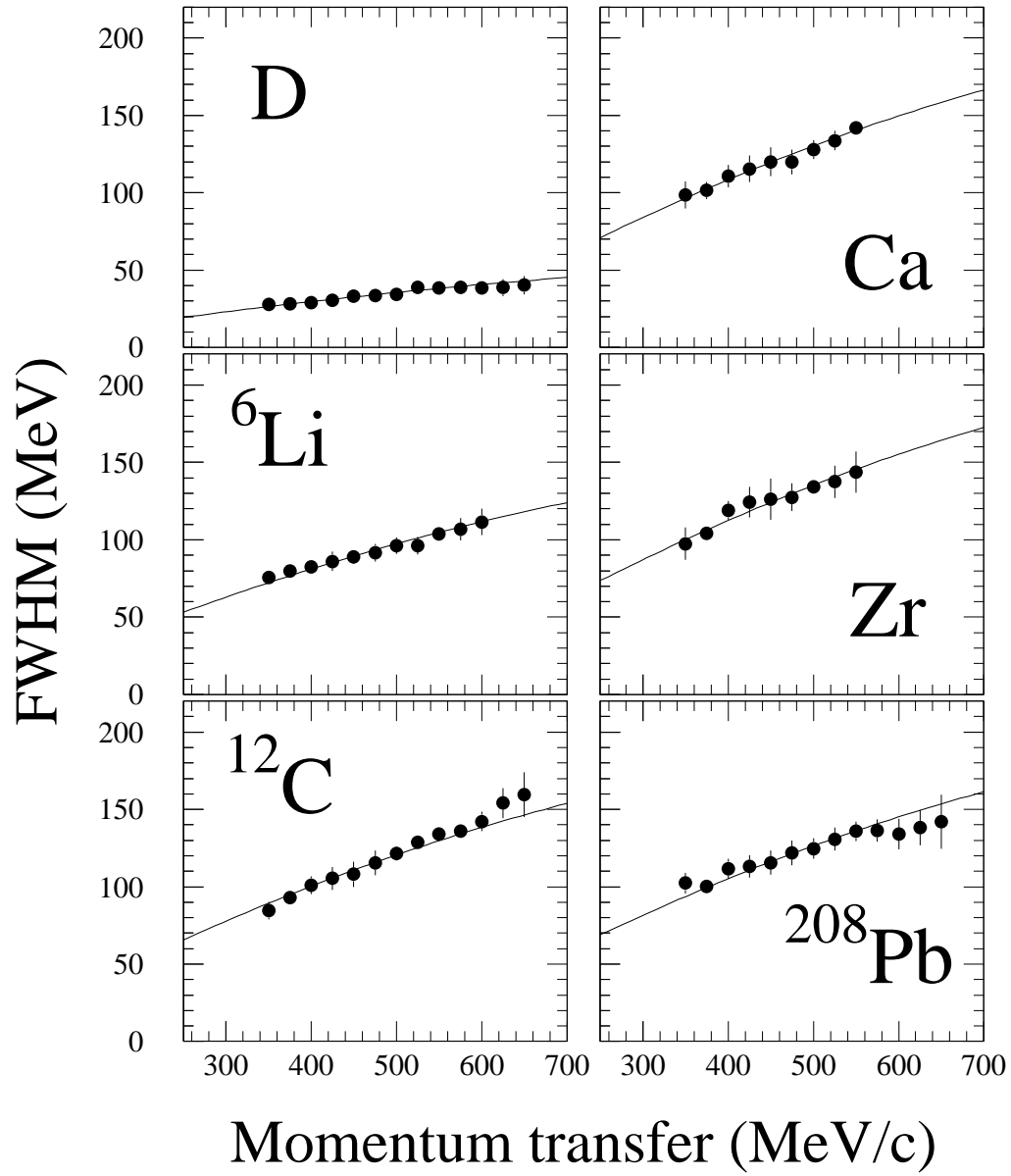


Figure 4.6: Extracted widths of quasielastic peak as a function of momentum transfer. The solid lines show a fit to a Fermi gas model using relativistic kinematics and a mass of free nucleon.

Table 4.2: Measured and calculated values of  $A_{\text{eff}}$ .

target	Z	A	experiment	eikonal
D	1	2.0	$1.76 \pm 0.06$	-
$^6\text{Li}$	3	6.0	$2.77 \pm 0.13$	2.77
C	6	12.0	$3.57 \pm 0.22$	3.09
Ca	20	40.1	$6.75 \pm 0.77$	5.73
Zr	40	91.2	$9.15 \pm 0.68$	7.36
$^{208}\text{Pb}$	82	208.0	$11.70 \pm 0.80$	10.04

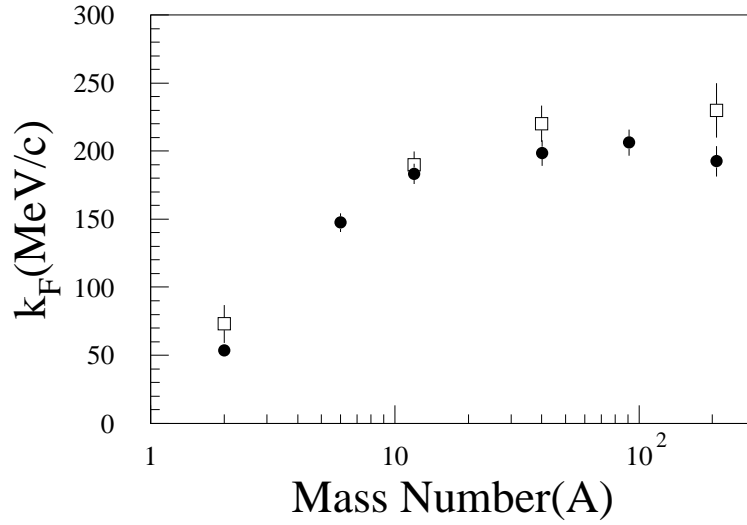


Figure 4.7: Fermi momenta extracted from measured widths of the quasielastic peaks are compared. The filled circles are the present results and the open squares are the values from the  $(K^+, K^{+'})$  reaction.

Table 4.3: Dominant couplings of reactions and observed peak shifts

reaction	dominant couplings	peak shift (MeV)
$(e, e')$	$S=0, T=0+1$ and $S=1_T, T=1$	+10~+30
$(p, p')$	$S=1, T=1$ and $S=0, T=0$	+5
$(p, n)$	$S=1, T=1$	+26
$(^3\text{He}, t)$	$S=1, T=1$	+16 ( $q = 280 \text{ MeV}/c$ )
		-17 ( $q = 480 \text{ MeV}/c$ )
$(\pi, \pi^0)$	$S=0, T=1$	+20 (at low $q$ )
		$\sim 0$ ( $q > 500 \text{ MeV}/c$ )
$(\pi, \pi')$	$S=0, T=0$	$\sim 0$ (previous data)

Fermi momentum and effective mass of the struck nucleon  $M^*$  by the relationship

$$\Gamma_{\text{FG}} = \frac{1}{\sqrt{2}} \left( \sqrt{M^{*2} + (q + k_F)^2} - \sqrt{M^{*2} + (q - k_F)^2} \right), \quad (4.13)$$

where relativistic kinematics for  $q$  is used. Figure 4.6 shows the widths of the quasielastic peak as a function of momentum transfer, obtained by fitting to Eq. (4.13). The solid lines show the results fitted by a mass of free nucleon for  $M^*$ . Figure 4.7 shows the obtained Fermi momenta as a function of  $A$ . The filled circles are the present results and the open squares are the values from the  $(K^+, K^{+'})$  reaction [15]. There is a sharp rise in  $k_F$  with mass number increasing from D to C and moderate increase from Ca to  $^{208}\text{Pb}$ , as nuclear density in heavier nuclei becomes saturated.

The kaon data give somewhat larger  $k_F$  than the present data. This may be due to a difference of a nuclear mean free path; pions probe a lower density than kaons do.

## 4.7 Peak shifts

Figure 4.8 shows shift of quasielastic peak energy for each nucleus. Here the peak shift is defined as the difference in energy loss between the quasielastic and hydrogen elastic peak. The positive (negative) value means the peak shifts toward higher (lower) energy loss relative to free kinematics, and is often called a hardening (softening) of the response. The present result shows a hardening with an increase in  $q$ , especially on  $^6\text{Li}$  and  $^{12}\text{C}$ .

Figure 4.9 shows a comparison of the quasielastic peak shifts on carbon observed in: (a)  $(e, e')$  [33] (+); (b)  $(p, p')$  [34] at 400 MeV (open triangles),  $(p, n)$  [9] at 300 MeV (solid triangles), and  $(^3\text{He}, t)$  [11] (asterisks); (c)  $(\pi^+, \pi^{+'})$  (solid stars) and  $(\pi^-, \pi^{-'})$  (open stars) at 624 MeV/c [12], and the present data at 950 MeV/c (solid circles); (d)  $(\pi^+, \pi^0)$  (open squares) and  $(\pi^-, \pi^0)$  (solid squares) at

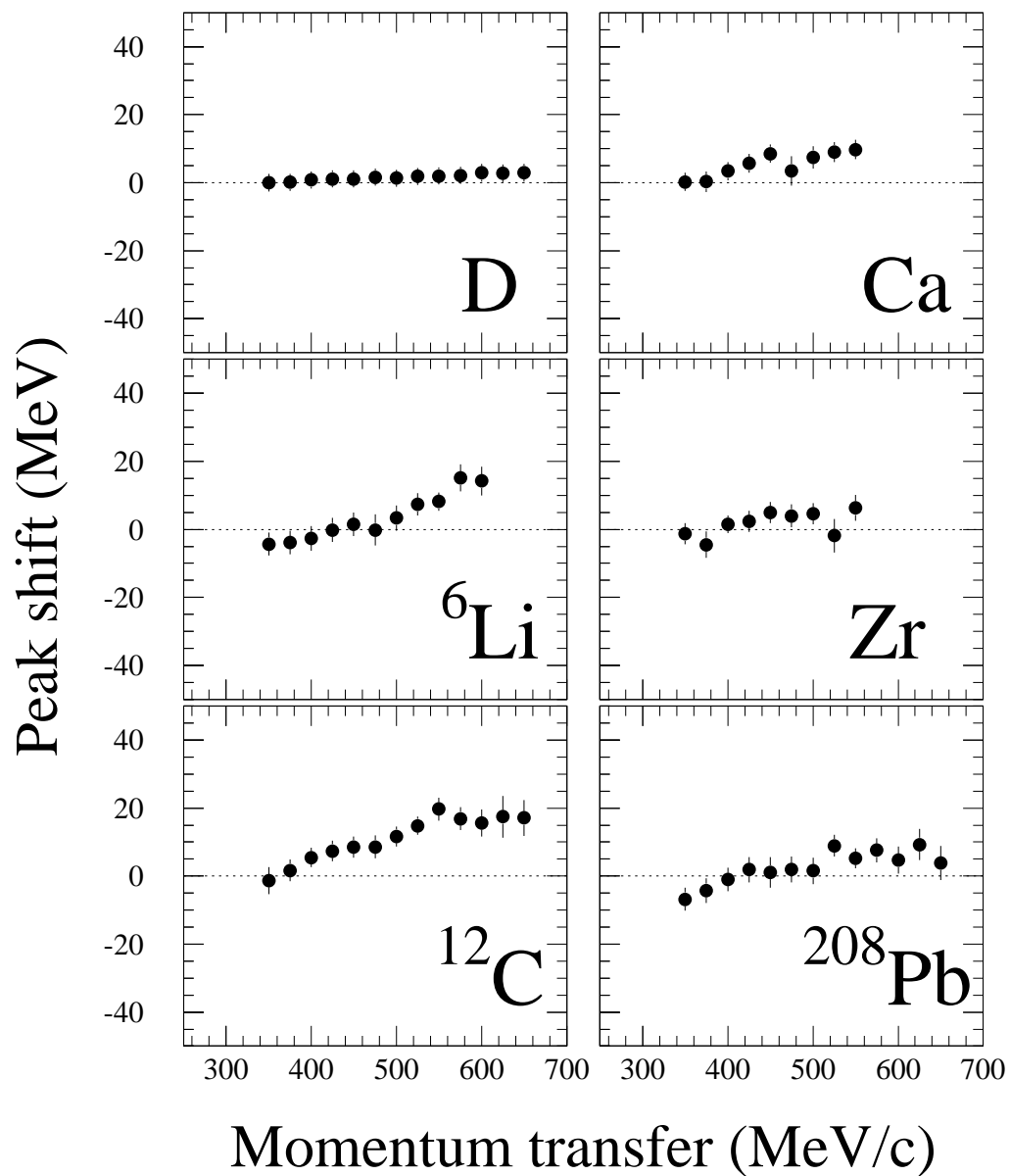


Figure 4.8: Quasielastic peak shifts relative to scattering from hydrogen for D,  $^6\text{Li}$ , C, Ca, Zr, and  $^{208}\text{Pb}$ .

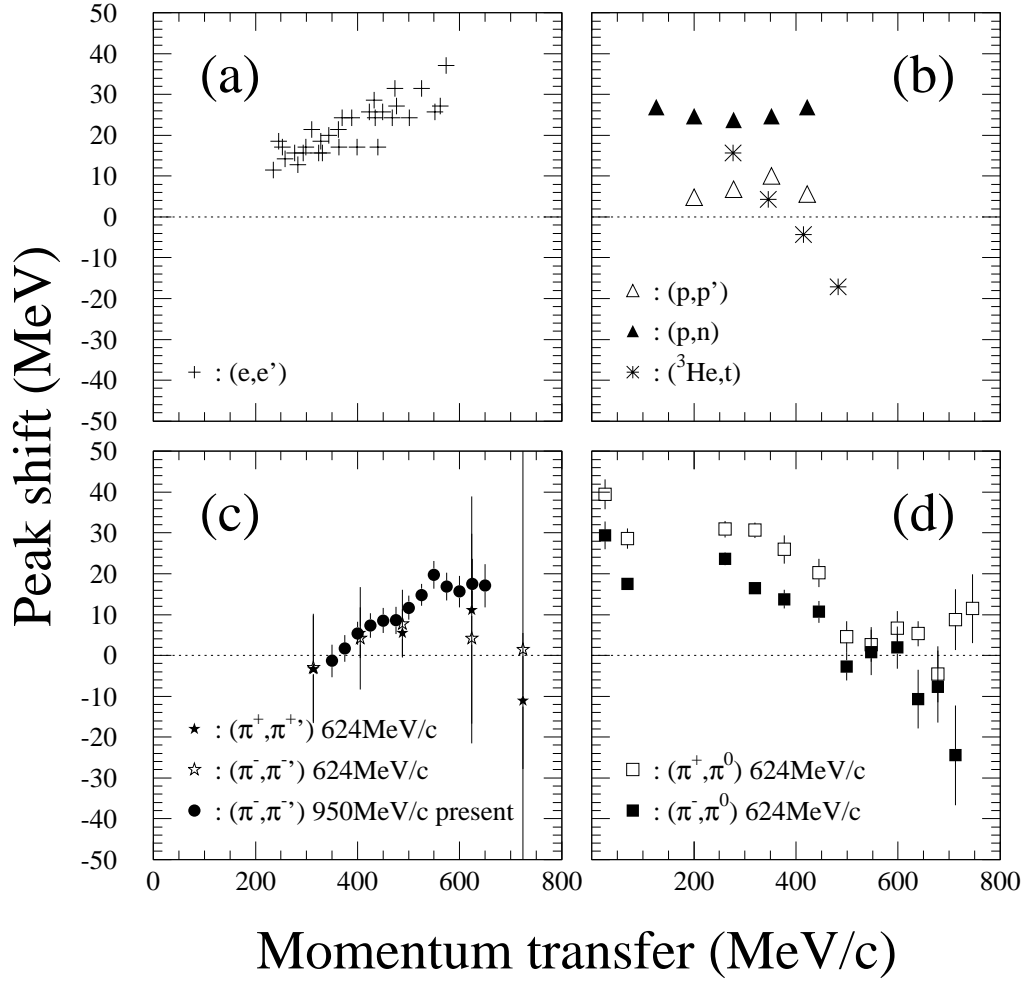


Figure 4.9: A comparison of the quasielastic peak shifts on carbon observed in (a)  $(e, e')$  (+); (b)  $(p, p')$  (open triangles),  $(p, n)$  (solid triangles), and  $(^3\text{He}, t)$  (asterisks); (c)  $(\pi^+, \pi^+)$  (solid stars) and  $(\pi^-, \pi^-)$  at 624 MeV/c (open stars) and present data at 950 MeV/c (solid circles); (d)  $(\pi^+, \pi^0)$  (open squares) and  $(\pi^-, \pi^0)$  (solid squares).

624 MeV/c [14]. These are often explained as an average separation energy of nucleon or in terms of effective mass of nucleon inside a nucleus. These can also be explained as due to nuclear correlations. The observed responses reflect the associated particle-hole interaction. In Table 4.3 dominant couplings for each reaction are summarized together with peak shifts.

Calculation of Alberico *et al.* predicted a hardening for spin-transverse response and a softening for spin-longitudinal response [16]. The former can account the hardening of the  $(e, e')$  and  $(p, n)$  reactions. The difference of peak shift between the  $(p, n)$  and  $(p, p')$  reactions, however, was unexplained even if scalar-isoscalar contribution is considered [35].

It is suggested that the contribution of the spin-longitudinal response accounts the  $q$ -dependent shift of the  $(^3\text{He}, t)$  reaction [36].

Ouyang *et al.* showed that isovector response of carbon is hardened both non-spin-flip and spin-flip channels due to repulsive particle-hole interactions, and explained the  $(\pi^\pm, \pi^0)$  data fairly well.

In previous  $(\pi, \pi')$  experiment at 624 MeV/c [12] no significant peak shift was observed for the momentum transfer up to about 600 MeV/c. However, due to large uncertainty of the previous data, the present data can be consistent with previous one. In contrast, 624 MeV/c pion single charge exchange (SCX) data showed systematics quite different from the present result, that is, hardening at low  $q$  and softening at high  $q$ . This can be interpreted as due to a momentum-transfer dependence from different channels of particle-hole interaction, because such SCX reaction probes the isovector channel of the nuclear response.

A discussion for the present data in regard to effective particle-hole interaction will be given in section 4.9 with result of a theoretical calculation.

## 4.8 Comparison with other data

In this section the present data are compared with the kaon data at 705 MeV/c and previous pion data at 624 MeV/c. Kaon quasielastic scattering also probes mostly the scalar-isoscalar channel of the response, and is expected to be more sensitive to the nuclear interior than pion quasielastic, because relative weakness of the  $K^+N$  interaction. Thus we may see density dependent effects in this comparison. A comparison with previous pion data possibly indicate a difference of a contribution of the scalar-isoscalar channel.

In the impulse approximation, quasielastic cross section is factorized as given in Eq. (1.1) and a response function depends only upon the internal structure of the target nucleus. Thus, we can obtain experimental nuclear response by dividing the doubly differential cross section by the corresponding elementary cross section and some normalization factor.

$$R(q, \omega) = \frac{d^2\sigma}{d\Omega d\omega} \left[ N_{\text{eff}} \left( \frac{d\sigma}{d\Omega} \right)_{\text{elem}} \right]^{-1}. \quad (4.14)$$

Here, the elementary cross section in free space  $(d\sigma/d\Omega)_{\text{elem}}$  is calculated by SAID, and  $N_{\text{eff}}$  is calculated with Eq. (4.11).

Figure 4.10 shows the experimental response functions for  $^{12}\text{C}$  at a momentum transfer of approximately 475 MeV/ $c$  for (a) the  $(\pi^-, \pi^{-'})$  reaction at 950 MeV/ $c$  present work and (b) the  $(K, K')$  reaction at 705 MeV/ $c$  [15]. Figure 4.11 shows a ratio of the response functions  $R_\pi/R_K$ . The obtained responses for  $(\pi^-, \pi^{-'})$  and  $(K, K')$  are quite similar, and we see no pronounced difference. The increase in ratio at high  $\omega$  will be due to contribution from delta excitation.

Figure 4.12 shows the experimental response functions for  $^{12}\text{C}$  at a momentum transfer of approximately 400 MeV/ $c$  for  $(\pi^-, \pi^{-'})$  reaction at (a) 950 MeV/ $c$  present work and (b) 624 MeV/ $c$  [12]. Figure 4.13 shows a ratio of the response functions (a)/(b). The enhancement of the ratio at the low energy loss side of the peak can be due to an increased contribution of the scalar-isoscalar response, because the scalar-isoscalar response is enhanced at the low energy loss side of the peak as shown in next section.

It may be noted, however, that this comparison is quite naive, because contribution from non-quasielastic processes is included in these plots, and momentum transfer is not constant for the kaon and previous pion plots, varies by about 5% over the width of the quasielastic peak. Moreover, these responses are from simple factorization of Eq. (4.14). Further sophisticated method is needed for precise derivation of the experimental responses.

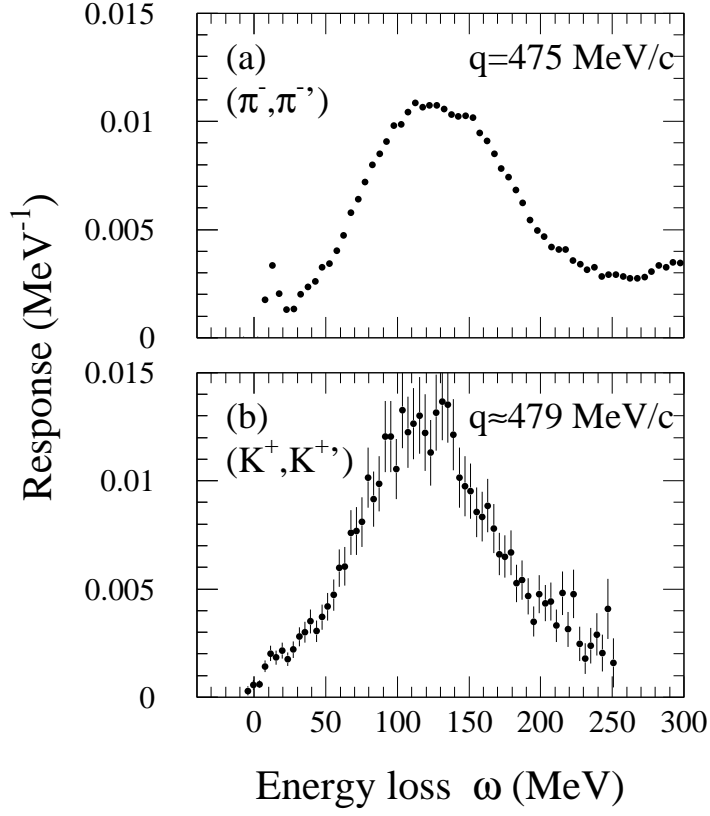


Figure 4.10: Response functions for  $^{12}\text{C}$  at a momentum transfer of approximately  $475 \text{ MeV}/c$  for (a) the  $(\pi^-, \pi'^-)$  reaction at  $950 \text{ MeV}/c$  present work and (b)  $(K, K')$  reaction at  $705 \text{ MeV}/c$ .

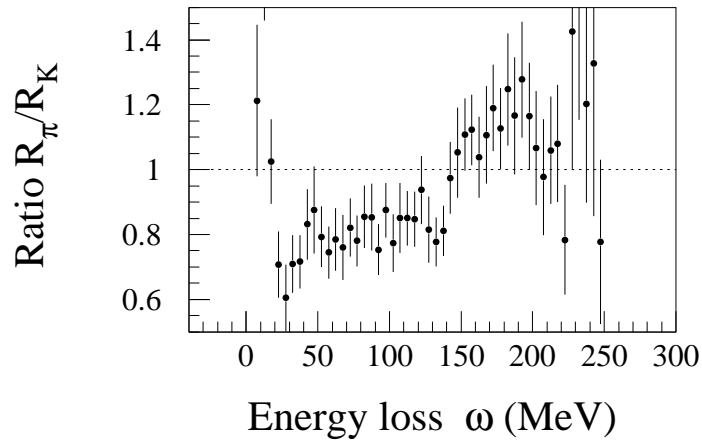


Figure 4.11: Ratio of response functions  $R_\pi/R_K$ .



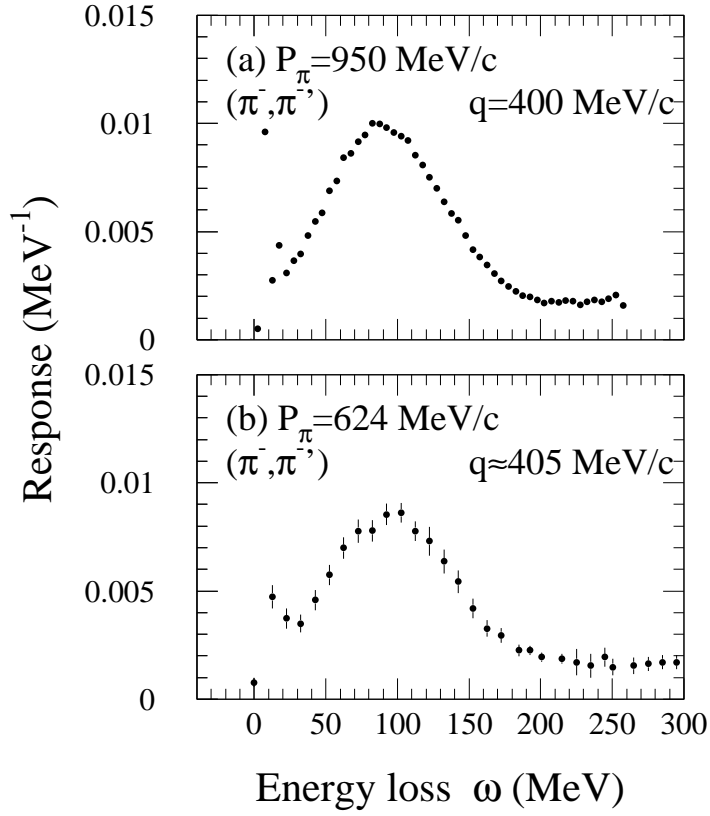


Figure 4.12: Response functions for  $^{12}\text{C}$  at a momentum transfer of approximately 400 MeV/c for  $(\pi^-, \pi'^-)$  reaction at (a) 950 MeV/c present work and (b) 624 MeV/c previous work.

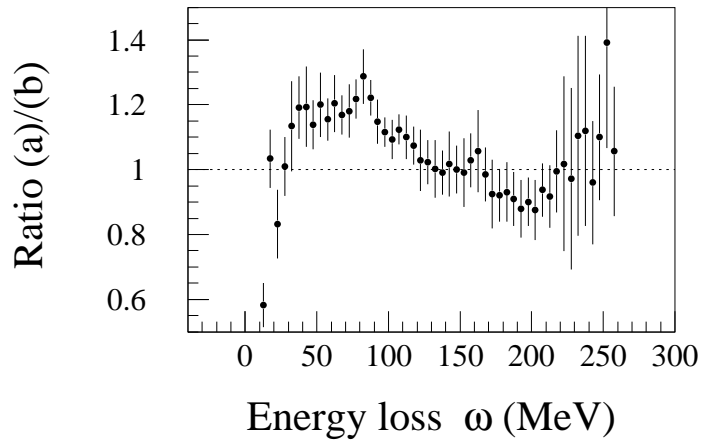


Figure 4.13: Ratio of response functions (a)/(b).

## 4.9 Comparison with theoretical calculation

Several sophisticated theoretical models have been developed attempting to analyze a quasielastic observables with hadronic probes; semi-infinite slab model [28][23], relativistic PWIA [37], distorted-wave impulse approximation (DWIA) using continuum random phase approximation (RPA) with the orthogonality condition [36], and continuum RPA using a density-dependent particle-hole interaction [35][18].

Among these, the present result is compared with a preliminary calculation performed by A. De Pace [38]. The calculation is based on a finite nucleus continuum RPA framework with consistent treatment of reaction mechanism following the Glauber theory, using a density-dependent particle-hole interaction. For the effective particle-hole interaction, a G-matrix in Ref. [39] used the strength of scalar-isoscalar channel renormalized by 50%. The present calculation are by the same framework as described in Ref. [18]. The calculation well reproduced the  $(K, K')$  quasielastic data.

Figure 4.14 shows a comparison between a free (dotted line) and RPA (solid line) response in the scalar-isoscalar channel for  $\pi^-$ - $^{12}\text{C}$  quasielastic scattering. At low momentum transfer, where nuclear correlations are important, the attractive interaction of the scalar-isoscalar channel is responsible for the significant softening relative to the free response. At high momentum transfer, there observed little difference between the RPA and free calculation, since the interaction becomes less important.

Figure 4.15 shows  $\pi^-$ - $^{12}\text{C}$  quasielastic cross sections compared with the RPA calculations. The open circles show the quasielastic portion of the experimental data; the background determined by the fitting described in section 4.3 is subtracted from the experimental data. The dashed lines show the response only with the scalar-isoscalar channel, the solid lines show the total (sum of all channels) response, and the dotted lines show contribution from non-scalar-isoscalar responses. At low momentum transfer, it is clearly seen that the scalar-isoscalar channel dominates the total response. Moreover, at the low energy loss side of the quasielastic peak, the present RPA calculation overestimates the experimental cross section. This will imply that the interaction used in the calculation is too attractive in the scalar-isoscalar channel.

The RPA responses show a hardening with an increase in  $q$ . At  $q < 550 \text{ MeV}/c$ , total response is dominated by the scalar-isoscalar channel and the peak shift is responsible for a  $q$  dependence of the scalar-isoscalar response. At  $q > 550 \text{ MeV}/c$ , the hardening of the total response is due to an increasing contribution from non-scalar-isoscalar responses. The  $q$  dependence of the observed peak shift on  $^{12}\text{C}$  shown in Figure 4.8 is qualitatively reproduced by the RPA calculation. Thus, the observed peak shift will be due to the change of nuclear responses, reflecting the  $q$  dependence of the particle-hole interactions.

$^{12}\text{C}$

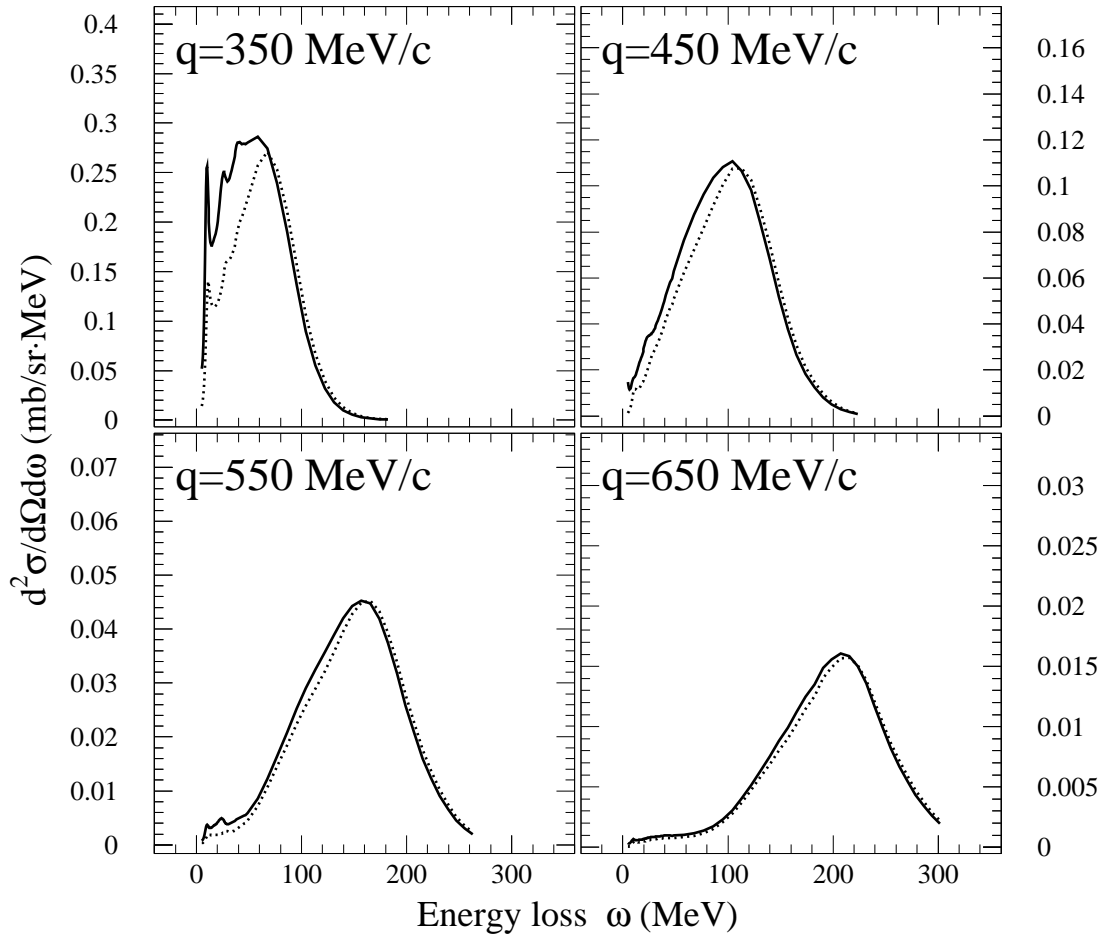


Figure 4.14: A comparison between a free (dotted line) and RPA (solid line) response in the scalar-isoscalar channel for  $\pi^-$ - $^{12}\text{C}$  quasielastic scattering.

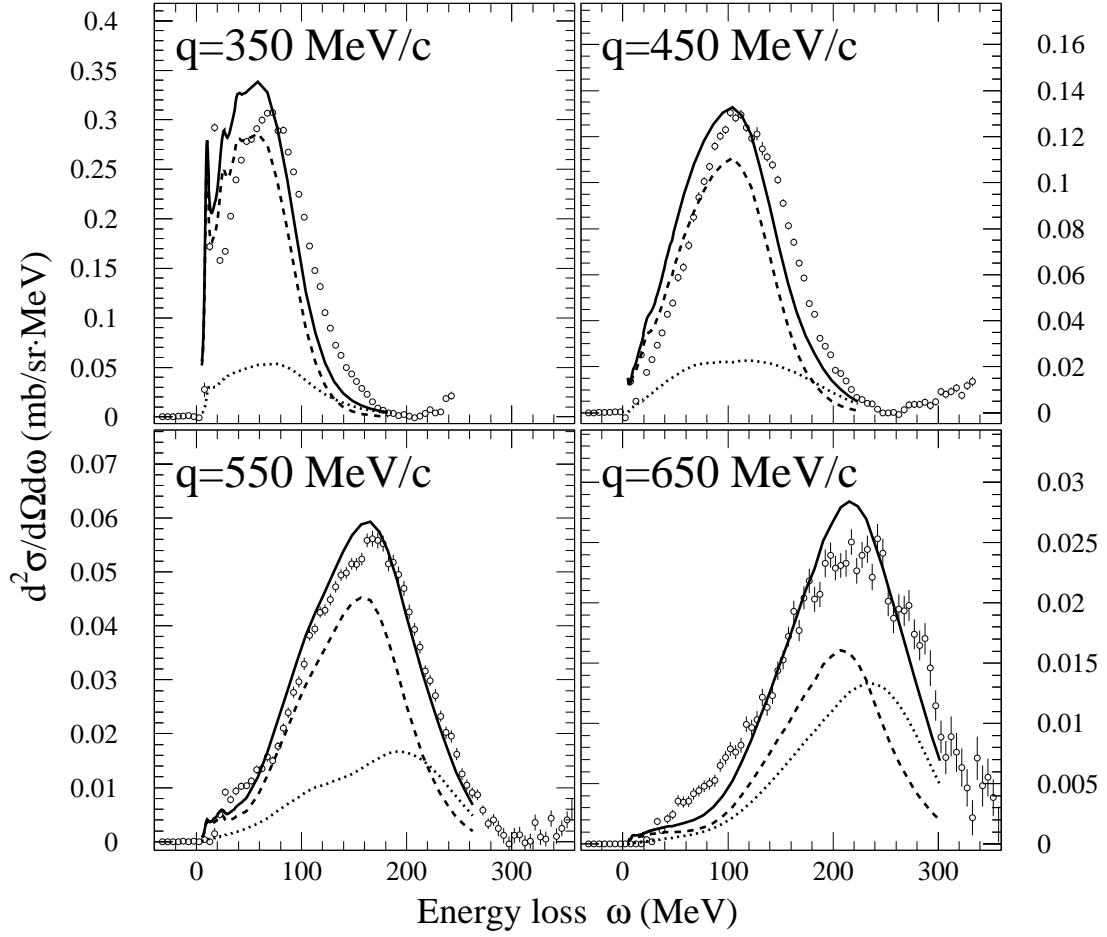
$^{12}\text{C}$ 

Figure 4.15:  $\pi^-$ - $^{12}\text{C}$  quasielastic cross sections compared with the RPA calculation. The open circles show the quasielastic portion of the experimental data. The dashed lines show the response only with the scalar-isoscalar channel, the solid lines show the total (sum of all channels) response, and the dotted lines show contributions from non-scalar-isoscalar responses.

# Chapter 5

## Summary and Conclusions

Quasielastic scattering of negatively charged pions from nuclei of D,  ${}^6\text{Li}$ , C, Ca, Zr, and  ${}^{208}\text{Pb}$  at an incident momentum of 950 MeV/ $c$  is studied for a momentum transfer range from 350 to 650 MeV/ $c$ .

The doubly differential cross sections show a broad peak corresponding to quasielastic single nucleon knockout.

The effective number of nucleons and Fermi momentum are extracted and discussed based on the non-interacting Fermi-gas model and the eikonal approximation. The results can be understood as that the quasielastic pion scattering in this momentum region takes place at the surface of a target nucleus.

The  ${}^{12}\text{C}$  data are compared with other data and an RPA calculation. The comparison shows that the measured response is dominated by the scalar-isoscalar response over a range of  $q$  from 350 to 550 MeV/ $c$ . At low  $q$  the RPA response overestimates the measured response at the low energy loss side of the quasielastic peak. This suggests that the interaction used in the RPA calculation is too attractive in the scalar-isoscalar channel. The hardening of the measured response with greater  $q$  is interpreted as due to the  $q$  dependence of the scalar-isoscalar response at  $q < 550$  MeV/ $c$ . The observed hardening at high  $q$  will imply the increased contribution from non-scalar-isoscalar responses.

In conclusion, this study has revealed the momentum transfer dependence of the scalar-isoscalar response over a wide range of momentum transfer, from 350 to 550 MeV/ $c$ , through the pion quasielastic scattering.

# Acknowledgments

I wish to express my thanks to my advisor Professor Takemi Nakagawa for his continuous guidance, support, advice, and encouragement in the course of the work.

I am much indebted to Professor Jerry Peterson, the spokesperson of the KEK-PS E352 experiment. I would like to thank him for his valuable advice and encouragement.

I owe countless debts to Professor Osamu Hashimoto, the chief examiner of this thesis. I would like to thank him for introducing me to this field of work and his continuous guidance, support, advice, and encouragement in the course of the work.

I am deeply indebted to all the members of this experiment.

I would like to acknowledge Professor Arturo De Pace for sending us the theoretical result.

I would like to thank the staff of the KEK-PS for their support in running this experiment.

I am indebted to all the members of the experimental nuclear physics group at Tohoku University.

Last but not least, I would like to express my gratitude to my parents, Akira and Kiyomi Fujii, my brother Takanori, and my grandparents, Tyuuji and Sumie Fujii, and Matsue Sakamoto for their continuous support and encouragement.

# Appendix A

## Acceptance Study of the SKS

The KEK-PS E352 is the first experiment that utilizes full acceptance of the SKS. Thus we carried out an extensive study of the acceptance of the SKS by taking  $\pi^-p$  elastic scattering data. We devoted 30% of the total beam for the study as listed in Table 2.8.

### A.1 Effective solid angle of the SKS

An effective solid angle of the SKS,  $\Delta\Omega_{\text{eff}}$ , was calculated with a Monte-Carlo simulation code. We need five parameters to fully specify the acceptance of the SKS  $\mathcal{A}$  (apart from particle decay, absorption etc.). For instance, horizontal and vertical position and their derivatives ( $x_s, y_s, u_s, v_s$ ) and momentum  $p_s$  of a particle on a virtual target plane.

$$\mathcal{A}(x_s, y_s, u_s, v_s, p_s) = \begin{cases} 1, & \text{if the particle is in the SKS acceptance,} \\ 0, & \text{otherwise.} \end{cases} \quad (\text{A.1})$$

Since  $\Delta\Omega_{\text{eff}}$  is a function of a scattering angle  $\theta$ , we also need a beam profile to calculate it. Here we define a beam profile distribution function  $\mathcal{B}(x_b, y_b, u_b, v_b)$ , where  $(x_b, y_b, u_b, v_b)$  is horizontal and vertical position and their derivatives of a beam particle on the virtual target plane.

In the present analysis, the beam profile dependence on the  $\Delta\Omega_{\text{eff}}$  was averaged out by using experimental beam profile. Then we get  $\Delta\Omega_{\text{eff}}$  as a function of  $\theta$  and  $p$  as follows:

$$\begin{aligned}
\Delta\Omega_{\text{eff}}(\theta, p) &= \left( 2\pi \int_{\theta-\frac{1}{2}\Delta\theta}^{\theta+\frac{1}{2}\Delta\theta} \sin\theta d\theta \right) \\
&\times \int dx \int dy \iiint_{\theta-\frac{1}{2}\Delta\theta \leq \Theta < \theta+\frac{1}{2}\Delta\theta} du_s dv_s du_b dv_b \\
&\quad \mathcal{A}(x, y, u_s, v_s, p) \mathcal{B}(x, y, u_b, v_b) , \tag{A.2} \\
\Theta &= \arctan \sqrt{\tan^2 \theta_u + \tan^2 \theta_v}, \tag{A.3} \\
\theta_u &= \arctan u_s - \arctan u_b + \theta_{\text{SKS}}, \tag{A.4} \\
\theta_v &= \arctan v_s - \arctan v_b. \tag{A.5}
\end{aligned}$$

where  $\theta_{\text{SKS}}$  is a rotation angle of the SKS and  $\Delta\theta$  is a bin width. Eq. (A.2) was evaluated with the Monte-Carlo simulation code.

### A.1.1 Monte-Carlo simulation code

The Runge-Kutta routine used in the offline analysis program is also used in the Monte-Carlo simulation code, with adding some software cuts in order to simulate the actual experimental condition of:

- A scattered particle passes through the effective area of each detector
- A scattered particle does not hit any materials such as pole face

Applied cuts for each detector are listed in Table A.1. In addition, a cut of  $\theta > 17^\circ$  and a cut shown in Figure A.1 as the shadowed area were applied. The former is the same software cut as applied in the offline data analysis; this rejects events from VETO counter. The latter is responsible for a decreasing of  $\Delta\Omega_{\text{eff}}$  at low momentum and large  $u_s$  region. The absolute magnitude and global structure of  $\Delta\Omega_{\text{eff}}$  are determined by the vertical cut in the pole gap.

Some of them are differ for each momentum setup, but these differences are not essential except for the SDC2 cut. The SDC2 cut for the 210A mode is essential to reproduce the  $\pi^-$ -p cross section. This cut is responsible for vertical acceptance of the SKS. I can not find, however, the physical meaning of this cut.

A pion survival factor was included in the present Monte-Carlo simulation code. The factor is calculated from flight path and momentum of the particle. Typical survival factor is 90%.

Beam events were generated in accordance with the experimental beam profile, including  $x$ - $u$  and  $y$ - $v$  correlation.



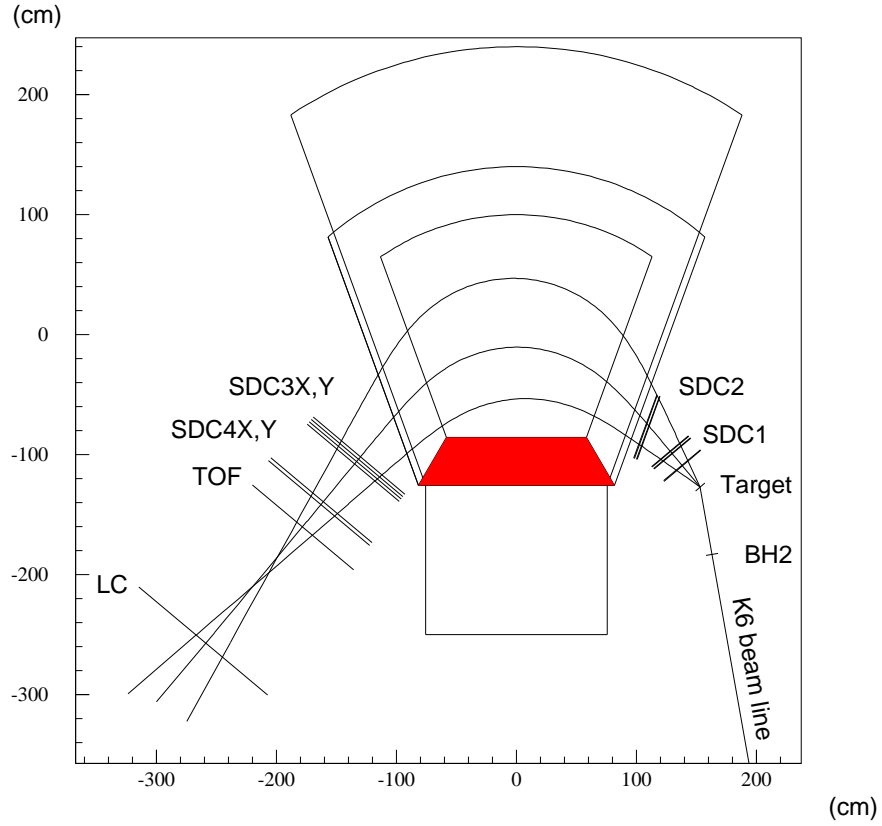


Figure A.1: Schematic top view of the SKS. The shadowed area shows an additional acceptance cut.

Table A.1: Cuts for each detector applied in the Monte-Carlo simulation.

Detector	$x$ (cm)	$y$ (cm)
SDC1	$ x  \leq 20$	-
SDC2	$ x  \leq 28$	$ y  \leq 11$ (395,320A) $ y  \leq 10$ (272A) $ y  \leq 7.5$ (210A)
(pole gap)	-	$ y  \leq 23.5$
SDC3	$-46.0 \leq x \leq 48.5$	$ y  \leq 31.5$
SDC4	$-47.0 \leq x \leq 47.5$ (395A) $-47.5 \leq x \leq 47.5$ (320A) $-47.5 \leq x \leq 47.5$ (272A) $-47.0 \leq x \leq 48.0$ (210A)	$ y  \leq 50$
TOF	$-52.5 \leq x \leq 47.5$ (395A) $-53.0 \leq x \leq 48.0$ (320A) $-53.0 \leq x \leq 47.0$ (272A) $-52.5 \leq x \leq 48.0$ (210A)	$ y  \leq 50$
LC	$-72.5 \leq x \leq 72.0$ (395A) $-73.0 \leq x \leq 69.5$ (320A) $-74.0 \leq x \leq 72.0$ (272A) $-72.5 \leq x \leq 70.0$ (210A)	$ y  \leq 70$

## 395A mode

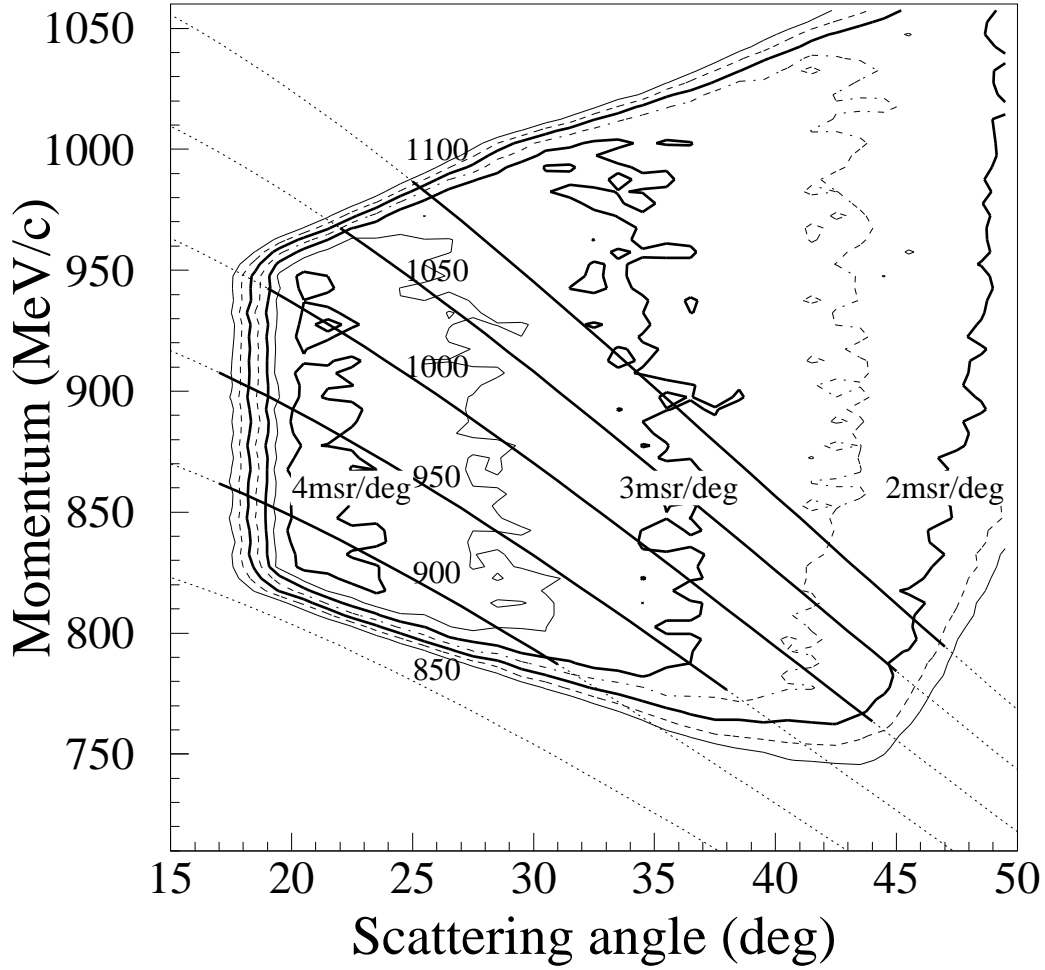


Figure A.2: Effective solid angle of SKS for the 395A mode. The dotted and solid loci show kinematics of  $\pi^-$ -p scattering for each beam momentum. The solid loci show regions where SAID calculations were reproduced.

## 320A mode

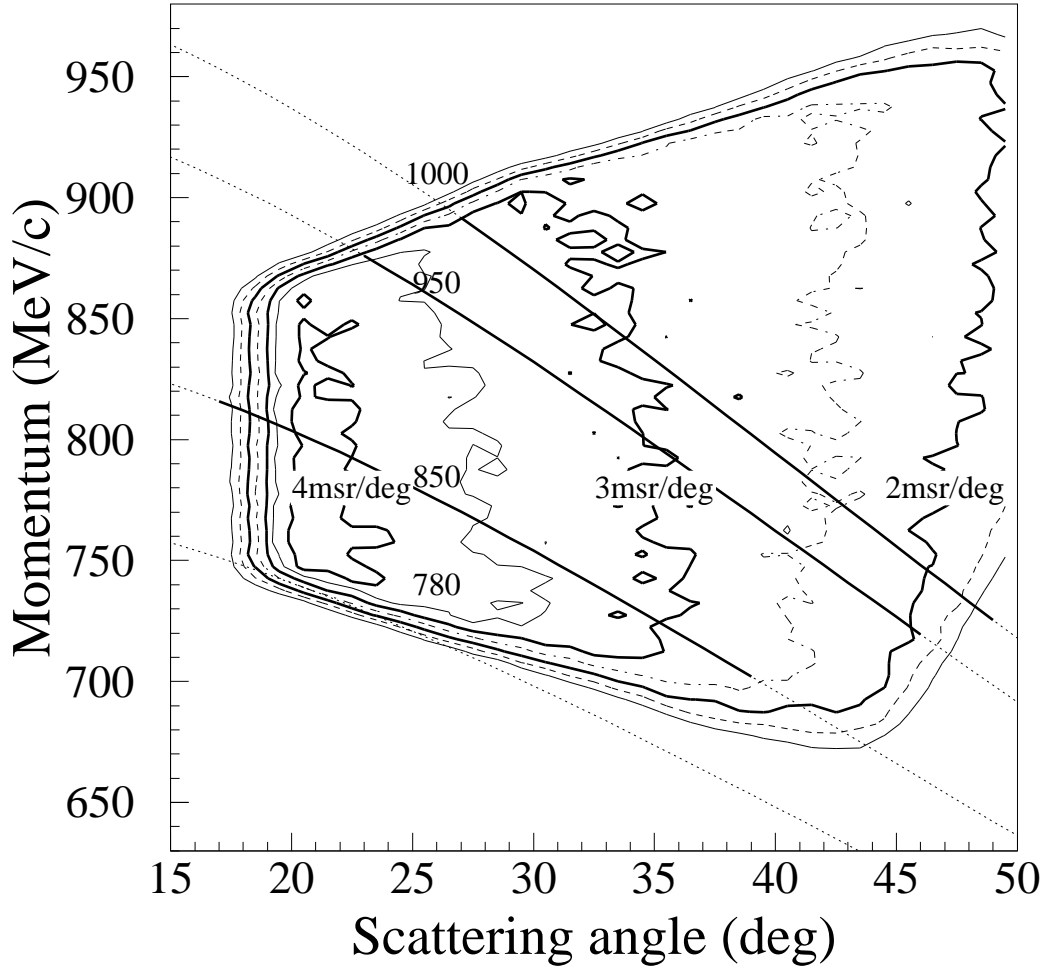


Figure A.3: Effective solid angle of SKS for the 320A mode. The dotted and solid loci show kinematics of  $\pi^-$ -p scattering for each beam momentum. The solid loci show regions where SAID calculations were reproduced.

## 272A mode

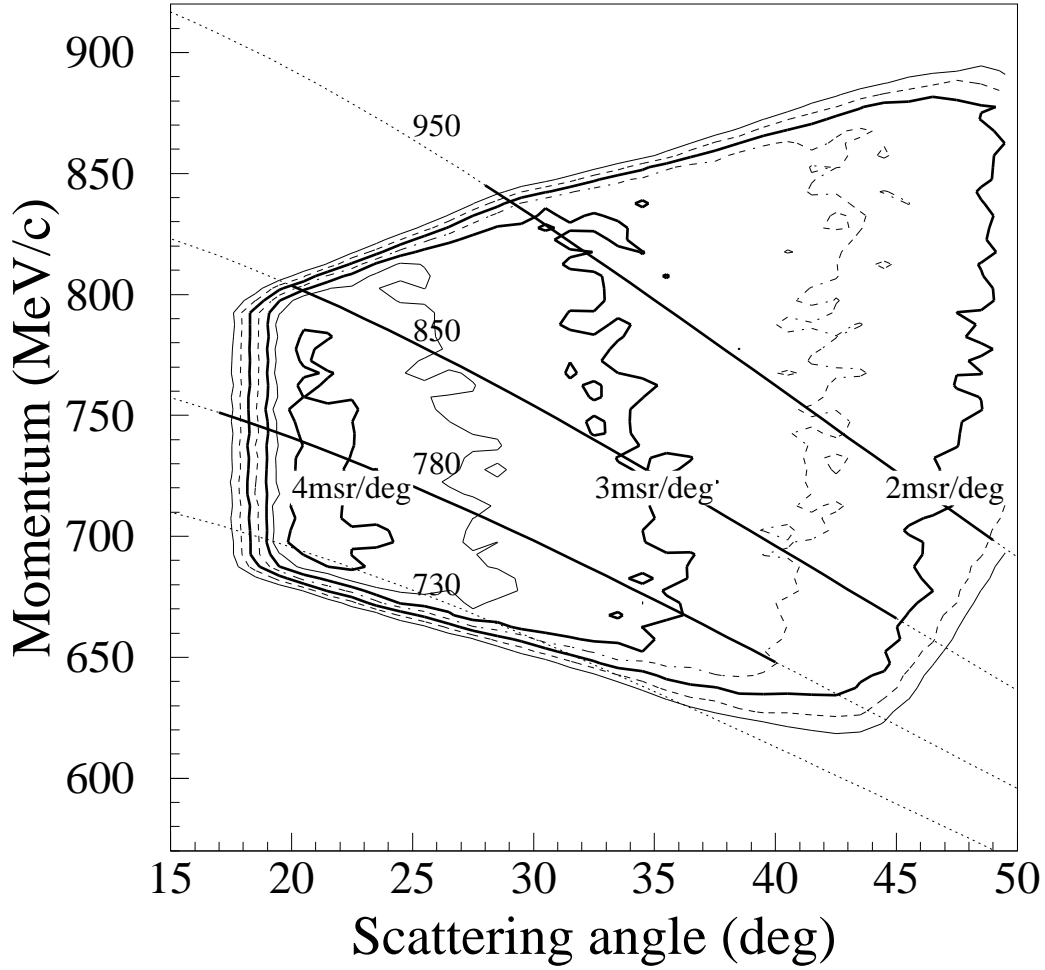


Figure A.4: Effective solid angle of SKS for the 272A mode. The dotted and solid loci show kinematics of  $\pi^-$ -p scattering for each beam momentum. The solid loci show regions where SAID calculations were reproduced.

## 210A mode

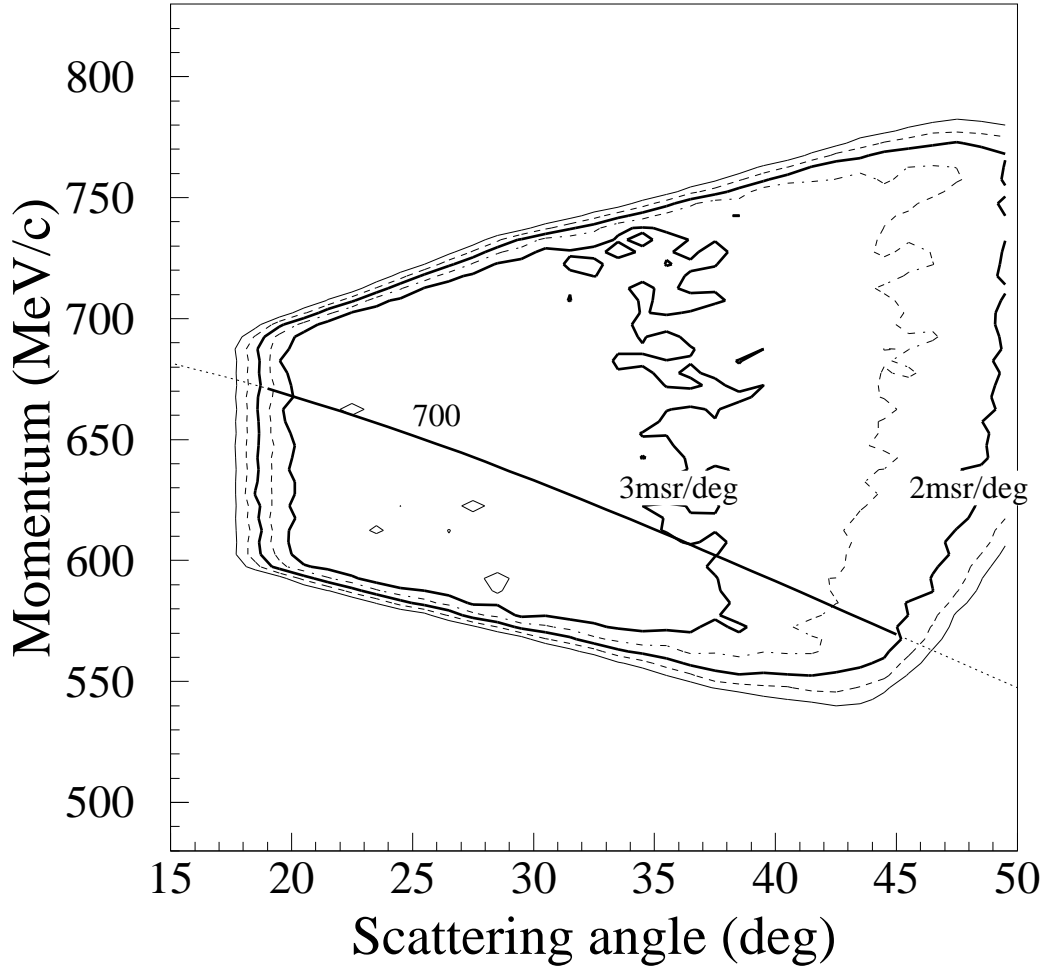


Figure A.5: Effective solid angle of SKS for the 210A mode. The dotted and solid loci show kinematics of  $\pi^-$ -p scattering for each beam momentum. The solid loci show regions where SAID calculations were reproduced.

## A.2 $\pi^-$ -p cross sections

In this section, measured  $\pi^-$ -p elastic scattering cross sections are shown for each SKS mode. The error bars are statistical only.

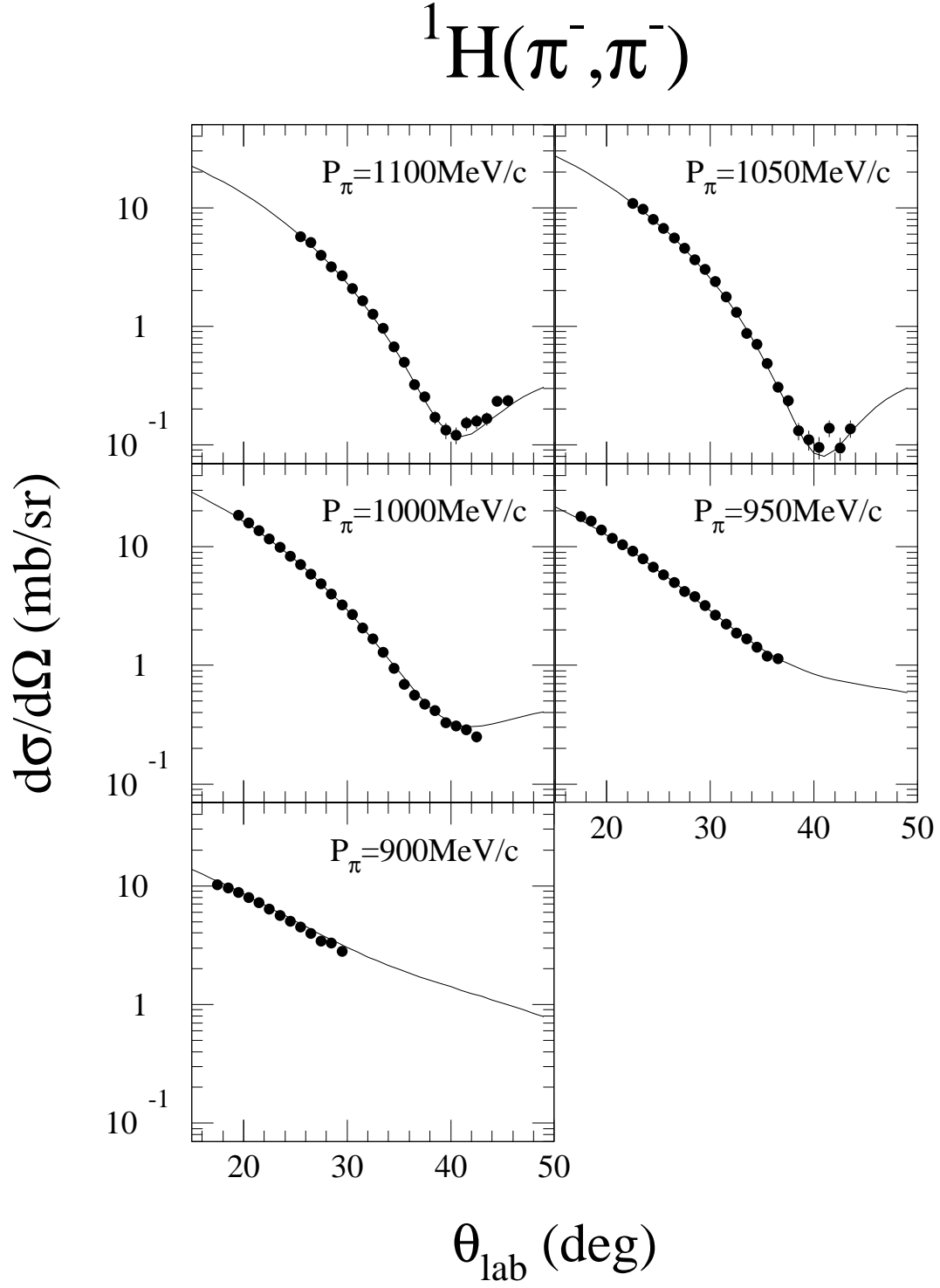


Figure A.6: Differential cross sections for  $\pi^-$ -p elastic scattering measured with the 395A mode. The solid lines show the results of SAID.



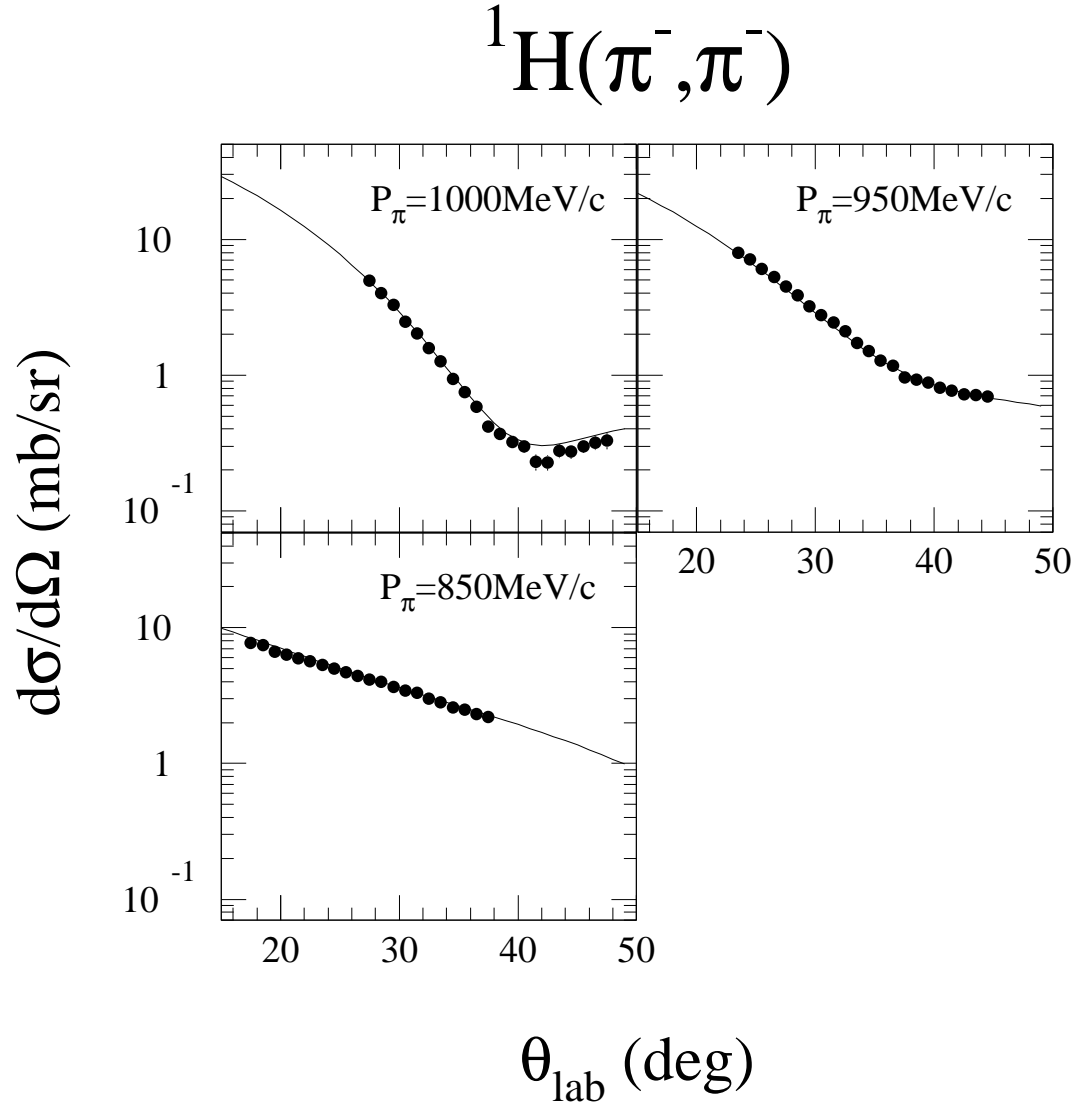


Figure A.7: Differential cross sections for  $\pi^-$ -p elastic scattering measured with the 320A mode. The solid lines show the results of SAID.

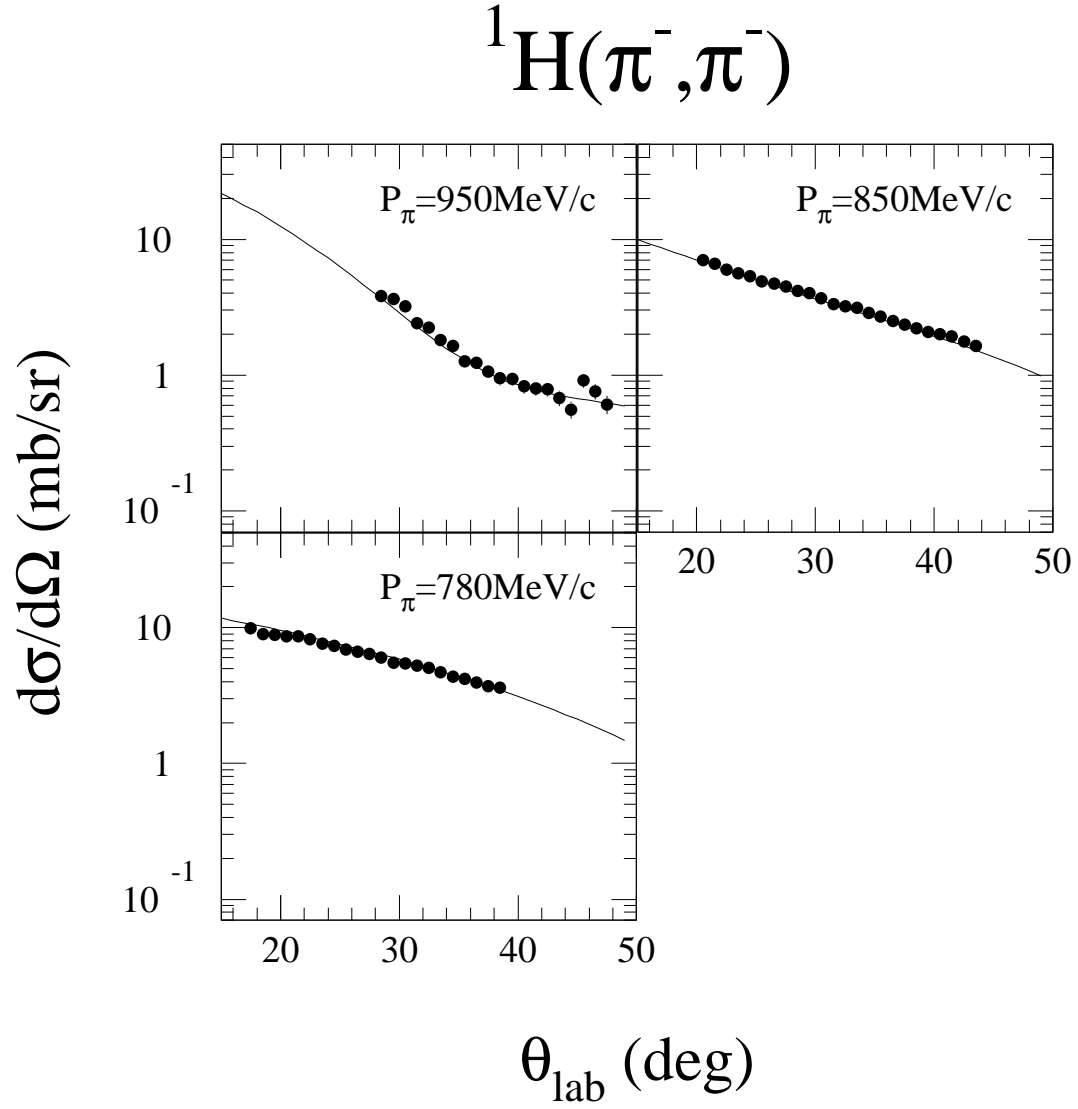


Figure A.8: Differential cross sections for  $\pi^-$ -p elastic scattering measured with the 272A mode. The solid lines show the results of SAID.

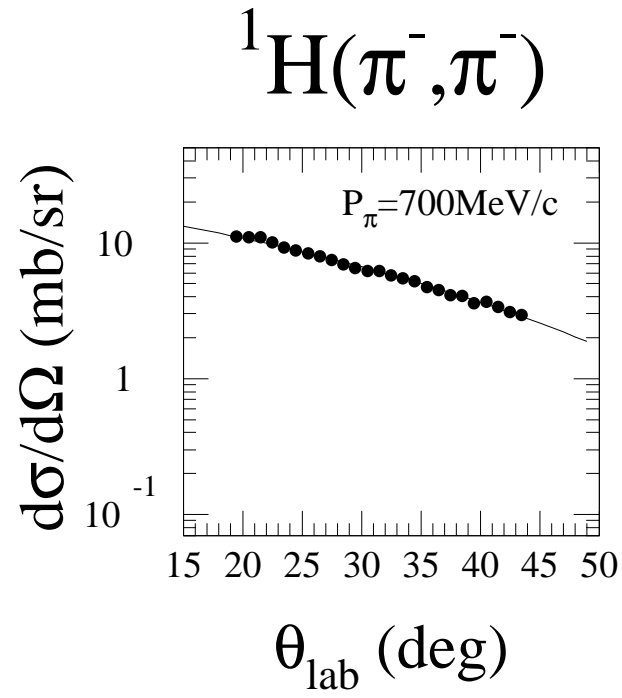


Figure A.9: Differential cross sections for  $\pi^-$ -p elastic scattering measured with the 210A mode. The solid lines show the results of SAID.

# Appendix B

## Data and Fitted Results

In this section, all experimental data with the fitted results are shown. The error bars are statistical only.

$$D(\pi^-, \pi'^-)$$

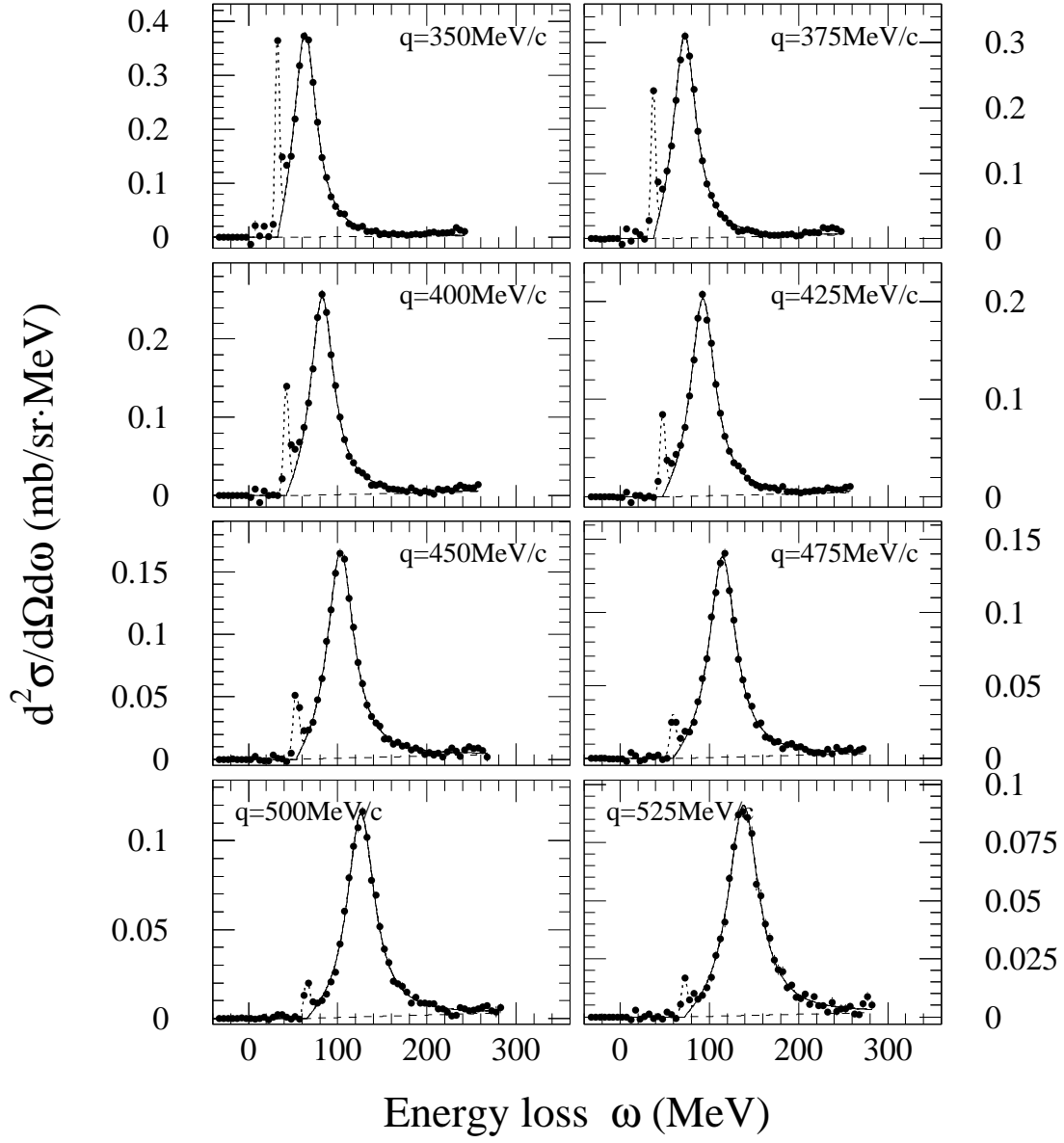


Figure B.1: Doubly differential cross sections for the  $\pi^-$ -D scattering.

$$D(\pi^-, \pi'^-)$$

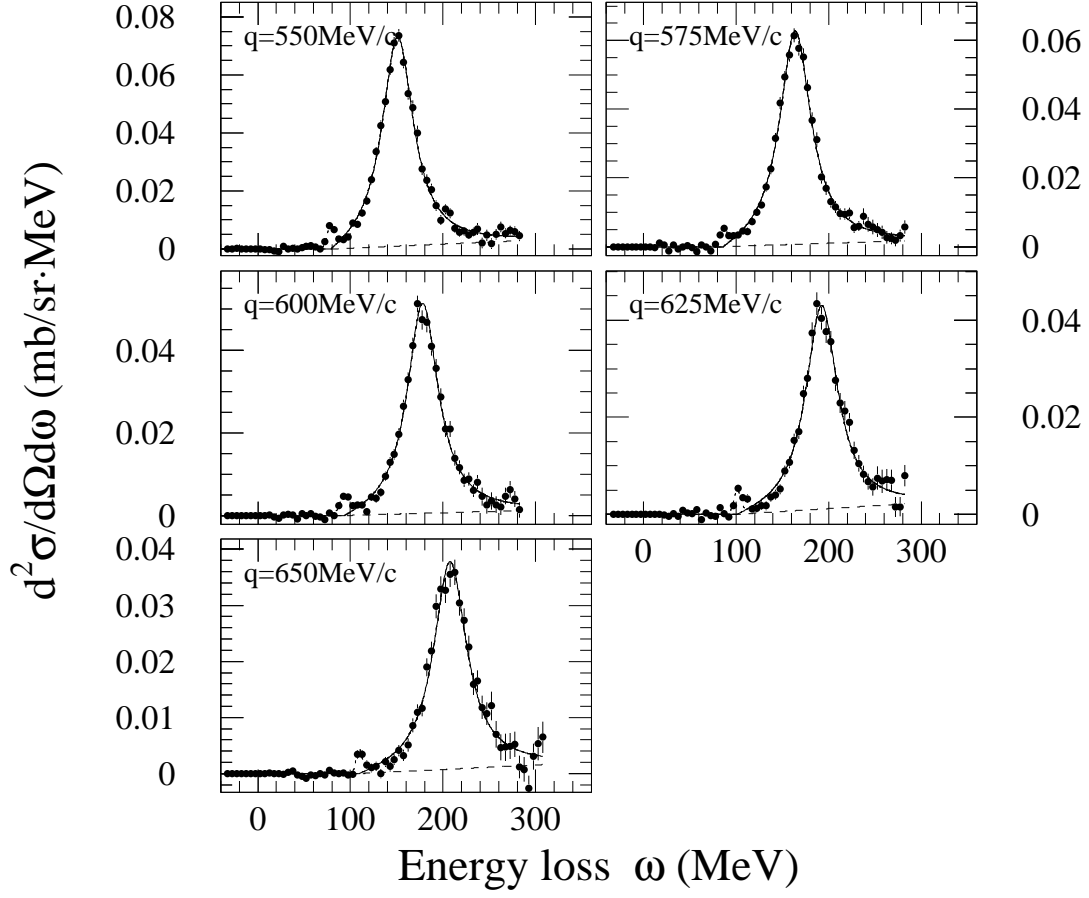


Figure B.1 : — Continued

# ${}^6\text{Li}(\pi^-, \pi^-')$

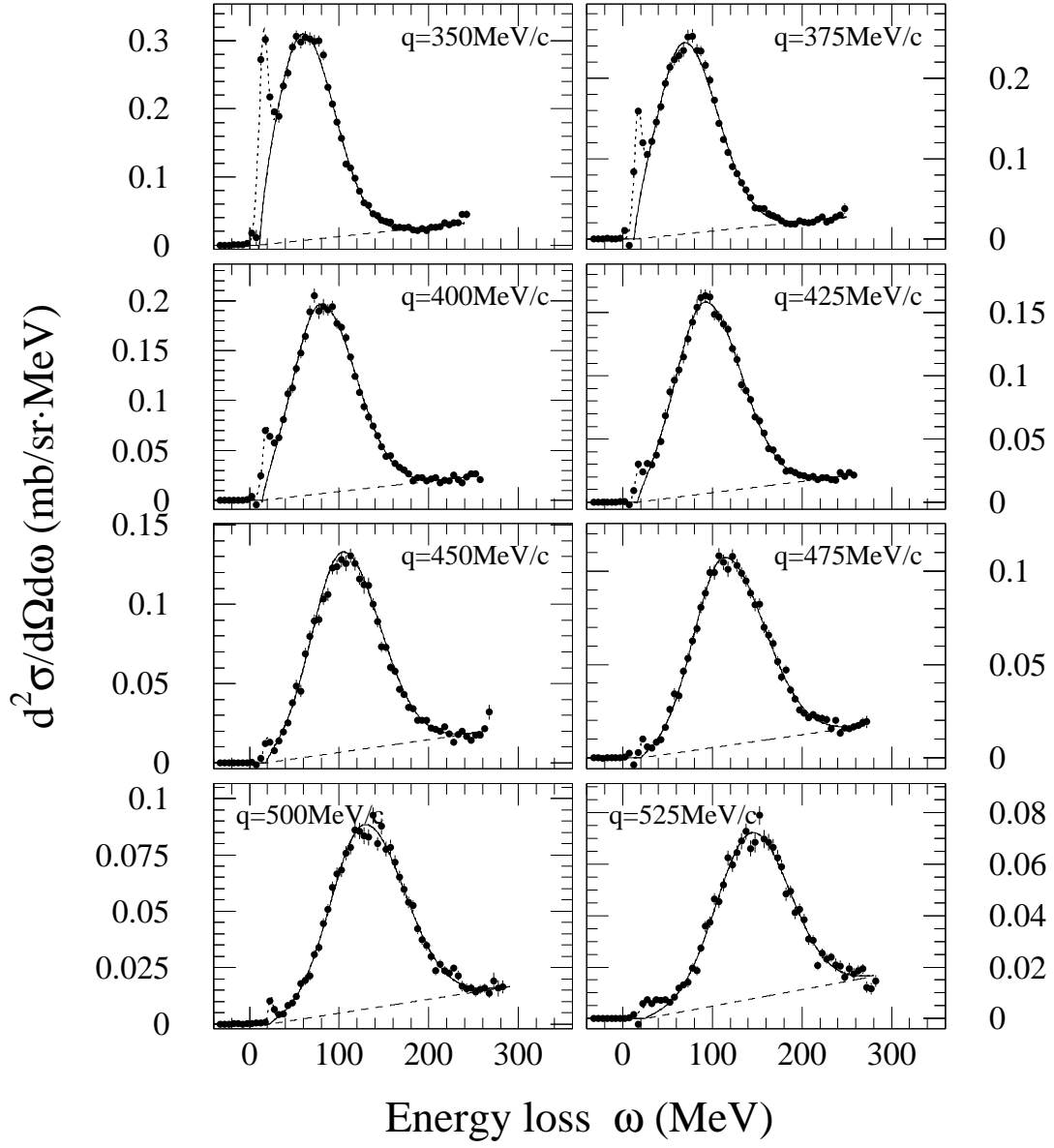


Figure B.2: Doubly differential cross sections for the  $\pi^-$ - ${}^6\text{Li}$  scattering.

# ${}^6\text{Li}(\pi^-, \pi^-')$

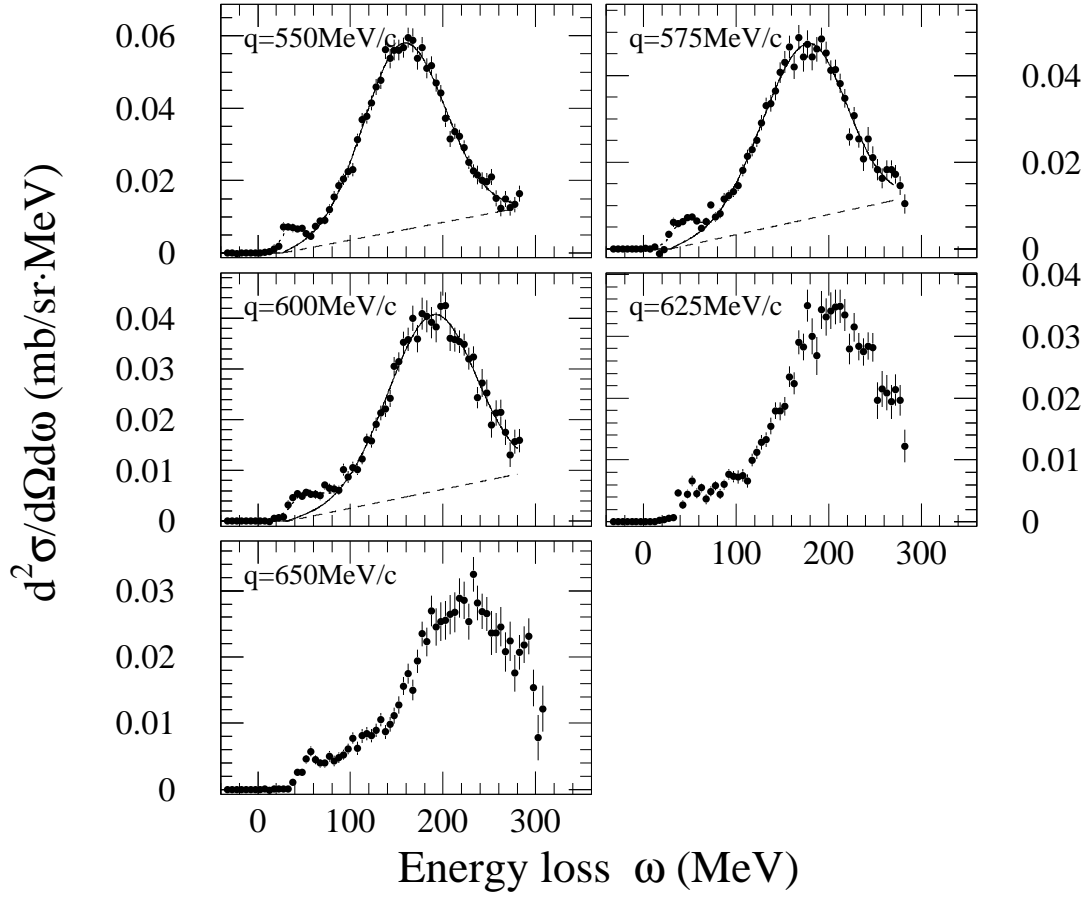


Figure B.2 : — Continued



$$^{12}\text{C}(\pi^-, \pi^-')$$

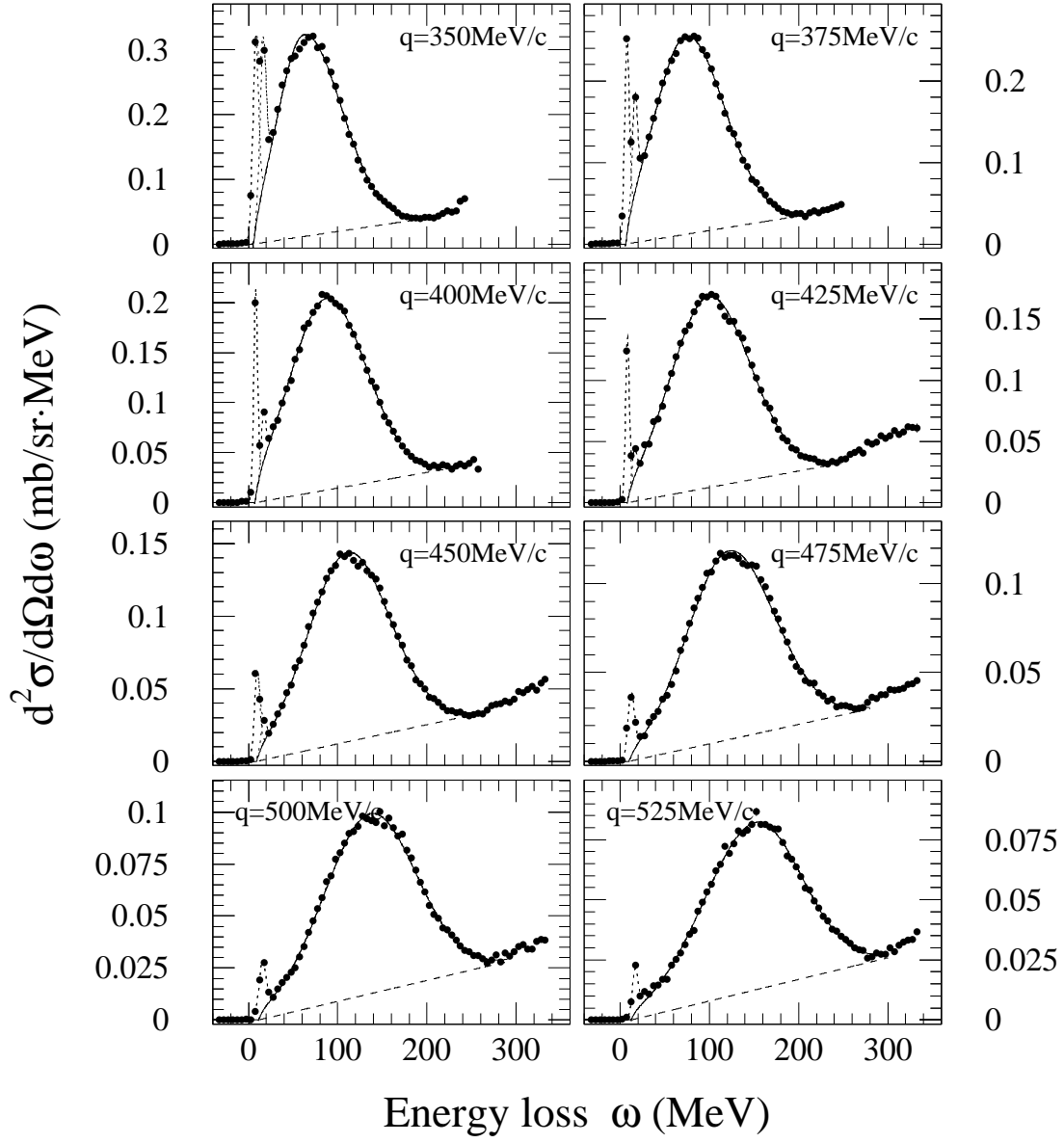


Figure B.3: Doubly differential cross sections for the  $\pi^-$ -C scattering.

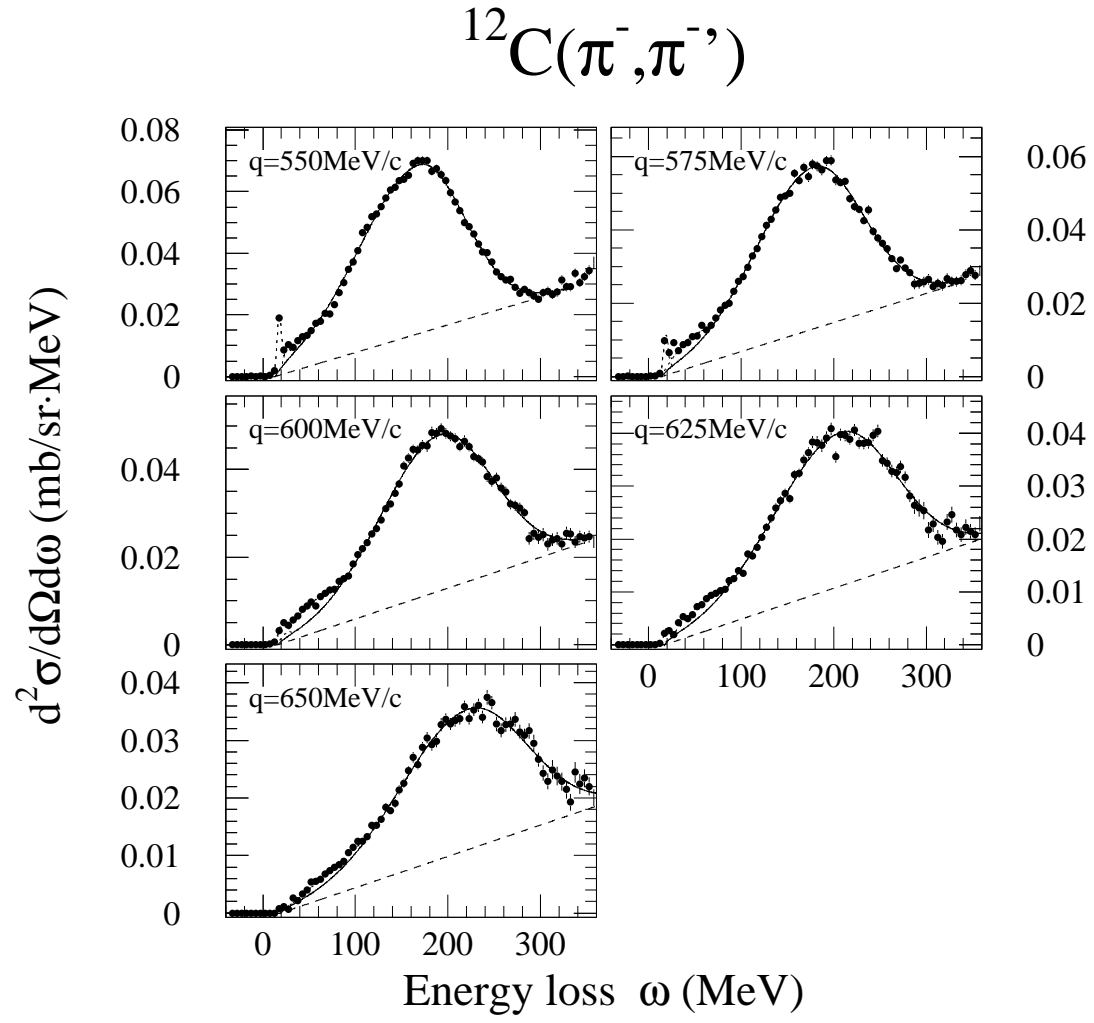


Figure B.3 : — Continued

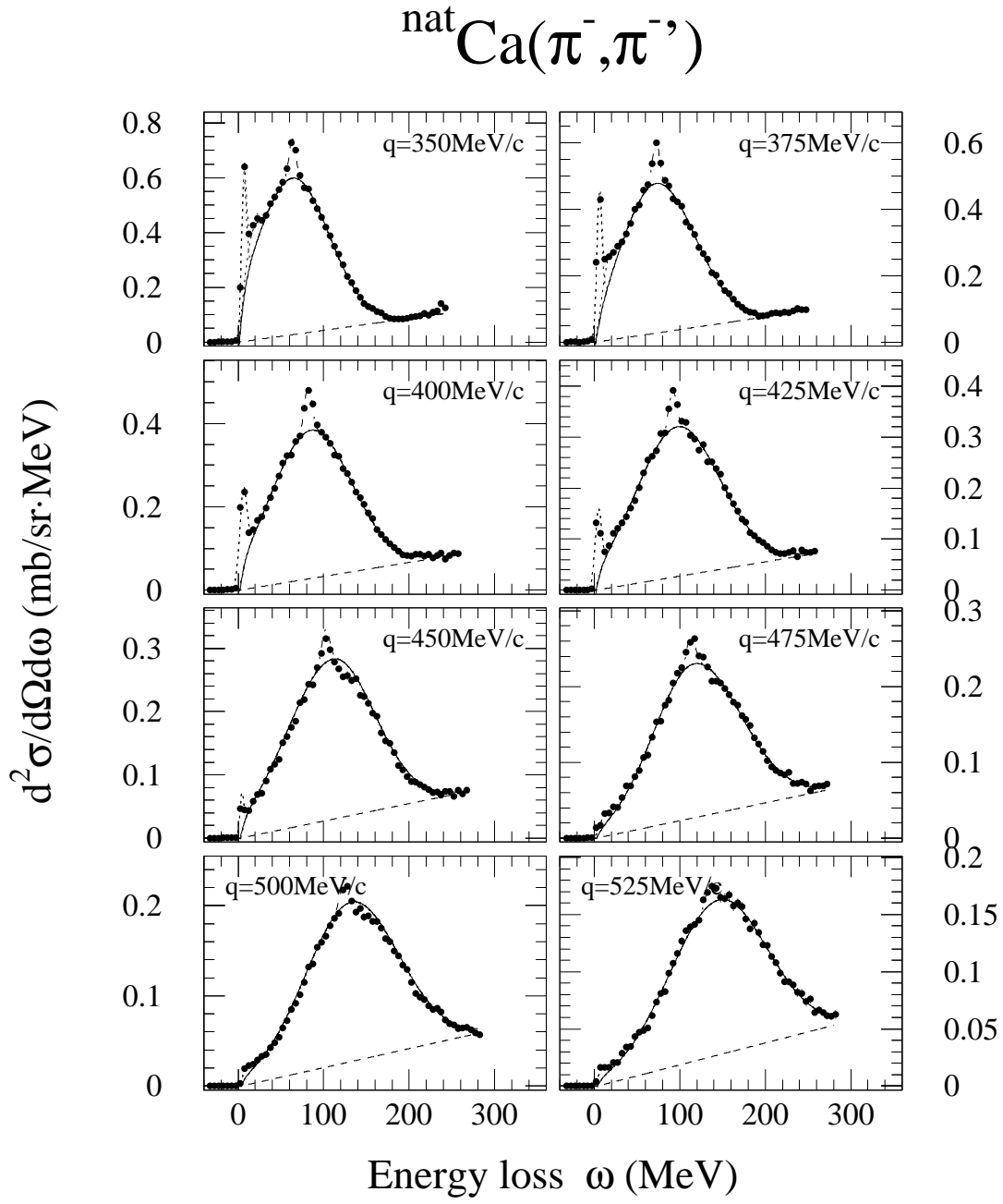


Figure B.4: Doubly differential cross sections for the  $\pi^-$ -Ca scattering.

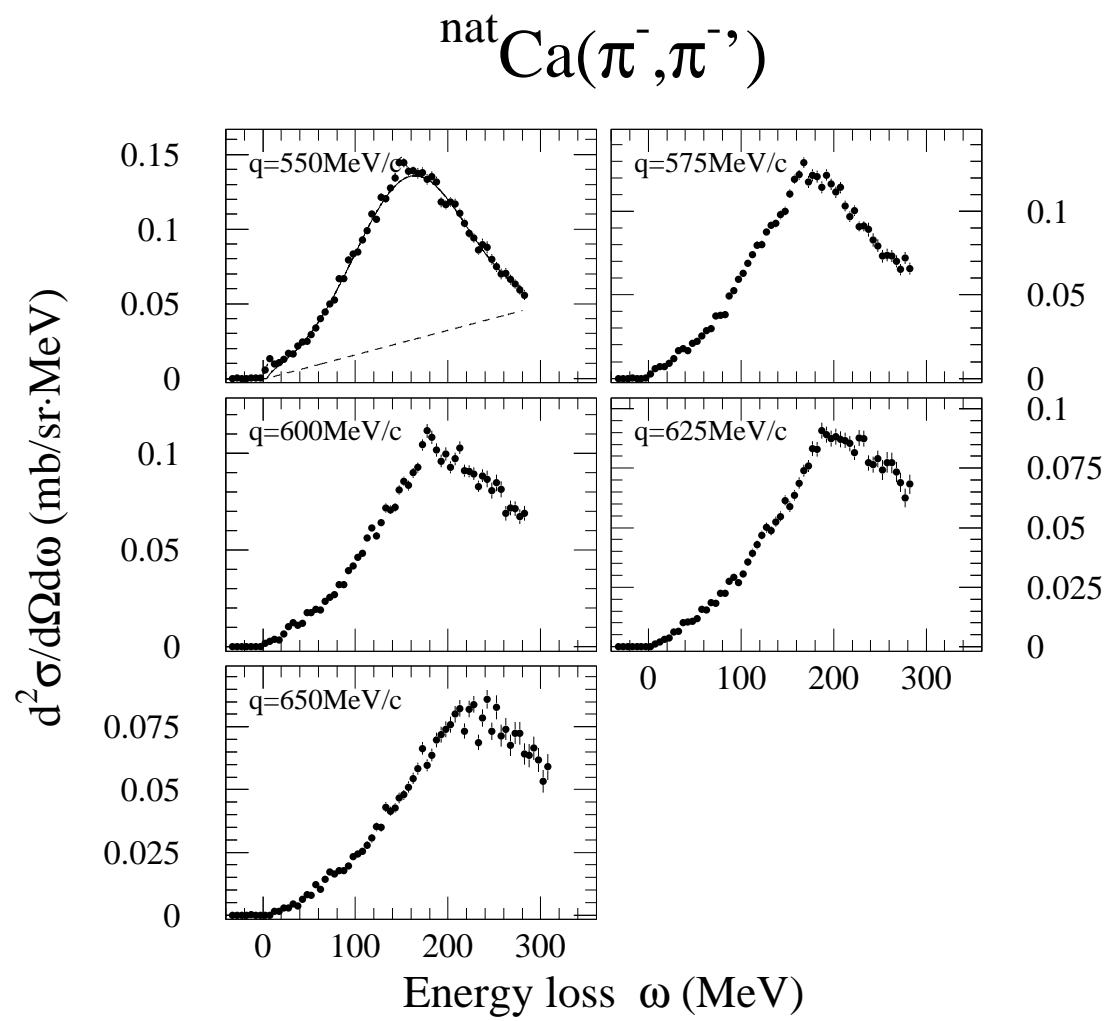


Figure B.4 : — Continued

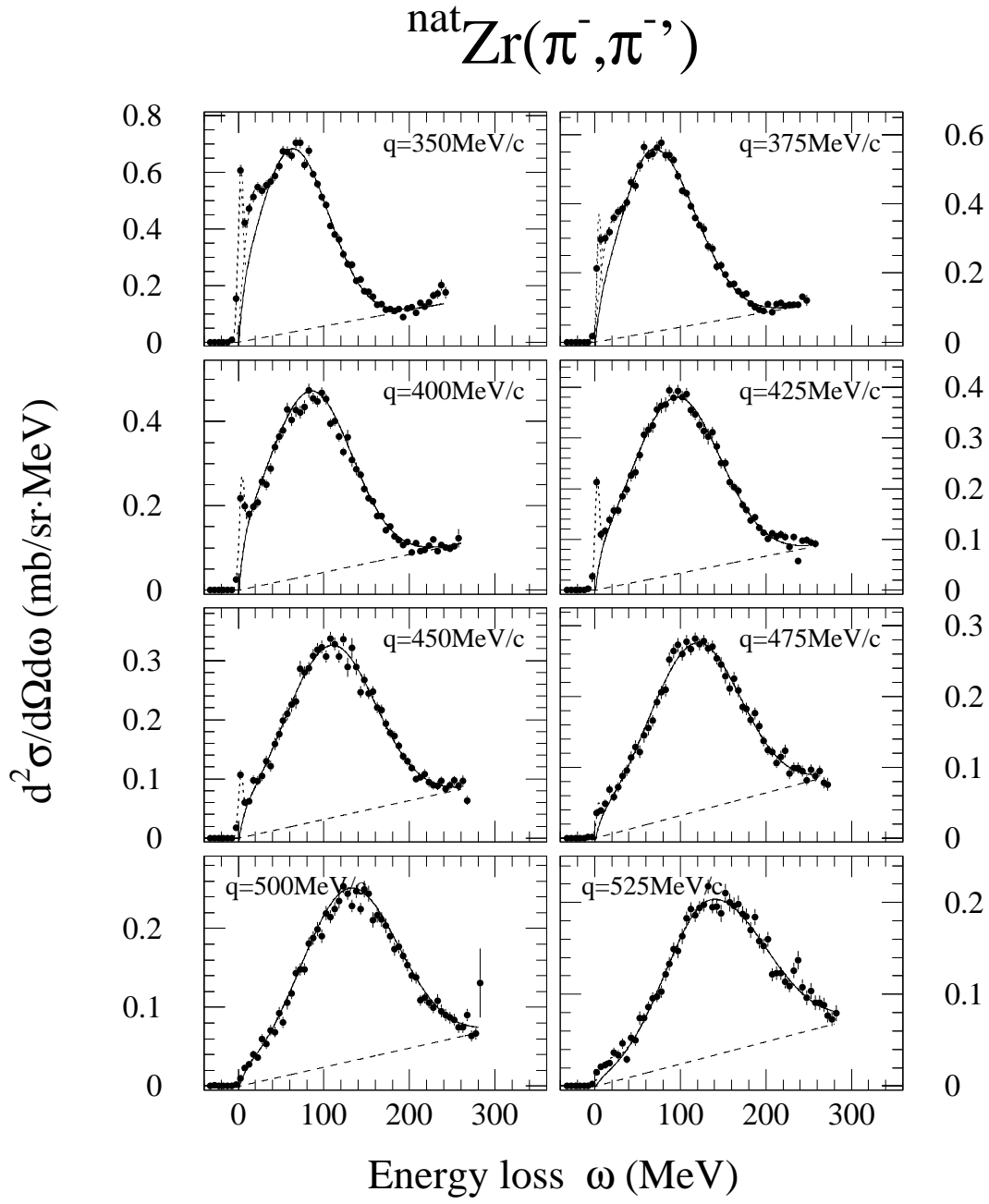


Figure B.5: Doubly differential cross sections for the  $\pi^-$ -Zr scattering.

$^{\text{nat}}\text{Zr}(\pi^-, \pi^-')$

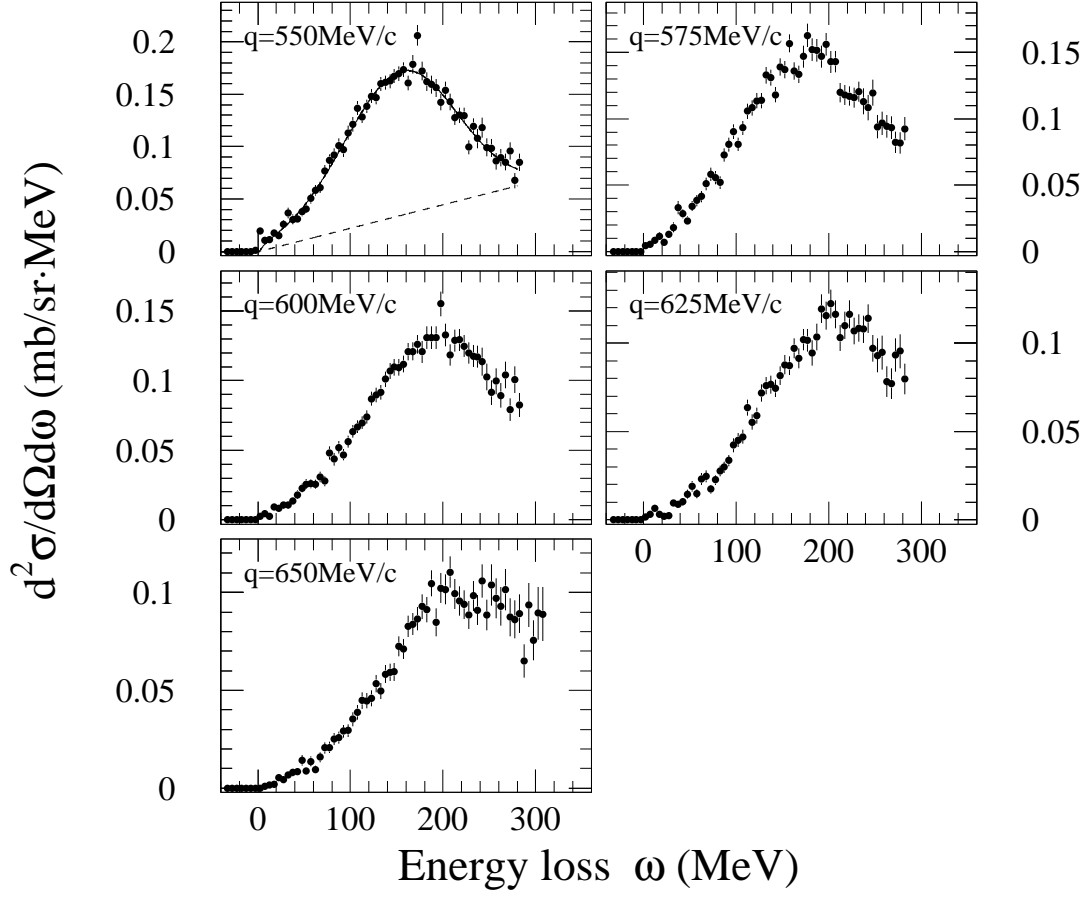


Figure B.5 : — Continued

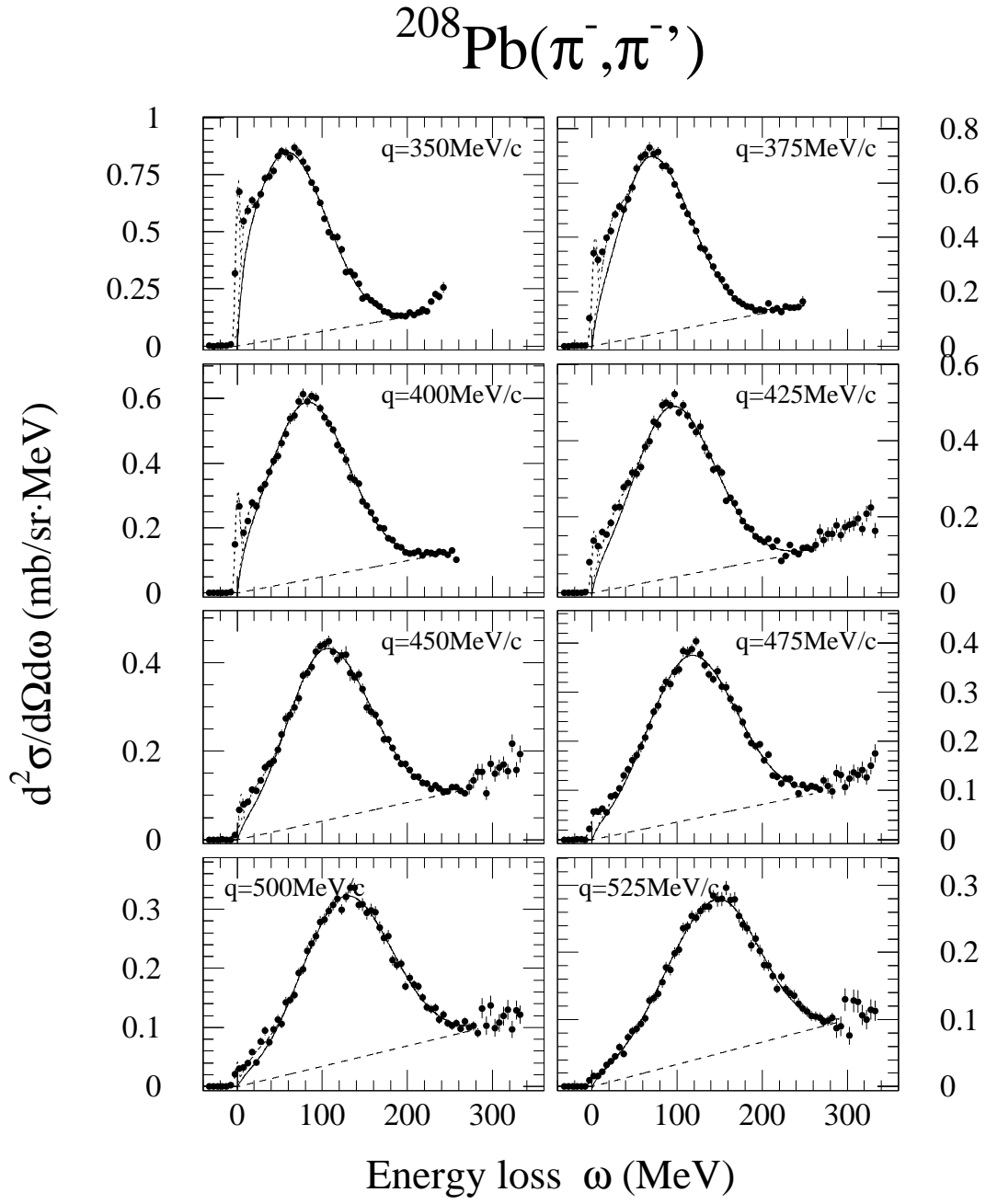


Figure B.6: Doubly differential cross sections for the  $\pi^-$ - $^{208}\text{Pb}$  scattering.

# $^{208}\text{Pb}(\pi^-, \pi^-')$

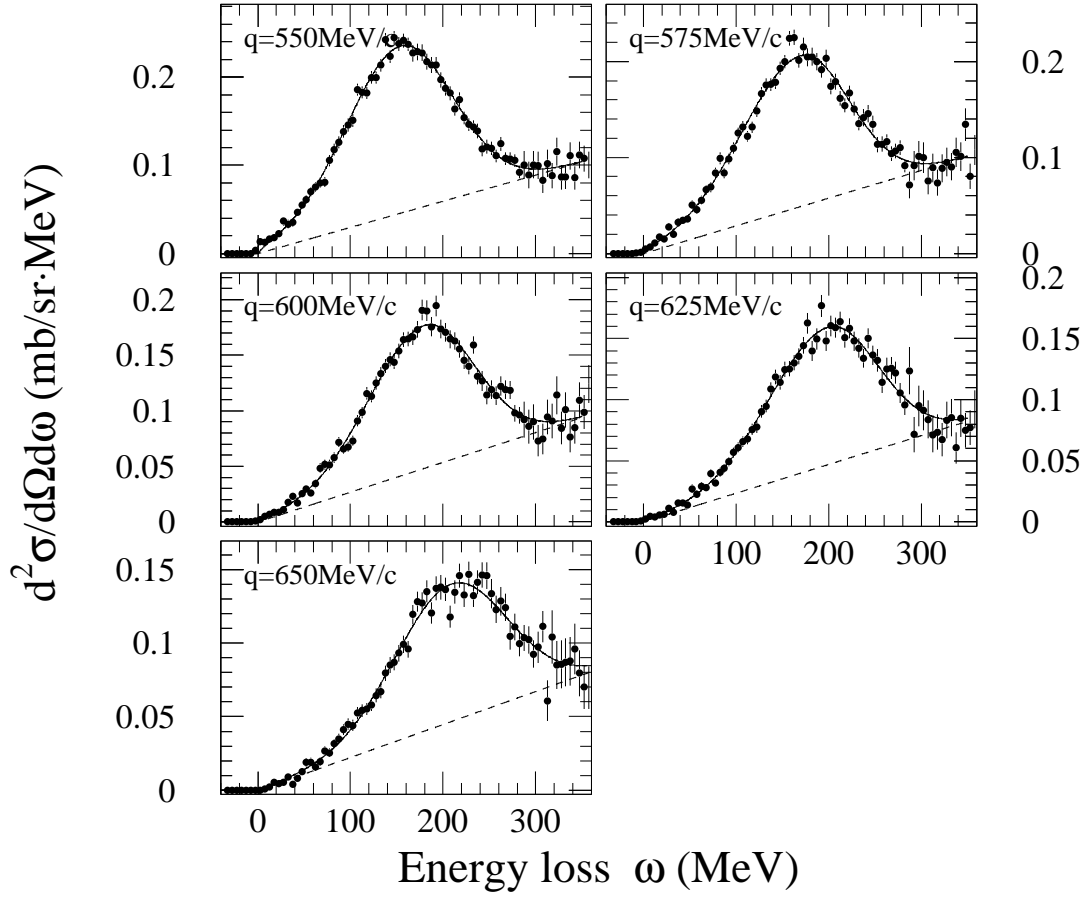


Figure B.6 : — Continued



# Bibliography

- [1] P. Barreau, M. Bernheim, J. Duclos, J. M. Finn, Z. Meziani, J. Morgenstern, J. Mougey, D. Royer, B. Saghai, D. Tarnowski, S. Turck-chieze, M. Brussel, G. P. Capitani, E. De Sanctis, S. Frullani, F. Garibaldi, D. B. Isabelle, E. Jans, I. Sick, and P. D. Zimmerman, Nucl. Phys. **A402**, 515 (1983).
- [2] M. Deady, C. F. Williamson, P. D. Zimmerman, R. Altemus and R. R. Whitney, Phys. Rev. C **33**, 1897 (1986).
- [3] C. C. Blatchley, J. J. LeRose, O. E. Pruet, Peter D. Zimmerman, C. F. Williamson, and M. Deady, Phys. Rev. C **34**, 1243 (1986).
- [4] A. Zghiche, J. F. Danel, M. Bernheim, M. K. Brussel, G. P. Capitani, E. De Sanctis, S. Frullani, F. Garibaldi, A. Gerard, J. M. Le Goff, A. Magnon, C. Marchand, Z. E. Meziani, J. Morgenstern, J. Picard, D. Reffay-Pikeroën, M. Traini, S. Turck-Chieze, and P. Vernin, Nucl. Phys. **A572**, 513 (1994).
- [5] R. E. Chrien, T. J. Krieger, R. J. Sutter, M. May, H. Palevsky, R. L. Stearns, T. Kozlowski, and T. Bauer, Phys. Rev. C **21**, 1014 (1980).
- [6] T. A. Carey, K. W. Jones, J. B. McClelland, J. M. Moss, L. B. Rees, N. Tanaka, and A. D. Bacher, Phys. Rev. Lett. **53**, 144 (1984).
- [7] L. B. Rees, J. M. Moss, T. A. Carey, K. W. Jones, J. B. McClelland, N. Tanaka, A. D. Bacher, and H. Esbensen, Phys. Rev. C **34**, 627 (1986).
- [8] L. Wang, X. Yang, J. Rapaport, C. D. Goodman, C. C. Foster, Y. Wang, J. Piekarewicz, E. Sugarbaker, D. Marchlinski, S. de Lucia, B. Luther, L. Rybarczyk, T. N. Taddeucci, and B. K. Park, Phys. Rev. C **50**, 2438 (1994).
- [9] H. Sakai, M. B. Greenfield, K. Hatanaka, S. Ishida, N. Koori, H. Okamura, A. Okihana, H. Otsu, N. Sakamoto, Y. Satou, T. Uesaka, and T. Wakasa, Nucl. Phys. **A577**, 111c (1994).
- [10] D. L. Prout, C. Zafiratos, T. N. Taddeucci, J. Ullmann, R. C. Byrd, T. A. Carey, P. Lisowski, J. B. McClelland, L. J. Rybarczyk, W. Sailor, W. Amian, M. Braunstein, D. Lind, D. J. Mercer, D. Cooper, S. DeLucia, B. Luther, D. G. Marchlinski, E. Sugarbaker, J. Rapaport, B. K. Park,

- E. Gülmez, C. A. Whitten, Jr., C. D. Goodman, W. Huang, D. Ciskowski, and W. P. Alford, *Phys. Rev. C* **52**, 228 (1995).
- [11] I. Bergqvist, A. Brockstedt, L. Carlén, L. P. Ekström, B. Jakobsson, C. Ellegaard, C. Gaarde, J. S. Larsen, C. Goodman, M. Bedjidian, D. Contardo, J. Y. Grossiord, A. Guichard, R. Haroutunian, J. R. Pizzi, D. Bachelier, J. l. Boyard, T. Hennino, J. C. Jourdain, M. Roy-Stephan, M. Boivin, and P. Radvanyi, *Nucl. Phys.* **A469**, 648 (1987).
- [12] J. E. Wise, M. R. Braunstein, S. Høibråten, M. D. Kohler, B. J. Kriss, J. Ouyang, R. J. Peterson, J. A. McGill, C. L. Morris, S. J. Seestrom, R. M. Whitton, J. D. Zumbro, C. M. Edwards, and A. L. Williams, *Phys. Rev. C* **48**, 1840 (1993).
- [13] J. Ouyang, S. Høibråten, and R. J. Peterson, *Phys. Rev. C* **48**, 1074 (1993).
- [14] R. J. Peterson, S. Høibråten, J. Ouyang, M. R. Braunstein, X. Y. Chen, M. D. Kohler, B. J. Kriss, D. J. Mercer, D. S. Oakley and D. L. Prout, *Phys. Lett. B* **297**, 238 (1992).
- [15] C. M. Kormanyos, R. J. Peterson, J. R. Shepard, J. E. Wise, S. Bart, R. E. Chrien, L. Lee, B. L. Clausen, J. Piekarewicz, M. B. Barakat, E. V. Hungerford, R. A. Michael, K. H. Hicks, and T. Kishimoto, *Phys. Rev. C* **51**, 669 (1995).
- [16] W. M. Alberico, M. Ericson and A. Molinari, *Nucl. Phys.* **A379**, 429 (1982).
- [17] T. N. Taddeucci, B. A. Luther, L. J. Rybarcyk, R. C. Byrd, J. B. McClelland, D. L. Prout, S. DeLucia, D. A. Cooper, D. G. Marchlenski, E. Sugarbaker, B. K. Park, T. Sams, C. D. Goodman, J. Rapaport, M. Ichimura, and K. Kawahigashi, *Phys. Rev. Lett.* **73**, 3516 (1994).
- [18] A. De Pace, C. García-Recio, and E. Oset, *Phys. Rev. C* **55**, 1394 (1997).
- [19] T. Fukuda, T. Hasegawa, O. Hashimoto, A. Higashi, S. Honma, T. Kitami, Y. Matsuyama, T. Miyachi, T. Morimoto, T. Nagae, K. Omata, M. Sekimoto, T. Shibata, H. Sakaguchi, T. Takahashi, K. Aoki, Y. Doi, Y. Kondo, Y. Makida, M. Nomachi, H. Noumi, O. Sasaki, T. Shintomi, H. Bhang, H. Park, M. Youn, H. Yu, Y. Gavrilov, S. Ajimura, T. Kishimoto, A. Ohkusu, N. Shinkai, K. Maeda, R. Sawafta, *Nucl. Instr. and Meth.* **A361**, 485 (1995).
- [20] S. Morinobu, private communication.
- [21] J. Myrheim and L. Bugge, *Nucl. Instr. and Meth.* **160**, 43 (1979).
- [22] R. A. Arndt, I. I. Strakovsky, R. L. Workman, and M. M. Pavan, *Phys. Rev. C* **52**, 2120 (1995).

- [23] H. Esbensen and G. F. Bertsch, *Ann. Phys. (N.Y.)* **157**, 255 (1984).
- [24] A. Erell, J. Alster, J. Lichtenstadt, M. A. Moinester, J. D. Bowman, M. D. Cooper, F. Irom, H. S. Matis, E. Piasetzky, and U. Sennhauser, *Phys. Rev. C* **34**, 1822 (1986).
- [25] J. D. Zumbro, C. L. Morris, J. A. McGill, S. J. Seestrom, R. M. Whitton, C. M. Edwards, A. L. Williams, M. R. Braunstein, M. D. Kohler, B. J. Kriss, S. Høibråten, R. J. Peterson, J. Ouyang, J. E. Wise, and W. R. Gibbs, *Phys. Rev. Lett.* **71**, 1796 (1993).
- [26] W. M. Alberico, M. Ericson, and A. Molinari, *Ann. Phys. (N.Y.)* **154**, 356 (1984).
- [27] R. J. Peterson, S. Høibråten, J. Ouyang, M. R. Braunstein, X. Y. Chen, M. D. Kohler, B. J. Kriss, D. J. Mercer, D. S. Oakley, and D. L. Prout, *Phys. Lett. B* **297**, 238 (1992).
- [28] G. F. Bertsch and O. Scholten, *Phys. Rev. C* **25**, 804 (1982).
- [29] R. R. Whitney, I. Sick, J. R. Ficenec, R. D. Kephart, and W. P. Trower, *Phys. Rev. C* **9**, 2230 (1974).
- [30] J. Ouyang, S. Høibråten, and R. J. Peterson, *Phys. Rev. C* **47**, 2809 (1993).
- [31] R. J. Glauber and G. Matthiae, *Nucl. Phys.* **B21**, 135 (1970).
- [32] H. de Vries, C. W. de Jager, and C. de Vries, *At. Data and Nucl. Data Tables* **36**, 495 (1987).
- [33] J. S. O'Connell and B. Schrøder, *Phys. Rev. C* **38**, 2447 (1988).
- [34] H. Otsu, H. Sakai, H. Okamura, T. Wakasa, K. Hatanaka, S. Ishida, N. Sakamoto, T. Uesaka, Y. Satou, T. Fujita, A. Okihana, N. Koori, and M. B. Greenfield, *Proceedings of the RCNP International mini Workshop on NUCLEAR MEDIUM EFFECT VIA NUCLEON INDUCED REACTION*, *Genshikaku Kenkyu Vol.42 No.1,13* (1997).
- [35] A. De Pace and M. Viviani, *Phys. Rev. C* **48**, 2931 (1993).
- [36] M. Ichimura, K. Kawahigashi, T. S. Jørgensen and C. Gaarde, *Phys. Rev. C* **39** 1446, (1989).
- [37] C. J. Horowitz and D. P. Murdock, *Phys. Rev. C* **37**, 2032 (1988).
- [38] A. De Pace, private communication.
- [39] K. Nakayama, S. Krewald, J. Speth, and W. G. Love, *Nucl. Phys.* **A431**, 419 (1984).